Master Thesis

A Numerical Study on Compressible Flows over Thick Airfoils for Tilted Wind Turbines

S. Hemelaar

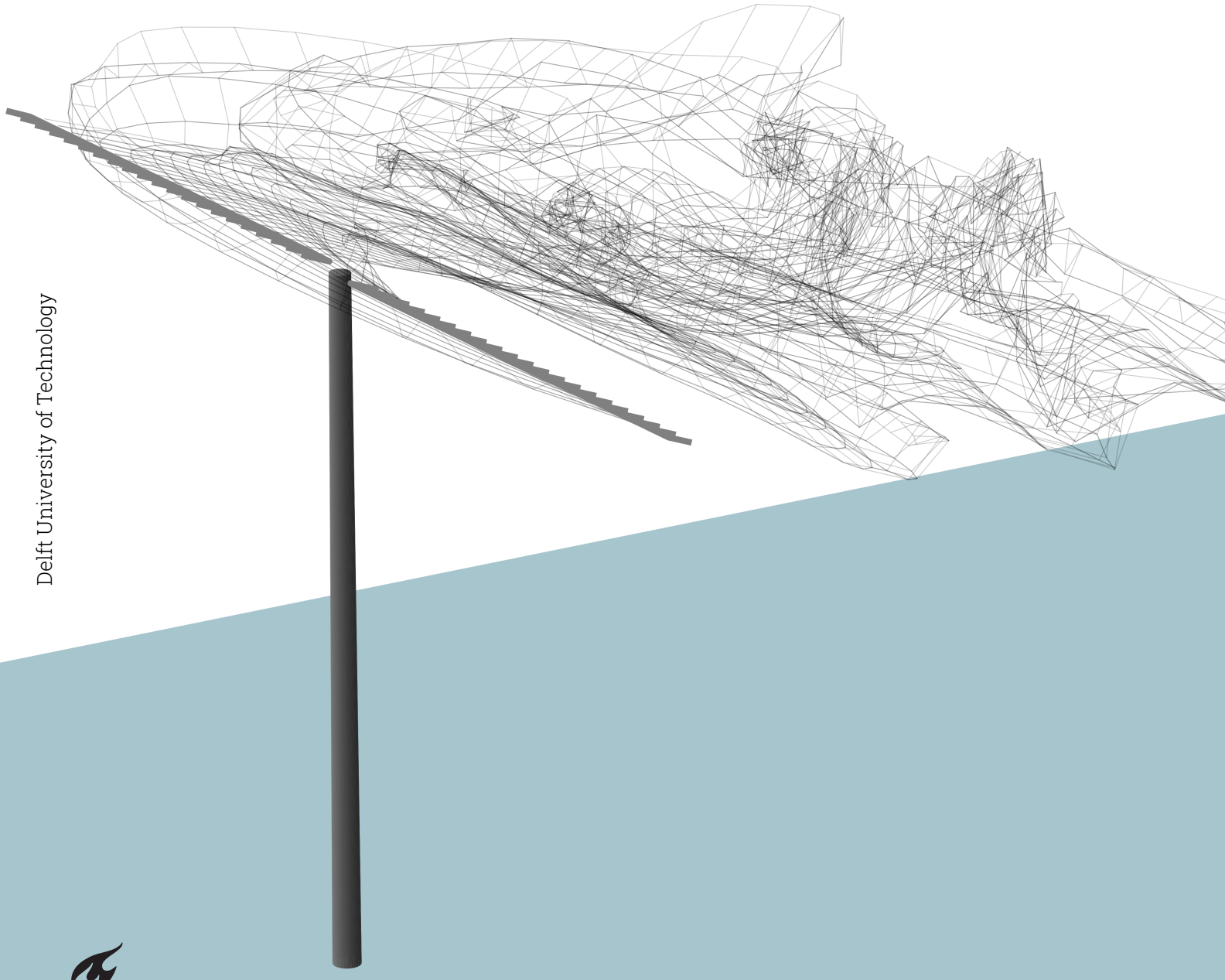

Delft University of Technology

TU Delft

Master Thesis

A Numerical Study on Compressible Flows over Thick Airfoils for Tilted Wind Turbines

by

S. Hemelaar

to obtain the degree of Master of Science
at the Delft University of Technology,
to be defended publicly on Tuesday March 26, 2024 at 09:30 AM.

Student number:	4573404	
Project duration:	March 20, 2023 – February 26, 2024	
Thesis committee:	Dr. ir. D. A. von Terzi,	TU Delft, Chair
	Dr. ir. B. W. van Oudheusden,	TU Delft, Examiner
	Dr. ir. D. Modesti,	TU Delft, Supervisor I
	Dr. ir. D. A. M. De Tavernier,	TU Delft, Supervisor II
	Ir. J. C. M. van Beek,	TouchWind B.V.

This thesis is confidential and cannot be made public until December 31, 2028.

Cover: Lifting Line Simulation of the TouchWind 3MW concept rotor.

An electronic version of this thesis is available at `http://repository.tudelft.nl/`.

TU Delft

TouchWind

Preface

As is probably true for many prefaces, this is written during the twilight hours, as the final submission deadline is looming, amidst considerable yet - thankfully - manageable stress. It marks the end of a year full of valuable experiences. Beyond significantly enriching my understanding of aerodynamics and making me a better engineer, another valuable lesson stands out: Humanity has great knowledge, but the unknown still vastly outweighs the known. It has reassured me that my lifetime will be filled with academic discoveries; a comforting thought.

I extend my gratitude to my supervisors at the TU Delft, Davide Modesti and Delphine de Tavernier, for their invaluable assistance, insights, feedback, and suggestions. I always experienced our meetings as very pleasant, and your assistance played a crucial role in facilitating my smooth progress to the current state of this work.

Furthermore, I would like to thank Luc van Beek and Rikus van de Klippe, and everyone else I had the pleasure of meeting during my time at TouchWind. I always enjoyed the lengthy discussions on wind turbines, that occasionally took extensive detours. The atmosphere at TouchWind has always been great, and I am grateful for the opportunity I was given.

Finally, to the reader, I hope you enjoy the read. Please feel free to reach out to me; engaging in further discussions or providing clarifications about my work is something I will always appreciate and look forward to.

S. Hemelaar
Rotterdam, February 2024

Summary

While the assumption of incompressible flow has been the prevailing standard for numerical simulations of wind turbine aerodynamics, the limit of this assumption is approached as the industry progresses towards increasingly higher operational tip speeds. This thesis explores the implications of compressibility and transonic flow phenomena, particularly in relation to a new rotor design that integrates the concept of rotor tilt.

The study is split into two phases. The first phase involves two-dimensional Computational Fluid Dynamics (CFD) simulations, employing an Unsteady Reynolds Averaged Navier-Stokes (URANS) framework, specifically for the thick NACA 63(4)-421 airfoil. Attention is directed at the effects of high subsonic and transonic Mach numbers, and the complex flow phenomena emerging from shock wave-boundary layer interactions (SBLI). The second phase extends the findings from the first phase by simulating a 3MW concept rotor, utilizing a lifting line method. Here, particular emphasis lies on runaway conditions; the operating point of an unloaded rotor where rotational velocity maximizes. Since airfoil drag significantly increases through the onset of "shock-stall", it might provide a passive mechanism for overspeed protection.

The URANS study provides the first exploration of transonic buffet for a thick non-symmetrical airfoil; the phenomenon characterized by periodic shock movement, leading to large-scale load oscillations. The findings indicate that these fluctuations are significant and could pose a threat to the structural integrity of a full-scale rotor. Additionally, regarding the subcritical compressible regime, the study found that the von Karman-Tsien correction is the most appropriate method for the prediction of airfoil loads prior to reaching the critical boundary.

In the second phase, the rotor is simulated using the averaged values of the compressible aerodynamic coefficients, obtained in the first phase. Two flow scenarios are considered: Storm conditions typical for the North Sea, and subsequently, higher wind speeds often encountered during tropical typhoons in the Western Pacific. The results show that for the first scenario, shock-stall does not prevent the rotor from overspeeding. Instead, using rotor tilt is suggested as a more effective strategy. For the second scenario, a distinctive maximum rotational velocity has been found for an incoming wind speed of 57.5 m/s, leading to the conclusion that shock-stall could effectively prevent the rotor from overspeeding.

Since the averaged values of the aerodynamic coefficients are used to assess the adequateness of shock-stall as an overspeed protection mechanism, the load fluctuations attributed to transonic buffet are initially neglected. A subsequent preliminary assessment of these fluctuations revealed that operating in the high transonic regime potentially poses severe risks regarding rotor safety.

Contents

Preface iii

Summary v

Nomenclature xv

1 Introduction 1
- 1.1 Research Framework and Questions . . . 2
- 1.2 Thesis Outline . . . 3

I State of the Art

2 Aerodynamics of Compressible Flow 7
- 2.1 Fundamentals of Compressibility . . . 7
- 2.2 Corrections . . . 8
- 2.3 Shocked Flows . . . 10
  - 2.3.1 Transonic Shock Buffet . . . 12

3 Horizontal-Axis Wind Turbines 15
- 3.1 Local Supersonic Flow . . . 18

II 2D CFD

4 CFD: Methodology 23
- 4.1 Favre-Averaged Equations . . . 24
- 4.2 Turbulence Model . . . 26
  - 4.2.1 Model Selection . . . 27
- 4.3 Non-Dimensional Equations . . . 29
- 4.4 Finite Volume Solver . . . 31
  - 4.4.1 Solver Selection . . . 32
- 4.5 Computational Domain . . . 33
  - 4.5.1 Mesh Strategy . . . 33
  - 4.5.2 Boundary Conditions . . . 34
- 4.6 Design Space . . . 37

5 CFD: Verification/ Validation 41
- 5.1 Mesh Independence . . . 41
- 5.2 Low-Speed Validation . . . 44
  - 5.2.1 NACA 63(4)-421 . . . 44
  - 5.2.2 S809 . . . 45
- 5.3 High-Speed Validation . . . 46
  - 5.3.1 Steady Flow: RAE 2822 . . . 47
  - 5.3.2 Unsteady Flow: OAT15a . . . 48
- 5.4 Conclusion . . . 49

6 CFD: Results & Discussion 51
- 6.1 (Sub)critical Compressibility . . . 52
- 6.2 Transonic Flow & Buffet . . . 54
- 6.3 Polars . . . 57
  - 6.3.1 Stall . . . 58
- 6.4 Discussion . . . 59

III Lifting Line

7 Lifting Line: Methodology **63**
7.1 Computational Approach . . . 63
7.1.1 Potential Flow . . . 64
7.1.2 Perturbation Element: Vortex Filament . . . 66
7.1.3 Calculation of Blade Velocities . . . 67
7.1.4 Vortex Core Desingularization . . . 68
7.1.5 Iteration Loop for Bound Circulation . . . 68
7.2 Implementation . . . 69
7.2.1 Rotor Definition & Dicretization . . . 69
7.2.2 Polar Extrapolation . . . 70
7.2.3 Flow Conditions . . . 71

8 Lifting Line: Verification/ Validation **73**
8.1 Verification . . . 73
8.2 NREL Phase VI . . . 74
8.3 Mexico Project . . . 75
8.4 Conclusion . . . 76

9 Lifting Line: Results & Discussion **77**
9.1 Scenario 1: North Sea . . . 77
9.2 Scenario 2: Pacific . . . 79
9.3 Susceptibility to Buffet . . . 80
9.4 Discussion . . . 81

10 Conclusions **83**
10.1 Conclusions . . . 83
10.2 Recommendations . . . 85
10.2.1 Directions for Academic Research . . . 85
10.2.2 Engineering Design Recommandations . . . 85

References **87**

List of Figures

1.1 Side view **(a)** and front view **(b)** sketch of the TouchWind rotor concept. Incoming wind velocity is denoted by U_0 and rotor plane tilt angle by α_r. 2

2.1 Density ρ variations as function of Mach number M, according to the isentropic relations from Equation (2.3). 8
2.2 Critical Mach number calculation at $\alpha = 0°$ and $\alpha = 8°$ for **(a)** KU-109 and **(b)** KU-112F (adapted from Bonilla et al. [19]). 9
2.3 Sketch of flow development for NACA 63(4)-421 airfoil: Left side shows the airfoil at critical Mach number, whereas on the right, the Mach number is post-critical and a shock-wave emerges. 10
2.4 Sketch showing the effect of increasing the free stream Mach number M_∞ from sub- to supersonic on the drag coefficient C_d. 11
2.5 Lachman and Pearcy classification of shock-induced seperation (adapted from Lachmann and Pearcy [7]). 12
2.6 Lee's model for buffet of the second kind (adapted from Lee [8]). 13
2.7 Transonic Buffet Boundary and the effect on the lift coefficient C_l (adapted from Lee [27]). 14

3.1 Comparison of **(a)** Lift and **(b)** Drag Polars for EllipSys2D (Ell.) CFD Compressible, Incompressible & Corrected Incompressible Solution (adapted from Sørensen et al. [5]). 16
3.2 Comparison of power/ force results: **(a)** shows the BEM results for NREL 5-MW [33] by Yan and Archer [2] and **(b)** the span-wise tangential force distribution for the compressible & incompressible RANS Solution for IEA 15MW [35] by Cao et al. [3]. 17
3.3 Schematic of forces acting on a blade element: U_{rel} represents the incoming velocity by the blade element. $F_{l,comp}$ and $F_{d,comp}$ indicate the increase in lift and drag force from the Prandtl-Glauert correction. 17
3.4 BEM results for non-dimensional power coefficient C_p: **(a)** shows the results for the entire TSR range and **(b)** for lower TSR where the compressible solution leads to a higher C_P. $U_0 = 5$ & 15 m/s are omitted here to improve visibility. 18
3.5 Sub- and supersonic regime for NACA63(4)-421: **(a)** M_∞ vs C_p and **(b)** α vs M_∞ for $Re_c = 2.0 \times 10^6$, calculated using xFoil. Lines correspond with corrections to compressible C_p using indicated methods. 19

4.1 Diagram of flow models, based on the work of Jameson [38] and Peerlings [39]. 23
4.2 RMS pressure fluctuations for the RA16SC1 airfoil at $M_\infty = 0.732$, $Re_c = 4.2 \times 10^6$ and $\alpha = 4°$ (adapted from Concalves and Houdeville [48]). 27
4.3 Sketch of an arbitrary cell where the numerical fluxes are evaluated. 32
4.4 Blocking strategy for the C-mesh topology. 33
4.5 Geometry of the sponge zone within the computational domain. The hashed zone is evaluated without the damping term. 37
4.6 Conservative estimate of typical blade tip conditions for angle of attack α **(a)** and tip Mach number $M_{\infty,tip}$ **(b)** under varying tilt angle α_r. 38
4.7 Conservative estimate of typical flow conditions for angle of attack α **(a)** and chord-based Reynolds number Re_c **(b)**. 38
4.8 Design space for the CFD simulations. The subsonic (light blue) and supersonic (dark blue) regimes have been estimated using xFoil [68]. 39

5.1 Effect of grid refinement on the pressure coefficient C_p: **(a)** shows the continuous curve, whereas **(b)** provides a magnified view of the shock. $M_\infty = 0.65$, $Re_c = 18.0 \times 10^6$ and $\alpha = 0°$. 42

5.2 Effect of far field boundary distance on the pressure coefficient C_p for $x/c \in [0.1, 0.5]$: **(a)** shows suction side and **(b)** the pressure side. $M_\infty = 0.65$, $Re_c = 18.0 \times 10^6$ and $\alpha = 0°$. 42
5.3 Mean non-dimensional pressure field p_{mean}/p_∞ from coarsest (Grid 1) **(a)** to finest (Grid 4) **(d)** with Topology 3. $M_\infty = 0.65$, $Re_c = 18.0 \times 10^6$ and $\alpha = 0°$. 43
5.4 Selected C-mesh with grid dimensions 256×1002: **(a)** shows the entire computational domain and **(b)** an enlarged view around the NACA 63(4)-421 airfoil. 44
5.5 Airfoils considered for low-speed validation. 44
5.6 Lift **(a)** and drag **(b)** polars for NACA 63(4)-421 validation sequence at $Re_c = 9.0 \times 10^6$. For the URANS simulations the Mach number was set at $M_\infty = 0.2$. 45
5.7 Lift **(a)** and drag **(b)** polars for S809 validation sequence at $Re_c = 3.0 \times 10^6$. For the URANS simulations the Mach number was set at $M_\infty = 0.2$. 46
5.8 Airfoils considered for high-speed validation. 47
5.9 Pressure Coefficient C_p for the RAE 2822 airfoil. 47
5.10 Mach contours for *rhoEnergyFoam* **(a)** and *rhoPimpleFoam* **(b)** solvers. Black and red contours correspond to Spalart-Allmaras and Menter $k - \omega$ SST models, respectively. $M_\infty = 0.729$, $Re_c = 6.5 \times 10^6$ and $\alpha = 2.31°$. 48
5.11 Pre-buffet onset pressure coefficient C_p for the OAT15a airfoil. $M_\infty = 0.73$, $Re_c = 3.0 \times 10^6$ and $\alpha = 3.0°$. 48
5.12 Root-mean-square pressure fluctuations p_{rms} along the OAT15a airfoil at $M = 0.73$ and $Re = 3.0 \times 10^6$. Experimental data is from Ref. [26] and URANS from Ref. [10]. Negative x/c corresponds to the airfoils pressure side. 49

6.1 Influence of Mach number M_∞ on the flow field: **(a)** shows the effect on drag coefficient C_d, whereas **(b) - (e)** show the pressure field and streamlines for Mach numbers $M_\infty = \{0.60, 0.65, 0.70, 0.75\}$ at $Re_c = 18.0 \times 10^6$ and $\alpha = 0°$. 52
6.2 Comparison of minimal pressure coefficient $C_{p,min}$ from the compressibility corrections and the URANS simulations at $\alpha = \{-5°, 0°, 5°\}$ from **(a)-(c)** respectively at $Re_c = 18.0 \times 10^6$. The supersonic regime is derived from Equation (2.16). 53
6.3 Comparison of inviscid lift coefficient $C_{l,inv}$ from the compressibility corrections and the URANS simulations at $\alpha = \{-5°, 0°, 5°\}$ and $Re_c = 18.0 \times 10^6$. 54
6.4 Buffet fluctuations for lift coefficient C_l **(a)** and estimated critical and buffet boundary **(b)** for NACA 63(4)-421 airfoil at $Re_c = 18.0 \times 10^6$. 54
6.5 Buffet cycle of the NACA 63(4)-421 airfoil. Fluctuations of the aerodynamic coefficients are shown in **(a)**, whereas **(b) - (g)** provide numerical Schlieren ($\nabla\rho$) images with red lines marking the $u_1 = 0$ contour. $M_\infty = 0.65$, $Re_c = 18 \times 10^6$ and $\alpha = 2.5°$ 55
6.6 Buffet cycle of the NACA 63(4)-421 airfoil. Fluctuations of the aerodynamic coefficients are shown in **(a)**, whereas **(b) - (g)** provide numerical Schlieren ($\nabla\rho$) images with red lines marking the $u_1 = 0$ contour. $M_\infty = 0.725$, $Re_c = 18 \times 10^6$ and $\alpha = -1.25°$ 56
6.7 Calculated (URANS) field for mean lift coefficient $C_{l,mean}$ **(a)** and drag coefficient $C_{d,mean}$ **(b)** at $Re_c = 18.0 \times 10^6$. Contour projections are shown for sets $M_\infty = \{0.4, 0.65, 0.7, 0.75, 0.8\}$ and $\alpha = \{-5°, -2.5°, 0°, 2.5°, 5°\}$ 57
6.8 Lift and drag polar for the NACA63(4)-421 airfoil including stall region. $M_\infty = 0.20$ and $Re_c = 18.0 \times 10^6$ 58
6.9 Mean pressure field and streamlines for the NACA 63(4)-421 airfoil in stall region at $\alpha = 16°$ **(a)** and $\alpha = 20°$ **(b)**. $M_\infty = 0.20$ and $Re_c = 18.0 \times 10^6$ 59

7.1 Flow chart of the in-house lifting line code. 64
7.2 Basic singular solutions to the Laplace equation: **(a)** source/ sink, **(b)** doublet and **(c)** vortex. Sketches are based on the work of Katz and Plotkin [78]. 65
7.3 Sketch of the geometry of bound vortex filaments and shedded wake (adapted from van Garrel [79]). 66
7.4 Nomenclature for Biot-Savart law from Equation 7.13. 67
7.5 Geometry and discretization of the test rotor. 70
7.6 Extrapolation of lift and drag coefficients for NACA63(4)-421, as calculated by the Montgomerie [85], Aerodas [86] and Viterna [87] method. 70

8.1 Convergence of power coefficient C_P. Temporal development of C_P and torque Q shown in **(a)**, whereas **(b)** shows the convection of wake panels. $U_0 = 40$ m/s, $\alpha_r = 25°$ and $\lambda = 5.84$. 74
8.2 Power **(a)** and Thrust **(b)** at constant rotational speed ($\Omega = 72$ rpm) for NREL Phase VI turbine. Experimental data retrieved from Hand et al. [89] and URANS data from Hashem et al. [90]. 75
8.3 Azimuthal variations of normal force F_n **(a) - (c)** and tangential force F_t **(d) - (f)** for Mexico Rotor at radial stations $r/R = \{0.60, 0.82, 0.92\}$, where $U_0 = 15$ m/s, $\lambda = 6.67$ and $\psi = 30°$. 76

9.1 Power Coefficient C_P- curves for varying rotor plane tilt angle α_r at incoming wind speed $U_0 = 20$ m/s. 77
9.2 Radial distribution of tangential force $F_t{}'$ across a full rotation, as seen from above (rotation in counter-clockwise direction). Presented for incoming wind speeds $U_0 = 20$ m/s **(a)** and $U_0 = 30$ m/s **(b)**, evaluated at runaway tip speed ratio with a tilt angle of $\alpha_r = 30°$. 78
9.3 Tip speed ratio λ_{run} **(a)**, angular velocity Ω_{run} **(b)** at runaway for incoming wind speeds $U_0 \in [40, 60]$ at rotor plane tilt angles $\alpha = 10°, 15°$. 79
9.4 Power Coefficient C_P-curves for varying rotor plane tilt angle α_r at incoming wind speed $U_0 = 40$ m/s. 79
9.5 Tip speed ratio λ_{run} **(a)**, angular velocity Ω_{run} **(b)** and maximum tip Mach number M_{tip} **(c)** at runaway for incoming wind speeds $U_0 \in [40, 60]$ at rotor plane tilt angles $\alpha = \{10°, 15°\}$. 80
9.6 Local angle of attack α and Mach number M_∞ for rotor tip panel over a full rotation at runaway tip speed ratio λ_{run}. A point is plotted for every $d\phi = 10°$. 80
9.7 Tip region subjected to buffet. $U_0 = 60$ m/s, $\lambda = \lambda_{run}$ and $\alpha_r = 10°$ 81

List of Tables

4.1 Most common turbulence models for RANS [45]. 26
4.2 Turbulence models to be considered. 28
4.3 Lift and drag coefficient of RAE 2822 airfoil at $M_\infty = 0.729$, $Re_c = 6.5 \times 10^6$, $\alpha = 2.31$ [60] 32
4.4 Grid parameters considered for mesh independence. 34
4.5 C-mesh topology parameters (in dimensionless multiples of airfoil chord c) considered for mesh independance. 34

5.1 Aerodynamic coefficients obtained for mesh independence and topology study. 42
5.2 Aerodynamic coefficients for the NACA 63(4)-421 airfoil validation sequence at $Re_c = 9.0 \times 10^6$. Errors are calculated with respect to bold reference value. 45
5.3 Aerodynamic coefficients for the S809 airfoil validation sequence at $Re_c = 3.0 \times 10^6$. Errors are calculated with respect to bold reference value. 46
5.4 Aerodynamic coefficients for the RAE2822 airfoil validation sequence at $M_\infty = 0.729$ $Re_c = 6.5 \times 10^6$ and $\alpha = 2.31°$. 47
5.5 Qualitative assessment of the validation cases. 50

8.1 Airfoils spanning the MEXICO project rotor, including Reynolds number Re_c for available polar data. 75

Nomenclature

Abbreviations

Abbreviation	Definition
ABL	Atmospheric Boundary Layer
ALM	Actuator Line Model
BEM	Blade Element Momentum Theory
CFD	Computational Fluid Dynamics
DES	Detached Eddy Simulation
DNS	Direct Numerical Simulation
FANS	Favre Averaged Navier Stokes
HAWT	Horizontal Axis Wind Turbine
LES	Large Eddy Simulation
LL	Lifting Line
NS	Navier-Stokes
RANS	Reynolds Averaged Navier-Stokes
SBLI	Shock Boundary Layer Interactions
SST	Shear Stress Transport
TSR	Tip Speed Ratio
URANS	Unsteady Reynolds Averaged Navier Stokes

Dimensionless Groups

Symbol	Definition
C_d	Drag Coefficient; $F_d/q_\infty S$
ΔC_d	Buffet Amplitude of Drag Coefficient
C_l	Lift Coefficient; $F_l/q_\infty S$
ΔC_l	Buffet Amplitude of Lift Coefficient
C_P	Rotor Power Coefficient; $P/\frac{1}{2}\rho A {U_0}^3$
C_p	Pressure Coefficient; $(p-p_\infty)/q_\infty$
C_T	Rotor Thrust Coefficient; $T/\frac{1}{2}\rho A {U_0}^2$
k_r	Reduced Frequency of Buffet Fluctuations; $\frac{2\pi f(c/2)}{U_\infty}$
M	Mach Number; u/c
Pr	Prandtl Number; $c_p\mu/k$
Pr_t	Turbulent Prandtl Number
Re_c	Chord Reynolds Number; $\rho u_\infty c/\mu_\infty$
γ	Specific Heat Ratio; c_p/c_v
λ	Tip Speed Ratio; $\Omega R/U_0$

Latin Symbols

Symbol	Definition	Unit
$\mathbf{F}_e$	Eulerian Flux Vector	-
$\mathbf{F}_v$	Viscous Flux Vector	-
$\mathbf{n}_1$	Chordwise Unit Vector	-
$\mathbf{n}_2$	Chordnormal Unit Vector	-
$\mathbf{u}$ / $\boldsymbol{U}$	Velocity Vector	m/s
$\mathbf{W}$	Vector of Conserved Variables	-
A	Swept Rotor Area	m^2
E	Total Energy; $E = e + \frac{1}{2}u^2$	J
F_d	Drag Force	N
F_l	Lift Force	N
F_n	Normal (Axial) Force	N
F_t	Tangential (Azimuthal) Force	N
H	Total enthalpy per Unit Mass; $H = h + \frac{1}{2}u^2$	J/kg
P	Rotor Power	W
Q	Rotor Torque	Nm
R	Rotor Radius; $R = \frac{1}{2}D$	m
S_{ij}	Strain Tensor	s^{-1}
T	Rotor Thrust	N
U_0	Incoming Wind Speed Rotor	m/s
a	Axial Induction	-
a'	Tangential Induction	-
c	Speed of sound	m/s
c	Airfoil Chord Length	m/s
c_p	Specific Heat at Constant Pressure	$\mathrm{J\,kg^{-1}K^{-1}}$
c_v	Specific Heat at Constant Volume	$\mathrm{J\,kg^{-1}K^{-1}}$
f	Buffet Frequency	s^{-1}

Symbol	Definition	Unit
k	Thermal Conductivity	W m^{-1}K^{-1}
k	Turbulence Kinetic Energy ($k-\omega$ models)	m^2/s^2
p	Pressure	Pa
$\bar{q}$	Reynolds Averaged Quantity	-
$\tilde{q}$	Favre Averaged Quantity	-
q'	Fluctuating Quantity (Favre)	-
q''	Fluctuating Quantity (Reynolds)	-
q_j	Heat Flux Components	W/m^2
q_j^t	Turbulent Heat Flux Components	W/m^2
s	Entropy	J/K
t	Time	s
u_i	Velocity Components (Einstein Notation)	m/s
v	Control Volume	m^3
$x_{k,damp}$	Damping Factor for Sponge Zone	-
y^+	Dimensionless Wall Distance	-

Greek Symbols

Symbol	Definition	Unit
α	Angle of Attack	rad
α_ℓ	Runge Kutta Scheme Constants	-
α_r	Rotor Plane tilt angle	rad
α_t	Turbulent Thermal Diffusivity	m^2/s
Γ	Circulation	m^2/s
ϵ	Error against Experimental Data	-
θ	Rotor Pitch Angle	rad
μ	Dynamic Viscosity	Pa s
μ_t	Dynamic Eddy Viscosity	Pa s
ν	Kinematic Viscosity	m^2/s
$\tilde{\nu}$	Eddy Viscosity Parameter (Spalart-Allmaras)	m^2/s
ν_t	Kinematic Eddy Viscosity	m^2/s
ξ	Average Compressibility Factor	-
ρ	Density	kg/m^3
sigma	Turbulent-Viscous Stress Tensor	Pa
τ	Compressibility of a Fluid	Pa^{-1}
τ_{ij}	Total Viscous Stresses	Pa
τ_{ij}^t	Reynolds Stresses	Pa
ϕ	Azimuthal Rotor Blade Position	rad
$\hat{\phi}$	Linearized Velocity Potential	m^2/s
Φ	Velocity Potential	m^2/s
ψ	Rotor Yaw Angle	rad
ω	Specific turbulence dissipation	s^{-1}
Ω	Angular velocity / Mean Vorticity	rad/s

Subscripts

Script	Definition
$*$	Dimensional Quantity
∞	Free Stream Conditions
$comp$	Compressible Coefficients
$crit$	Critical (Sonic) Conditions
inc	Incompressible Coefficients
max	Maximum Value

Script	**Definition**
$mean$	Mean Value
min	Minimum Value
rms	Root Mean Squared Values
run	Runaway Conditions (Unloaded Rotor)
t / 0	Total Conditions
θ	Azimuthal Component

1 Introduction

As the world continues to look for ways to reduce carbon emissions, wind turbines are expected to play an increasingly important role in meeting energy demands [1]. As wind turbine designs continue to evolve and rotor diameters increase, new challenges arise. One of these challenges is the effect of compressibility. While compressibility has been studied extensively in the field of aerospace engineering for fixed wing applications, the assumption of incompressible flow has been a prevailing standard in the field of wind turbine aerodynamics.

Nevertheless, recent studies have shown an increasing interest in these effects in the context of Horizontal Axis Wind Turbines (HAWTs). Various methods have been employed to gain insights into the implications of compressibility. Yan and Archer [2] used a Blade Element Momentum (BEM) approach to quantitatively assess performance losses, while other studies, such as Cao et al. [3], implemented full three-dimensional Computational Fluid Dynamics (CFD) methods. The findings show considerable disparities, suggesting that the subject is still in its early stages. However, the studies collectively suggest the impact of compressibility effects will become significant and can no longer be ignored.

As the focus on compressibility effects for subsonic flow gain more attention, the exploration of even higher flow velocities; entering the transonic regime, remains limited. For a structure that is subjected to these velocities, the flow will be characterized by a region where the local velocity exceeds the speed of sound, ultimately collapsing into a shock wave. This significantly impacts the forces exerted on the affected structure. Research specifically devoted to the effects of local supersonic flows on wind turbine blades is limited. A pioneering study by De Tavenier and von Terzi [4] suggests that large HAWTs are likely to encounter supersonic flow in the future, yet the full scope and implications of these phenomena are not thoroughly understood or investigated.

This thesis will address fundamental implications of compressible and transonic flow in the context of wind turbine aerodynamics. However, the studied rotor, is not a traditional HAWT. Instead, this research will explore a variation of the conventional design by introducing rotor tilt. This modification offers significant benefits and is currently under development by TouchWind B.V., the company affiliated with this research, and from here on referred to as "the company". While the concept shares several similarities with conventional HAWTs, the key difference is its ability to tilt the rotor over its horizontal axis. A sketch of the design is given in Figure 1.1. Two key advantages arise from this configuration:

- Conventional HAWTs use pitch control to maintain constant power output when wind speed increases beyond its rated wind speed. However, blade pitching is limited, and beyond its cut-off wind speed the rotor must cease operation. In contrast, a turbine design implementing a tilt mechanism can reduce its effective surface area, potentially to zero. This feature enables the rotor to maintain power production beyond the cut-off wind speeds typical for conventional HAWTs. The company's goal has been set to maintain operation for wind speeds up to 70 m/s.
- A rotor produces thrust in axial direction. When a tilt angle is implemented, the resulting force on the flow causes the wake to be deflected downwards, creating a suction effect for higher flow layers. In a park configuration, this can lead to increased wind speeds for subsequent turbines, improving the total power output. This effect is relevant for incoming wind speeds below the rated wind speed, and therefor, out of the scope of this work.

Figure 1.1b illustrates that tilt introduces azimuthal variations of the local velocity perceived by the blades. Over a full rotation, the blades will go through an *advancing motion*; into the direction of incoming wind, and a *retreating motion*; following the wind direction. This design aspect leads to increased local velocities on the advancing side. Coupled with the desire to operate under high wind speeds at a high tip speed ratio, it becomes evident that this design is even more susceptible to compressibility effects compared to conventional HAWTs.

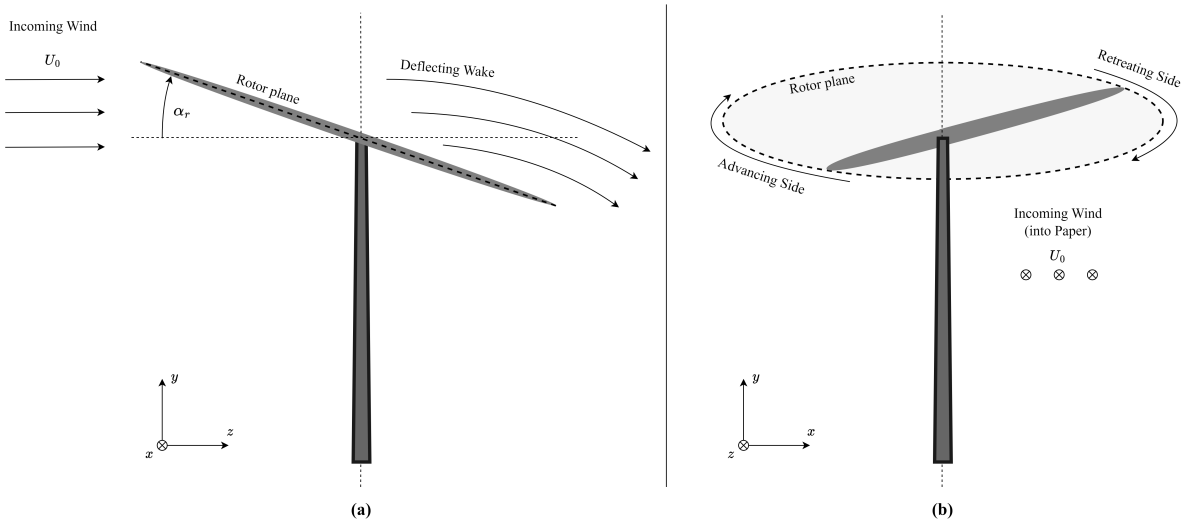

Figure 1.1: Side view **(a)** and front view **(b)** sketch of the TouchWind rotor concept. Incoming wind velocity is denoted by U_0 and rotor plane tilt angle by α_r.

Compressibility effects and the emergence of shock waves are generally deemed detrimental; degrading rotor performance and posing risks to structural integrity [2, 3, 5]. However, the significant increase in drag associated with the action "shock-stall", might offer a solution regarding rotor safety as well. In the case of generator failure, rotational velocity increases towards the operating point for an unloaded rotor, a condition referred to as *runaway*. The strong increase in drag from shock-stall might act as a passive overspeed protection mechanism. This hypothesis has been explored once by Wood [6] in the context of small HAWTs (3 kW) using a BEM method. His findings showed that the onset of shock-stall occurred too late to effectively prevent overspeeding. However, given the unique design aspects of the turbine under study, which includes rotor tilt, the implementation of a thicker airfoil, and operation at high tip speeds, it is reasonable to reassess this hypothesis.

Shock-stall originates from a strong adverse pressure gradient associated with the shock, inducing flow separation. The mechanism is intricately linked to the interaction between the shock and boundary layer; complex phenomena known as shock wave-boundary layer interactions (SBLIs). Lachmann and Pearcy [7] have conducted extensive studies on these mechanisms and have systematically categorized them according to the origin of separation. Furthermore, the interactions can trigger the onset of transonic buffet, a phenomenon characterized by periodic shock movement, leading to large-scale load oscillations. The prevailing theory regarding the governing physics of this unsteady phenomenon, as first proposed by Lee [8], is the presence of strong SBLIs combined with a subsonic flow region downstream, which allows for acoustic pressure waves to travel upstream and interact with the shock. Investigations into buffeting have primarily focused on supercritical airfoils, and successes have been achieved in modelling the load fluctuations through CFD methods, as demonstrated in the works of Iovnovich and Revah [9], and Thiery and Coustols [10]. In the context of thick airfoils that are typical for wind turbine blades, this behavior has not been studied. The load fluctuations associated with buffet typically reach great magnitudes, and could potentially pose severe risks to the structural integrity of a wind turbine.

1.1. Research Framework and Questions

A straight-forward approach to analyze the effects of compressibility and transonic flow would be to conduct an extensive three-dimensional CFD study. However, this strategy presents several challenges.

Firstly, it is a computationally intensive approach, which restricts the number of configurations that can be examined. Additionally, there is a notable gap in academic research regarding compressibility effects for thick airfoils in general. Therefore, attention is directed first towards understanding these effects and obtaining the resulting loads at a two-dimensional level. The current design airfoil used by the company is the NACA 63(4)-421; a thick airfoil typical for wind turbine blades. The analysis requires a CFD approach that can capture the complex nature of SBLIs. This is achieved through the implementation of an Unsteady Reynolds Averaged Navier Stokes (URANS) framework. The first phase of this research involves:

Phase 1: Rotor aerodynamics are ignored. Compressibility and transonic effects are studied in 2D for the NACA 63(4)-421 airfoil. The fundamental steps of this phase consist of:

(1) Establishment of a design space: i.e., a range of angles of attack and Mach numbers where the full-scale rotor will be subjected to in the compressible and transonic flow regime.

(2) URANS simulations are executed for the design space.

(3) Conclusions can be drawn from the acquired data. Lift and drag polars are obtained for varying inflow Mach numbers. These polars will contain the impact on the loads from compressibility effects, shock waves and buffeting.

Subsequently, the performance of the 3D rotor can be modeled using a lower-fidelity method, considering the requirement of simulating numerous configurations. Three potential methods for this analysis are available: A panel method, a BEM method, and a lifting line method. Firstly, panel methods can be excluded, as they represent the rotor using a series of doublets that describe the flow field around the blades under the assumption of incompressible flow. Both BEM and lifting line methods rely on airfoil polar data, making them suitable for the approach of this study. BEM however, relies on the principle of annular independence. As indicated by Schepers [11], the assumption of the induced velocities being independent of azimuthal variations, limits the accuracy of BEM for yawed flows. Given that this research intends to investigate highly non-axial inflow conditions, BEM is deemed unsuitable. This narrows the choice to the lifting line method, which is not limited to axial inflow. The second phase of this research involves the following:

Phase 2: The company's rotor concept will be modeled in 3D. This phase consists of the following fundamental steps:

(1) The company's in-house lifting line code with free wake model is utilized. The lift and drag polars acquired in Phase 1 are implemented in this model.

(2) Cases of an unloaded rotor, where angular velocity increases towards runaway, will be examined to assess whether the onset of shocks can act as an over-speed protection mechanism.

(3) It is assessed whether the rotor is susceptible to the unsteady load oscillations associated with transonic buffet, and the potential consequences are examined.

From the research framework outlined above, a set of research questions can be established. These are split into two primary questions, where **Q-1** corresponds with the first phase of the research and **Q-2** with the second phase. The primary research questions, along with their associated sub-questions, are presented on the next page.

1.2. Thesis Outline

This thesis is composed of three parts, with Part I dedicated to presenting the current state of the art, segmented into two chapters. Chapter 2 delves into the fundamentals of compressible and shocked flows. Subsequently, Chapter 3 presents a comprehensive review for HAWTs in relation to compressibility.

Following the foundational chapters, Parts II and III constitute the main body of this research. Part II is dedicated to the CFD analysis at airfoil level, whereas Part III focuses on the lifting line method for the full rotor. Each part commences with a methodology chapter, outlining the equations that describe the problems, and the specific problems they address. This is followed by a validation chapter to ensure the accuracy and reliability of the solutions. The parts conclude with a results chapter, which includes a discussion of the findings.

The thesis concludes with Chapter 10, encompassing both conclusions from this study and recommendations for future work.

Q-1 What is the influence of high subsonic and transonic Mach numbers on the loads for the thick NACA 63(4)-421 airfoil, typical for wind turbine blade applications?

- Q-1-1 To what extent can corrections to the incompressible aerodynamic coefficients accurately model the compressible coefficients?
- Q-1-2 Under which flow conditions can we expect shock-wave formation and transonic buffet, and how do these influence the loads?

Q-2 How do the effects of compressibility, shocked flow, and transonic buffet impact performance and operational safety of a tilted wind turbine under extreme wind conditions?

- Q-2.1 Under what conditions can the action of shock-stall function as a passive overspeed protection mechanism for an unloaded rotor?
- Q-2.2 For which conditions will the rotor be susceptible to transonic buffet, and what are the resulting implications on rotor loading?

Part I

STATE OF THE ART

2

Aerodynamics of Compressible Flow

This section provides a comprehensive review of the fundamental aerodynamic principles underpinning compressible and transonic flow. An examination of several corrections applicable to incompressible theory will be given in Section 2.2. Subsequently, focus will shift towards shocked flows, where simple corrections are no longer valid. However, let us start by introducing some fundamental concepts of compressibility.

2.1. Fundamentals of Compressibility

The degree of compressibility for a given fluid can be described by Equation (2.1). In this expression, v is a control volume for which the pressure is increased by an infinitesimal small dp. The resulting decrease in volume dv, determines the compressibility of that fluid, which is denoted by τ.

$$\tau = -\frac{1}{v}\frac{dv}{dp}, \tag{2.1}$$

To assess the properties of a fluid which flows around an object, we can redefine v as a specific volume $v' = 1/\rho$. Substituting into Equation (2.1), we obtain an expression in terms of the change in density ρ.

$$\tau = \frac{1}{\rho}\frac{d\rho}{dp}, \tag{2.2}$$

From this expression, it can be concluded that an increase in pressure results in an increase in density, and this density increase is dependent on the fluids' compressibility τ. For flows of sufficiently low velocity, referred to as *low-speed flows*, the fluctuations in pressure dp are sufficiently small to assume the variations in density ρ to be negligible. This is referred to as *incompressible flow*. The question remains for which conditions the incompressible flow assumption remains valid. Anderson [12] derives this limit as follows: Consider a fluid particle at rest which is isentropically accelerated. At $t = 0$ the density ρ is equal to the total density ρ_t. During acceleration, the density will decrease according to Equation (2.3). In this equation, the specific heat ratio is given by $\gamma = 1.4$ for a diatomic gas.

$$\frac{\rho}{\rho_t} = \left(1 + \frac{\gamma - 1}{2}M^2\right)^{-1/(\gamma-1)}, \tag{2.3}$$

Furthermore, M denotes the Mach number, which represents the ratio between the velocity u of an object in a fluid and the speed of sound c within that fluid, where the speed of sound is measured in the free stream. This relationship is given by Equation (2.4).

$$M = \frac{u}{c}; \tag{2.4}$$

$$c = \sqrt{\left.\frac{\partial p}{\partial \rho}\right|_s}, \tag{2.5}$$

In turn, the speed of sound c can be related to the partial derivative of pressure p with respect to density ρ, evaluated at constant entropy s. When Equation (2.3) is plotted in Figure 2.1, it can be observed that the curve has a relatively low gradient for low Mach numbers, and it increases gradually. For Mach

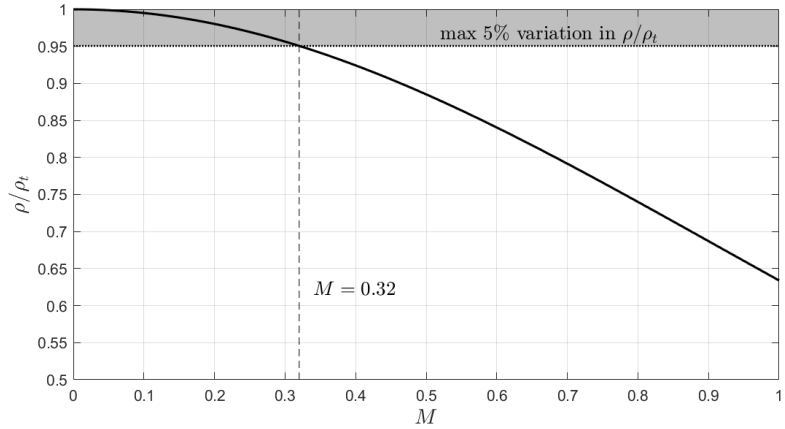

Figure 2.1: Density ρ variations as function of Mach number M, according to the isentropic relations from Equation (2.3).

number up to $M = 0.32$, the deviation between ρ and ρ_t peaks at 5%. Anderson [12] states that for the majority of applications, it is reasonable to consider the flow as incompressible within this range. Although it has no physical meaning, a Mach number of $M = 0.3$ is commonly accepted as the upper threshold beyond which the assumption of incompressible flow no longer holds. It's important to note that the Mach number M serves as a measure of the magnitude of compressibility effects, often being preferred over the use of a fluid's compressibility τ from Equation (2.2).

This thesis focuses on the tip region of a turbine. For conventional wind turbines, under operation the tips can reach velocities of 120 m/s [3], equating to a Mach number of approximately 0.33. The incompressible assumption is not valid for this regime, and methods to account for compressibility should be implemented.

2.2. Corrections

As can be concluded from Figure 2.1, compressibility effects should be considered when the flow velocity exceeds $M = 0.3$. This significantly complicates the governing equations describing fluid flow, since density ρ becomes a function of the local pressure p and temperature T. To avoid the need to solve for this additional variable, several corrections to the incompressible solution have been developed. These corrections provide a simple transformation from the incompressible to the compressible coefficients. The three most used corrections; Prandtl-Glauert, Karman-Tsien and Laitone, will be briefly explained first.

The emergence of propeller jet engines at the end of WWI led to an increasing interest in high Mach numbers at propeller tips. Although Ludwig Prandtl had already taught the transformation in his lectures, Glauert [13] was first to publish a proof in 1928 that is now known as the *Prandtl-Glauert compressibility correction*. The correction is derived from the linearized perturbation velocity potential, which is given by Equation (2.6) below. The entire derivation can be found in the work of Anderson [12]. The correction is given by Equation (2.7). Here, $C_{p,comp}$ and $C_{p,inc}$ represent the compressible and incompressible pressure coefficient, respectively.

$$(1 - M_\infty^2)\frac{\partial^2 \hat{\phi}}{\partial x^2} + \frac{\partial^2 \hat{\phi}}{\partial y^2} = 0, \tag{2.6}$$

$$C_{p,comp} = \frac{C_{p,inc}}{\sqrt{1 - M_\infty^2}} \tag{2.7}$$

For an inviscid flow, the drag, and lift forces on a body are integrals of the pressure distribution on that body. Additionally, the lift and moment coefficients are integrals of the pressure coefficient. Since, Equation (2.7) relates the incompressible and compressible pressure coefficients by a linear relation, the same must hold for the coefficients of lift and drag, as given by Equations (2.8) and (2.9). This is a powerful property of the Prandtl-Glauert correction compared to the Karman-Tsien and Laitone rule described below, which include non-linear terms. Here, the corrections must be applied to the pressure

coefficient first. Subsequently, the pressure components of the lift and drag coefficients can be found from integration over the airfoil surface.

$$C_{l,comp} = \frac{C_{d,inc}}{\sqrt{1 - M_\infty^2}}, \tag{2.8}$$

$$C_{d,comp} = \frac{C_{d,inc}}{\sqrt{1 - M_\infty^2}}, \tag{2.9}$$

The first attempt to improve the Prandtl-Glauert correction was achieved by the combined work of Tsien [14] and von Karman [15] early in the 1940s. Since the Prandtl-Glauert correction is completely based upon linear theory, the work of Tsien and von Karman captures some aspects of non-linearities. The correction, known as the *Karman-Tsien compressibility correction*, is given by (2.10).

$$C_{p,c} = \frac{C_{p,i}}{\sqrt{1 - M_\infty^2} + \left[M_\infty^2 / \left(1 + \sqrt{1 - M_\infty^2}\right)\right] C_{p,i}/2}, \tag{2.10}$$

Finally, the most recent attempt of improving the accuracy of the corrections was done by Laitone [16] in 1951. Instead of using the free stream Mach number, the local Mach number is used to derive the relation given by Equation (2.11).

$$C_{p,c} = \frac{C_{p,i}}{\sqrt{1 - M_\infty^2} + \left[\frac{1}{2} M_\infty^2 \left\{1 + ((\gamma - 1)/2) M_\infty^2\right\} \sqrt{1 - M_\infty^2}\right] C_{p,i}}, \tag{2.11}$$

Vos and Farokhi [17] applied the compressibility corrections mentioned above to the transonic experimental data for the NACA 4421 airfoil [18]. It is shown that the addition of extra terms increases the accuracy of the corrections. Karman-Tsien results in the most accurate match with the experimental data, followed by Laitone and Prandtl-Glauert, which respectively under- and overpredict the pressure coefficient.

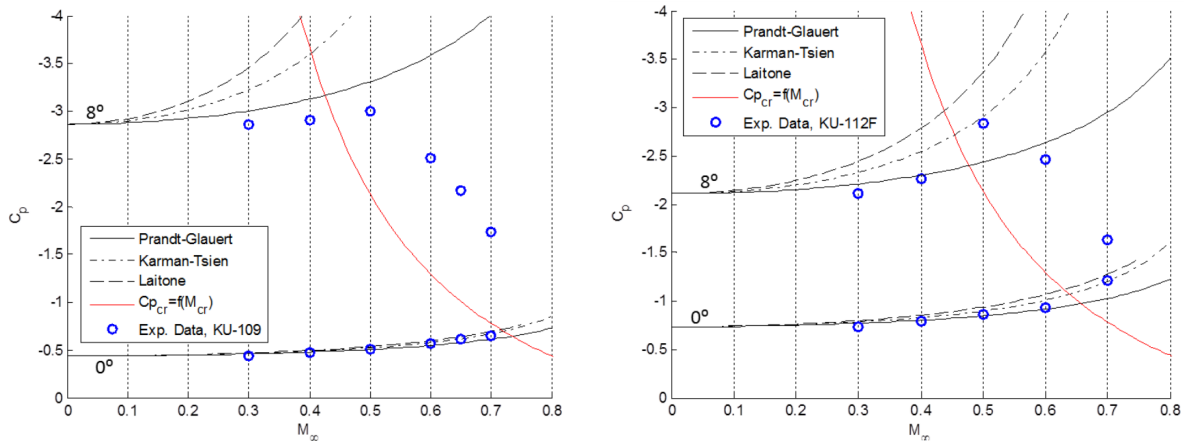

Figure 2.2: Critical Mach number calculation at $\alpha = 0°$ and $\alpha = 8°$ for **(a)** KU-109 and **(b)** KU-112F (adapted from Bonilla et al. [19]).

Furthermore, Bonilla et al. [19] studied the compressibility corrections, assessing their accuracy to predict the aerodynamic coefficients for rotor-craft airfoils. They experimentally tested two airfoils: The KU-112F, designed for high maximum lift near the root, and the KU-109, designed for higher drag divergence Mach number M_{DD} (refer to Section 2.3) in the rotor tip region. The experiments were executed for a range of transonic free stream Mach number from sub- to supercritical conditions: $0.3 < M_\infty < 0.7$. Their method to assess the quality of the compressibility corrections involves their ability to predict the critical pressure coefficient $C_{p,crit}$ (refer to Equation (2.16)); i.e., the pressure

coefficient for the onset of local supersonic flow. The experimental results are shown in Figure 2.2 for an angle of attack of $\alpha = 0°$ and $\alpha = 8°$. The minimum pressure coefficient found from the experiments at $M_\infty = 0.3$ is taken as the incompressible pressure coefficient. The compressibility corrections (equations (2.7), (2.10) and (2.11)) are subsequently applied to this value to obtain the curves in Figure 2.2. For lower Mach numbers at zero angle of attack, all corrections provide good accuracy at predicting the minimum pressure coefficient up to the critical regime. For high angle of attack, the accuracy reduces greatly. Only the Prandtl-Glauert correction gives an acceptable prediction before reaching critical conditions. Hence, Bonilla et al. [19] conclude that the Prandtl-Glauert correction most accurately predicts the pressure coefficient for pre-critical conditions.

Wang et al. [20] reviewed the compressibility corrections for the application of an underwater body tested in a wind tunnel. Hence, the corrections are applied to transform the compressible to the incompressible pressure coefficient. They defined an average compressibility factor ξ (2.12), where η_{cor} and η_{uncor} denotes the compressibility error measured at 4 points of interest around the object's surface.

$$\xi = 1 - \frac{\overline{\eta_{cor}}}{\overline{\eta_{uncor}}}, \tag{2.12}$$

Their findings show that $\xi_{PG} = 0.51$, $\xi_{KT} = 0.38$ and $\xi_{Lai} = 0.23$. Therefore, the Prandtl-Glauert correction is the most accurate. However, none of the corrections perform great for the application described above.

In summary, compressibility corrections are a useful tool to predict flow behavior in the subsonic regime (i.e. no shocked flows). However, it should be noted that the type of application greatly determines their effectiveness, and which correction (Prandtl-Glauert, Karman-Tsien, Laitone) gives the most accurate results.

2.3. Shocked Flows

As can be observed in Figure 2.2, the compressibility corrections become inadequate when the flow velocity exceeds the critical Mach number. This is expected since the flow characteristics change greatly when shock waves emerge. Figure 2.3 shows that for a free stream Mach number higher than the critical Mach number M_{crit}, a shock wave will occur. First, the flow accelerates over the airfoil surface to supersonic speeds, subsequently leading to a compression wave characterized by a rapid increase in pressure.

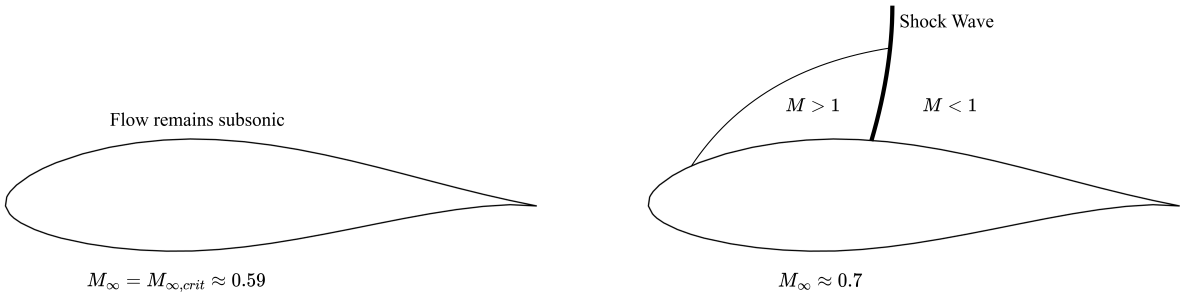

Figure 2.3: Sketch of flow development for NACA 63(4)-421 airfoil: Left side shows the airfoil at critical Mach number, whereas on the right, the Mach number is post-critical and a shock-wave emerges.

Firstly, it is important to understand when the flow will be subjected to shock waves. In the previous subsection 2.2 it was briefly mentioned that shocks occur when the critical pressure coefficient $C_{p,crit}$ is reached. Using the isentropic relations, the local pressure at an arbitrary point A can be calculated from the total pressure p_0 using Equation (2.13).

$$\frac{p_0}{p_A} = \left(1 + \frac{\gamma - 1}{2} M_A^2\right)^{\gamma/(\gamma-1)}, \tag{2.13}$$

Subsequently dividing by the expression corresponding to the free stream pressure, we find:

$$\frac{p_A}{p_\infty} = \frac{p_A/p_0}{p_\infty/p_0} = \left(\frac{1 + ((\gamma-1)/2)M_\infty^2}{1 + ((\gamma-1)/2)M_A^2}\right)^{\gamma/(\gamma-1)}, \tag{2.14}$$

Now, we introduce the non-dimensional pressure coefficient C_p, evaluated at point A.

$$C_{p,A} = \frac{2}{\gamma M_\infty^2} \left(\frac{p_A}{p_\infty} - 1 \right), \tag{2.15}$$

Substituting Equation (2.14) into (2.15), and taking $M_A = 1$, an expression for the critical pressure coefficient $C_{p,crit}$ is obtained. That is, the pressure coefficient corresponding to the flow reaching the critical free stream Mach number M_{crit}.

$$C_{p,\text{ crit}} = \frac{2}{\gamma M_\infty^2} \left(\left[\frac{1 + \frac{1}{2}(\gamma - 1) M_\infty^2}{1 + \frac{1}{2}(\gamma - 1)} \right]^{\frac{\gamma}{\gamma - 1}} - 1 \right), \tag{2.16}$$

In summary, the critical Mach number M_{crit} is defined as the Mach number, for which the sonic conditions ($M = 1$) occur at some point on the airfoil. The value for M_{crit} is dependent on the airfoil geometry and angle of attack α. Viscous effects have not been considered in this analysis so far. Nevertheless, to a lesser extent, the critical Mach number is also dependent on the boundary layer development, and thus the chord-based Reynolds number Re_c.

The flow characteristics around an airfoil are strongly dependent on the interaction between the shock wave and boundary layer, which is referred to as *shock wave-boundary layer interactions* (SBLIs). In the presence of a weak shock, the flow remains attached to the airfoil surface. This is referred to as a *weak interaction*. When the strength of the shock increases, the flow separates behind the shock, corresponding to a *strong interaction*. Furthermore, the nature of the interaction is related to the boundary layer type (laminar or turbulent); a shocked laminar boundary layer will separate earlier (according to wind tunnel results from Lachmann and Pearcy [7]).

Figure 2.4 shows a sketch of the drag coefficient C_d for an airfoil that is subjected to a free stream Mach number M_∞. In the subsonic flow regime, the drag coefficient experiences a gradual increase as a result of subsonic compressibility effects. This rate of increase becomes more pronounced once the flow exceeds the critical Mach number M_{crit}, attributed to *wave drag*; a component of pressure drag. Shortly after surpassing the critical Mach number, the drag divergence Mach number M_{DD} is encountered, indicating the point where the drag gradient becomes significantly higher. This juncture signifies that the SBLI has reached sufficient strength to induce flow separation. The peak drag coefficient $C_{d,max}$ is attained when the flow surrounding the airfoil is fully supersonic, a condition often referred to as the sound barrier. Beyond this point, the drag coefficient starts to decline.

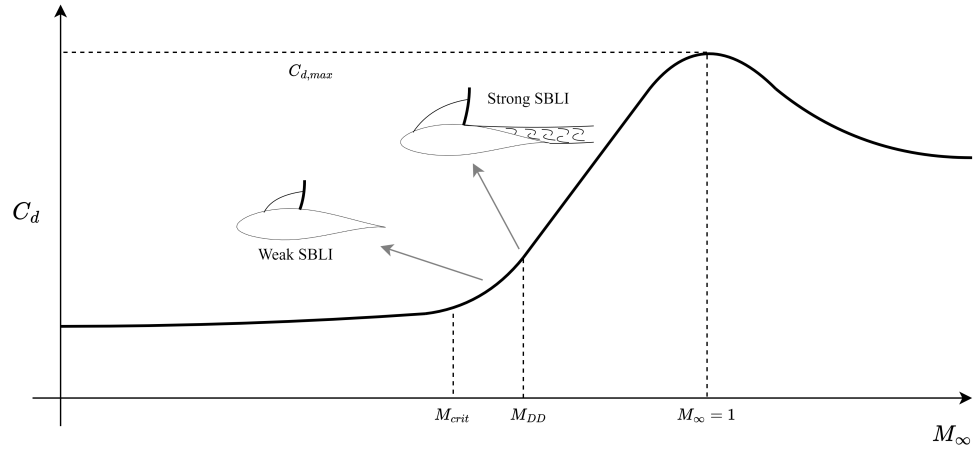

Figure 2.4: Sketch showing the effect of increasing the free stream Mach number M_∞ from sub- to supersonic on the drag coefficient C_d.

Since shock-induced separation is a driving factor regarding the lift and drag an airfoil produces, it is important to understand the mechanisms. In essence, the strong adverse pressure gradient induced by the shock wave may lead to flow separation. Lachmann and Pearcy [7] identified two types of flow separation induced by the SBLIs:

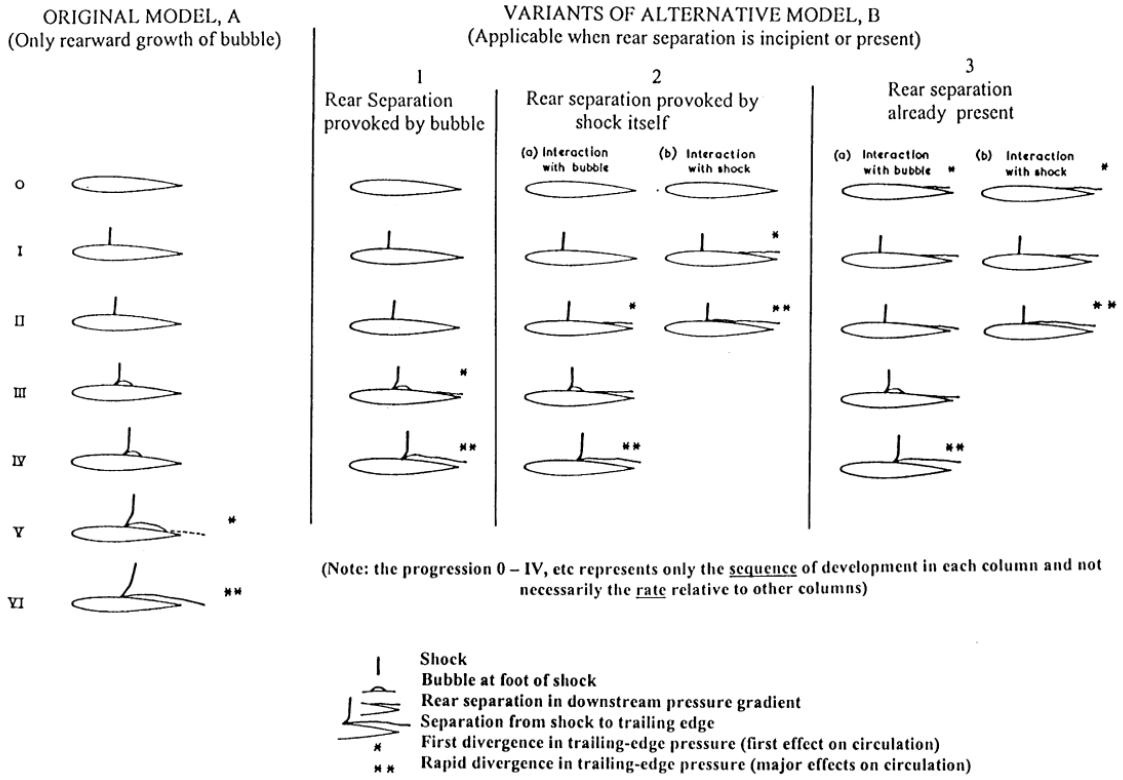

Figure 2.5: Lachman and Pearcy classification of shock-induced seperation (adapted from Lachmann and Pearcy [7]).

Model A: A separation bubble forms underneath the shock-wave, after which the boundary layer manages to reattach downstream. When the shock strength is increased, the flow completely breaks down, causing separation all the way towards the trailing edge. This phenomenon is commonly known as *shock-stall*, characterized by an abrupt loss of lift and an increase in drag.

Model B: Due to the adverse pressure gradient of the shock-wave, the boundary layer thickens, but the flow does not separate at the shock foot. Due to the thickened boundary layer, however, the flow separates at the trailing edge. When the strength of the shock increases, the separation area expands from the trailing edge towards the shock foot.

Model B can be subdivided into several variations, which are graphically shown in Figure 2.5. According to Babinsky and Harvey [21], a small separation bubble close to the shock wave will have a much less predominant effect on the lift and drag compared to separation at the trailing edge.

2.3.1. Transonic Shock Buffet

Although the principles of SBLIs described above might be viewed as steady phenomena, separation of the boundary layer is characterized by the onset of periodic shock movement, which is referred to as *transonic shock buffet*, or simply, *transonic buffet*. Gianellis et al. [22] published an overview of the recent developments in the understanding of the phenomenon. They indicate that, despite over six decades of research, the governing physics of transonic shock buffeting are still not fully understood. Nevertheless, numerous methods have been developed to predict the behavior of transonic buffeting.

Two main types of shock buffet have been identified: Type I typically occurs for biconvex airfoils around zero angle of attack. An oscillating shock wave is present on both the suction and pressure side. The shock on the upper and lower surface produce a self-sustained oscillatory motion, where the shock strength and position vary with a 180° phase shift. This type of buffeting can be modelled well owing to the work of Mabey [23] and Gibb [24]. Type 2 buffeting is characterized by an oscillating shock wave on the airfoils suction side, and is not limited to zero angle of attack. No academic consensus is reached regarding modelling of the second type. Buffet can be categorized further, as described by Tijdeman [25]. This classification is based on the predominant characteristic of shock motion. These types are:

Type A: Characterized by a sinusoidal shock movement, where the shock remains continuously present throughout its cycle.

Type B: The shock still periodically oscillates up- and downstream. However, as the shock reaches its upstream positions, it transitions into a weak compression wave. The magnitude of the load oscillations for Type B is larger compared to Type A.

Type C: The shock moves in upstream direction exclusively. As the shock departs from the leading edge, it generates other compression waves that ultimately form a new shock wave. Type C is notable for having the largest oscillations among the three types.

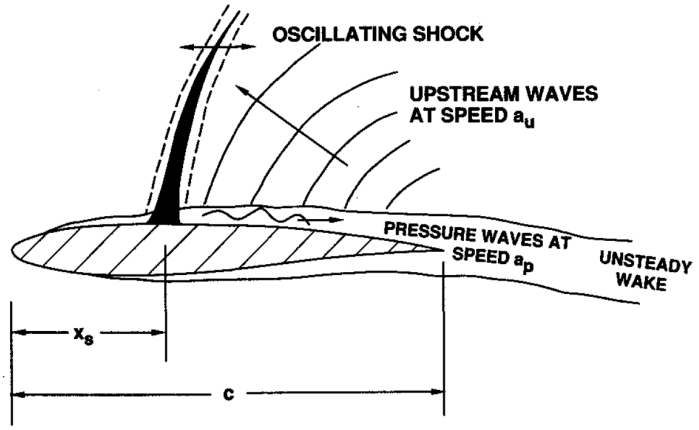

Figure 2.6: Lee's model for buffet of the second kind (adapted from Lee [8]).

Lee [8] developed a model that predicts the frequency of shock oscillations specific to Type A oscillations. This model attributes the periodic movements of the shock to a feedback mechanism involving the propagation of acoustic pressure waves that interact with the shock. This concept is visually shown in Figure 2.6. The periodic shock oscillations are sustained by a continuous feedback loop: The acoustic waves travel upstream and reach the shock, where energy exchange occurs. Efforts to enhance Lee's model have been undertaken by several researchers, including Jacquin et al. [26]. They suggested a modification where the pressure waves do not only travel towards the shock on the suction side; but also upstream on the pressure side, curving around the leading edge, and reach the shock. This enables interaction with the shock from both sides.

Furthermore, Figure 2.7 shows the buffet boundary as described in the work of Lee [27]. In the subsonic regime, the boundary is defined by the max lift vs. Mach number curve. As the flow speed increases, the shock will move towards the trailing edge until the flow is fully supersonic and shock-induced separation disappears. It can also be observed from Figure 2.7 that within the transonic regime, a relatively large area of operation exists for lower transonic free stream Mach numbers where onset of buffet is not present. As the Mach number increases, this area decreases rapidly towards the "elbow" of the buffet boundary. Lee and Ohman [28] have shown that large force fluctuations are present for the BGK No. 1 (supercritical) airfoil at $M_\infty = 0.733$. These fluctuations reach up to $C'_N = 0.05$ for the normal force coefficient.

Buffet phenomena for bodies of revolution are predominantly investigated in relation to helicopter rotors. A notable area of focus is buffet control, as exemplified by the research of Hanagud et al. [29]. They presented a design method for active structural buffet control aimed at reducing the amplitude of oscillatory loads. Additionally, there has been significant research into mitigating buffet through the SBLI control using methods like bumps or morphing layers. A notable example is the study by Shi et al. [30], which indicated that an adaptive bump created by a morphing layer can effectively attenuate a strong normal shock. This is achieved by forming a λ-shaped shock structure over the layer. However, these methods are not suitable for wind turbine blades, as they negatively affect performance at wind speeds below the rated power.

It's also important to note the distinct behavior of buffet under three-dimensional effects. Recent experimental findings by D'Aguanno et al. [31] reveal a notable reduction in load fluctuations for finite wings in comparison to full-span airfoils. This suggests that in the case of buffet occurrences in the

URANS simulations conducted in this study, the acquired load oscillations that would likely be an overestimate compared to the fluctuations experienced by a rotor.

In conclusion, the onset of transonic buffet could become relevant for wind turbine blades that will operate in the transonic regime. Type 1 buffeting is limited to the very specific case of a biconvex airfoil at zero angle of attack. Type 2 buffeting is studied mostly in the context of supercritical airfoil applications, where shock waves terminate on the suction side. The NACA 63(4)-421 airfoil considered in this study could experience shocked flow on both suction and pressure side when it operates in the critical regime. In addition, it must be considered that a thick airfoil could lead to different transonic buffet behavior compared to supercritical airfoils.

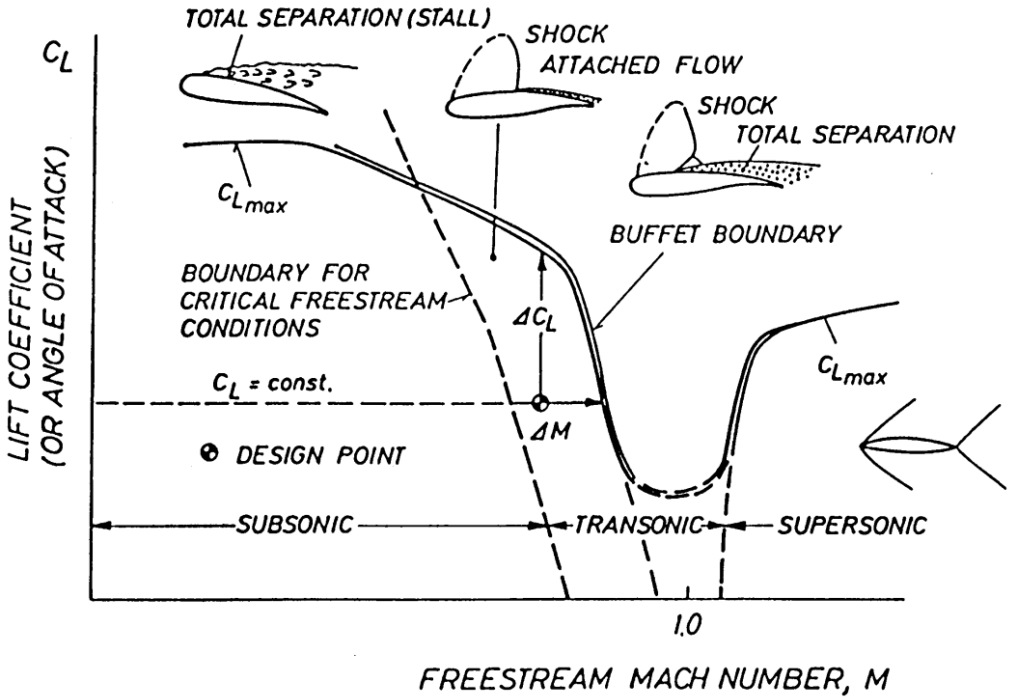

Figure 2.7: Transonic Buffet Boundary and the effect on the lift coefficient C_l (adapted from Lee [27]).

3

Horizontal-Axis Wind Turbines

Horizontal-axis wind turbines (HAWTs) are a type of turbine where the main rotor shaft is aligned horizontally with respect to the ground surface. This design is the predominant type utilized within the wind energy industry. Although the company's rotor design is not a HAWT in the classical sense, it rather aims to be an improvement to the conventional concept, and the effects of compressible flow will have similarities. Therefore, this section reviews the literature of compressible flow effects for HAWTs.

Veers et al. [1] published an overview of the grand challenges for the future of wind energy. It is stated that the cost of electrical energy from wind must continue to decrease over the following decades to remain economically attractive. To achieve this, manufacturers resort to increasing the hub height, power rating and rotor diameter. The fundamental equation of wind turbine energy production (3.1) helps to explain this trend. Here, P represents the power production, ρ the fluid density, C_P the turbine's power coefficient, A the swept rotor area, and U_0 the incoming free stream velocity.

$$P = \frac{1}{2}\,\rho\, C_P\, A\, U_0^3, \tag{3.1}$$

Due to the earth's atmospheric boundary layer, higher flow velocities are found at higher altitude. Increasing the hub height allows for operation in the higher-quality regime (i.e. higher wind speed U_0), thus increasing power production. Furthermore, the transition towards variable-speed wind turbines – currently dominating in market share compared to fixed speed turbines [32] — allows operation at peak C_P for a larger range of wind speeds. Variable speed turbines are not constrained to operate at fixed rotational speed to assure the generator matches the grid frequency (~ 50 Hz). Instead, they implement power electronics to adjust the generator speed independently of the wind speed. The final incentive towards energy-cost reduction is increasing the swept rotor area A, leading to wind turbines being designed with increasingly longer blades, while aiming for high tip speeds [5]. With increasing tip speeds, compressible flow theory might become significant for understanding their aerodynamic behavior. While in the past, the assumption of incompressible flow was considered valid, Yan and Archer [2] state that this assumption is questionable for modern wind turbines. Tip speeds for these turbines can reach Mach numbers exceeding 0.3 for nominal operating conditions, and even higher for wind speeds near the cut-off speed. In their research, they evaluated the NREL 5-MW reference turbine [33] (rotor diameter $D = 128$ m), since its blade section data is well documented. Firstly, they conducted a BEM simulation. To account for the compressibility effects, they used the Prandtl-Glauert correction [13] (see section 2.2 for its derivation). The simulation was performed for a uniform incoming wind speeds of $U_0 = \{5, 10, 15, 20\}$ m/s and a tip speed ratio (TSR) range from 0.25 to 16 with an incrementation of 0.25. TSR, often indicated by λ, is a dimensionless quantity given by Equation (3.2), where Ω represents the turbine's rate of rotation in radians per second, R the rotor diameter and U_0 the incoming wind speed.

$$\lambda = \frac{\Omega R}{U_0}, \tag{3.2}$$

The results show that for free stream velocities lower than ~ 15 m/s and TSR lower than ~ 12, no significant effect on power production due to compressibility is found. However, for free stream velocities

higher than ~ 15 ms^{-1} and TSR greater than ~ 12, the compressibility effects become significant and power losses can reach up to 50% (see figure 3.2a for a visual representation). It should be noted that large HAWTs mostly operate at a TSR of approximately 8. From these findings, they concluded that it is appropriate to use the incompressible aerodynamic coefficients to assess rotor power and torque.

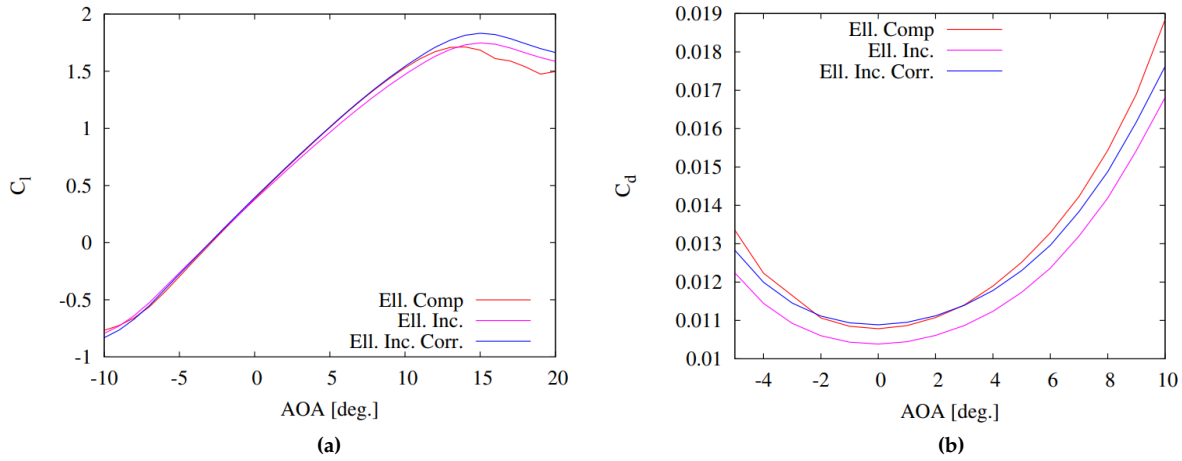

Figure 3.1: Comparison of **(a)** Lift and **(b)** Drag Polars for EllipSys2D (Ell.) CFD Compressible, Incompressible & Corrected Incompressible Solution (adapted from Sørensen et al. [5]).

Sørensen et al. [5] investigated the characteristics for even larger wind turbines (20 MW+, $D > 200$ m) using 2D CFD for the DU91-W2-250 airfoil. Both compressible and incompressible RANS solvers were used to assess the effects. They calculated the lift and drag polars at $r/R = 0.97$ for the AVATAR rotor [34] with a corresponding rotor tip Mach number of $M_\infty = 0.3$ and chord-based Reynolds number in the order of 14 million. The results from the incompressible solver, the compressible solver and the corrected (Prandtl-Glauert) incompressible solver are reported. It is concluded that the correction on the incompressible solution, accurately predicts the lift and drag of the compressible solution in the linear region (refer Figure 3.1). The corrections can be applied as a post-processing step provided that the flow is attached, viscous effects are limited, and Mach numbers do not exceed 0.3. Given that two separate solvers were employed; one for incompressible simulations and another for compressible simulations, questions arise regarding the fairness of this comparison. A more compelling methodology would involve the utilization of a single compressible solver, accompanied by setting a very low free stream Mach number (e.g., $M_\infty = 0.01$) for the incompressible simulations.

Compressibility effects are not limited to the aerodynamic coefficients. Therefore, the second part of the work by Yan and Archer [2] is dedicated to the effects of variable density. They executed Three-dimensional CFD (compressible RANS) simulations, simulating both a single and dual rotor set-up utilizing an actuator line model (ALM). The effects of variable density are assessed by using both an incompressible and compressible framework, and subsequently computing their differences. They use the same aerodynamic coefficients for the incompressible and compressible framework, to isolate the effects of variable density. This is partly in line with their previous findings that for lower TSR and wind speeds, the incompressible coefficients hold. They find that wind speed and turbulent kinetic energy differences between the compressible and incompressible simulations stem from the rotor tip area, but subsequently affect the full wake. For a single turbine in the ABL, the results show that power production is 8% lower for standard operating conditions (TSR~ 8) and 20% lower for a high TSR of ~ 12.

In a more recent publication, Cao et al. [3] question the approach of Yan and Archer [2]. They state that it is inaccurate to apply the same set of tabulated airfoil data for both the compressible and incompressible computations. For their analysis of compressibility effects, the entire blade geometry is modelled on a semi-cylindrical domain. Again, using a compressible and incompressible RANS framework to solve the flow field. In contrast with Yan and Archer [2], the findings show that the torque (hence, the power coefficient C_P) is higher for the compressible solution compared to the incompressible solution. For the case of an incoming wind speed $U_0 = 10.59$ m/s and tip Mach number of 0.28, the

total torque output for the IEA 15MW turbine [35] is 11.07% higher for the compressible case. Figure 3.2b shows that the computed forces are of greater magnitude in the blade tip region.

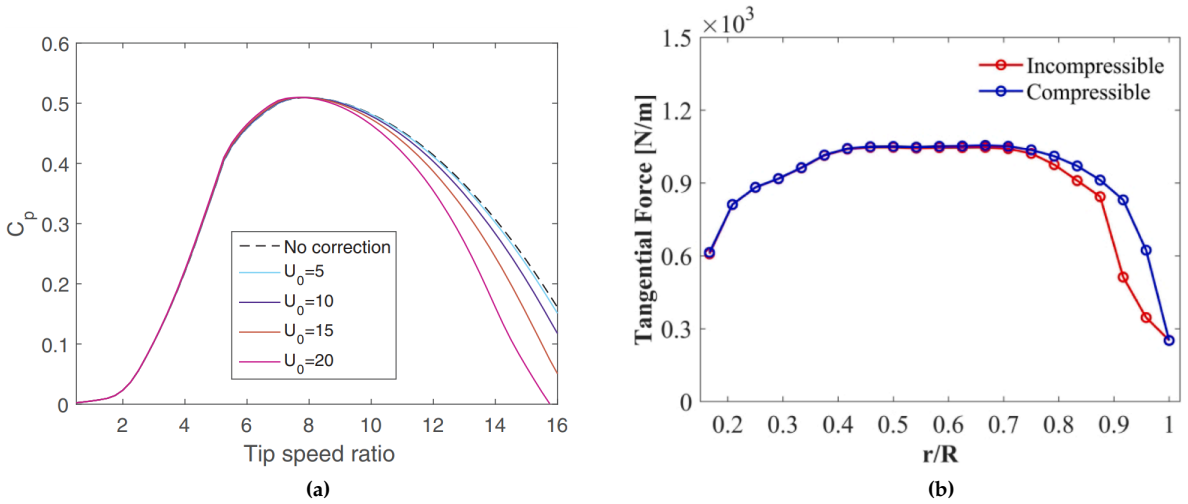

Figure 3.2: Comparison of power/ force results: **(a)** shows the BEM results for NREL 5-MW [33] by Yan and Archer [2] and **(b)** the span-wise tangential force distribution for the compressible & incompressible RANS Solution for IEA 15MW [35] by Cao et al. [3].

Although it is an unexpected observation that the compressibility effects lead to a reduction of power production in one study and an increase in the other, the force diagram from figure 3.3 can help explain from a purely geometrical relation why compressibility could both increase and decrease torque production. In this figure, the Lift and drag force are denoted by L and D respectively. Both quantities can be non-dimensionalized by the following relation:

$$C_l = \frac{F_l}{\frac{1}{2}\rho {U_{rel}}^2 S}; \quad C_d = \frac{F_d}{\frac{1}{2}\rho {U_{rel}}^2 S}, \tag{3.3}$$

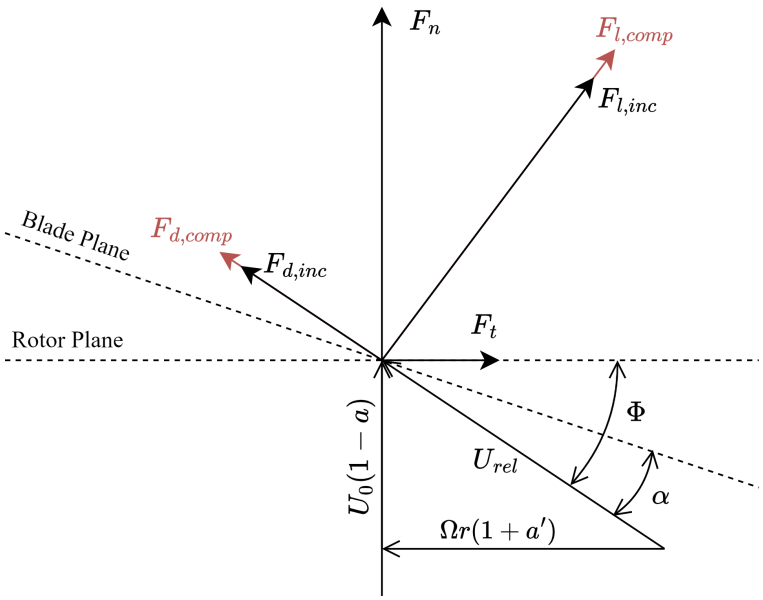

Figure 3.3: Schematic of forces acting on a blade element: U_{rel} represents the incoming velocity by the blade element. $F_{l,comp}$ and $F_{d,comp}$ indicate the increase in lift and drag force from the Prandtl-Glauert correction.

The relation between the lift and drag force with respect to the tangential and normal force is a geometric relation (see figure 3.3). By applying the Prandtl-Glauert correction (2.7) to the lift and drag coefficients, the effects of compressibility can be mapped onto the normal and tangential force coefficients. From Figure 3.3, it can be observed that the compressible solution would always result in a larger tangential force F_{tan} (in the case of positive tangential force) for the same inflow angle. However, the induction values a and a' will vary for a compressible and incompressible BEM simulation, resulting in a different inflow angle Φ.

To study the effects in more detail, the NREL-5MW [33] reference turbine was analyzed using a self-developed BEM code which includes a Prandtl tip-loss correction for a finite number of blades [36] (not to be confused with Prandtl-Glauert compressibility correction). The same airfoil and blade section data is used as for the study by Yan and Archer [2]. The Prandtl-Glauert correction is applied to the lift and drag polars, assuming a constant speed of sound $c = 340$ m/s to calculate the local Mach number.

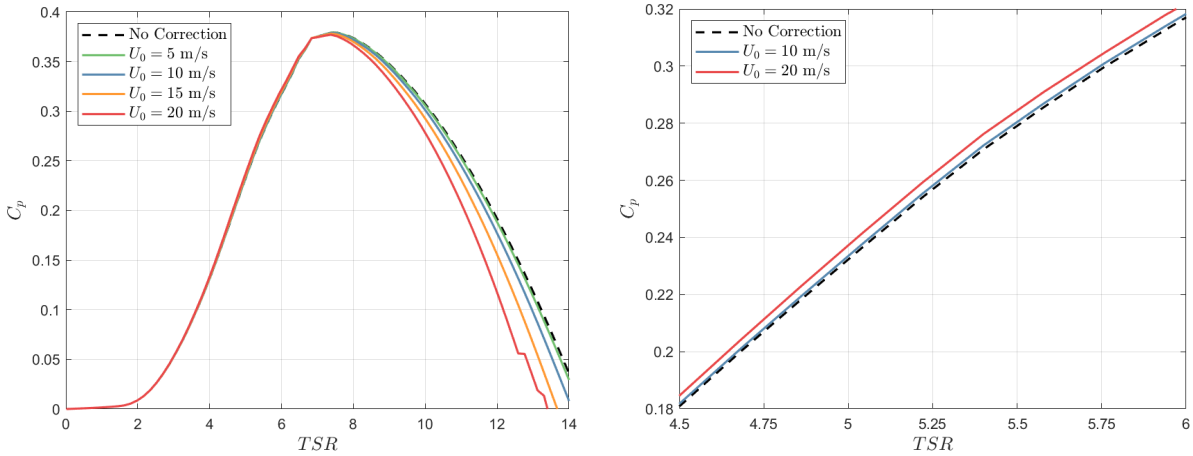

Figure 3.4: BEM results for non-dimensional power coefficient C_p: **(a)** shows the results for the entire TSR range and **(b)** for lower TSR where the compressible solution leads to a higher C_P. $U_0 = 5$ & 15 m/s are omitted here to improve visibility.

Figure 3.4 shows the BEM results for the power coefficient C_P. When the results are compared with the power curve of Yan and Archer [2] in Figure 3.2a, we observe a very similar shaped curve, although its magnitude is lower by $\sim 20\%$. This can have numerous reasons, but for the purpose of qualitatively assessing compressibility effects it is irrelevant. Interesting to note is that, when we focus on the range of TSR lower than peak C_P (Figure 3.4b), the compressibility corrections lead to higher power coefficients C_p. This can also be the case in Figure 3.2a, but it is difficult to observe and not specifically mentioned by Yan and Archer [2]. They only indicate compressibility effects are negligible for this regime.

Cao et al. [3] performed their analysis for a TSR of approximately 9, which is near peak C_P for the IEA 15MW turbine [35], and observed a significant increase in tangential force in the tip region. This does not correspond with the BEM results from Figure 3.2a and 3.4a, and it can be concluded that more research is required to assess the effects accurately.

3.1. Local Supersonic Flow

The studies that have been mentioned thus far [2, 3, 5] consider the effects of compressibility, but the onset of shock waves is out of their scope. As has been discussed in section 2.3, a shock wave will occur once the free stream Mach number M_∞ exceeds critical Mach number M_{crit}.

The first question that arises is whether HAWTs will operate under transonic flow conditions. De Tavernier & von Terzi [4] performed an identification study on the occurrence of local supersonic flow in the blade tip region. They first established a sub- and supersonic regime to assess for which conditions (Mach number M_∞ and angle of attack α) local supersonic flow will occur.

Using the definition of the critical pressure coefficient $C_{p,crit}$ from Equation (2.16), Figure 3.5a can be produced, where the boundary between the sub- and supersonic regime follows from $C_{p,crit}$. Furthermore, Figure 3.5b shows the sub- and supersonic regime for a combination of free stream Mach

number M_∞ and angle of attack α. The boundaries of this graph are dependent on the airfoil geometry and chord-based Reynolds number Re_c. The regimes are calculated for the NACA 63(4)-421 airfoil using xFoil in viscous mode, for a Reynolds number of 2×10^6. The critical pressure coefficient from Equation (2.16) is derived from compressible flow theory. This means that a correction should be applied to obtain the incompressible critical pressure coefficient, since xFoil implements a vortex panel method (hence, incompressible). Three corrections are implemented in Figure 3.5: Prandtl-Glauert, Karman-Tsien and Laitone. More can be read about these corrections in section 2.2.

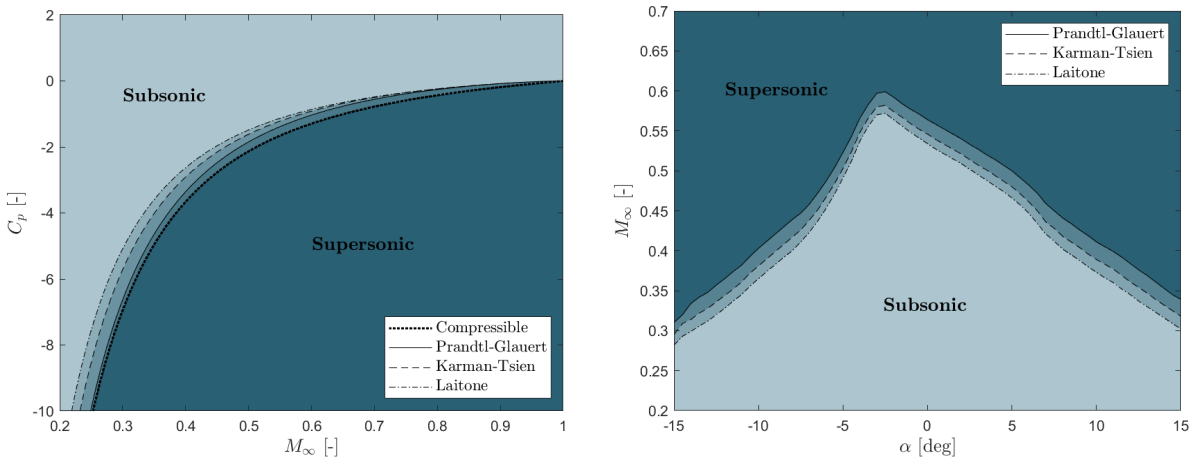

(a) **(b)**

Figure 3.5: Sub- and supersonic regime for NACA63(4)-421: **(a)** M_∞ vs C_p and **(b)** α vs M_∞ for $Re_c = 2.0 \times 10^6$, calculated using xFoil. Lines correspond with corrections to compressible C_p using indicated methods.

After defining a sub- and supersonic regime by the method described above, De Tavernier & von Terzi [4] analyzed the IEA 15MW reference turbine [35] for a turbulent wind profile under different operating conditions. At each discrete time-step, a point was plotted on a α - M_∞ diagram, similar to Figure 3.5b. From this analysis, it has been identified that supersonic flow at the blade tip may occur at high wind speeds. This was found for operational conditions near the cut-out speed, and the inflow turbulence was determined to be the driving factor. They concluded that, especially when keeping in mind the industry trends, the occurrence of local supersonic flow and its effects should be seriously considered in future HAWT design.

The published research regarding the effects of shock-formation on wind turbine blades is very limited. Nevertheless, Wood [6] published a paper on the subject as early as 1997. In this research, he investigated small wind turbines (600W — 5kW), as they typically operate at high TSR. The paper focuses primarily on whether the onset of shock-stall can function as an over-speed protection mechanism in the case of an unloaded rotor; where angular velocity maximizes. When the critical Mach number M_{crit} is surpassed, the drag coefficient C_d starts to increase rapidly, as shown in Figure 2.4. It is hypothesized that this effect can act as a braking mechanism. To assess the effects, he conducted a BEM analysis, using the polar data of the NACA 0012 airfoil for various Mach numbers M_∞. It was concluded that the drag divergence; i.e., the velocity for which the drag starts to increase rapidly, occurs to slowly w.r.t. the decrease in runaway TSR for increasing incoming wind speeds U_0. It should be noted, however, that for thicker airfoils (like the NACA 63(4)-421) that have a lower drag divergence Mach number M_{DD}, shock-stall might be a viable overspeed protection strategy.

A more recent publication by Hossain et al. [37] investigated shock wave propagation on the S809 airfoil (from NREL Phase IV reference turbine). They conducted 2-dimensional RANS simulations for a set Mach number of $M_\infty = 0.8$ and a varying angle of attack α. No major conclusions are drawn in their work, but they have shown that the shock position moves towards the trailing edge on the top surface, and towards the leading edge on the bottom surface, when the angle of attack is increased from $\alpha = 0°$ towards $9°$. Furthermore, they observed that the drag increases gradually when the angle of attack is increased, but around $\alpha = 8°$ the drag suddenly increases very rapidly, due to shock-induced separation.

Part II

2D CFD

4

CFD: Methodology

This chapter explains the mathematical model we use to describe the problem, and subsequently, how this problem will be solved numerically. Figure 4.1 shows a diagram of various available flow models. As we progress downward in the diagram, more assumptions are introduced, constraining the model's ability to capture certain characteristics of the flow. The selection of a model, inherently involves a trade-off between the complexity it can capture and computational costs. Given the objective to model the onset of shock-waves and the intricate characteristics of shock boundary layer interactions, such as shock-stall and transonic buffet, we are bound to use the Navier-Stokes models.

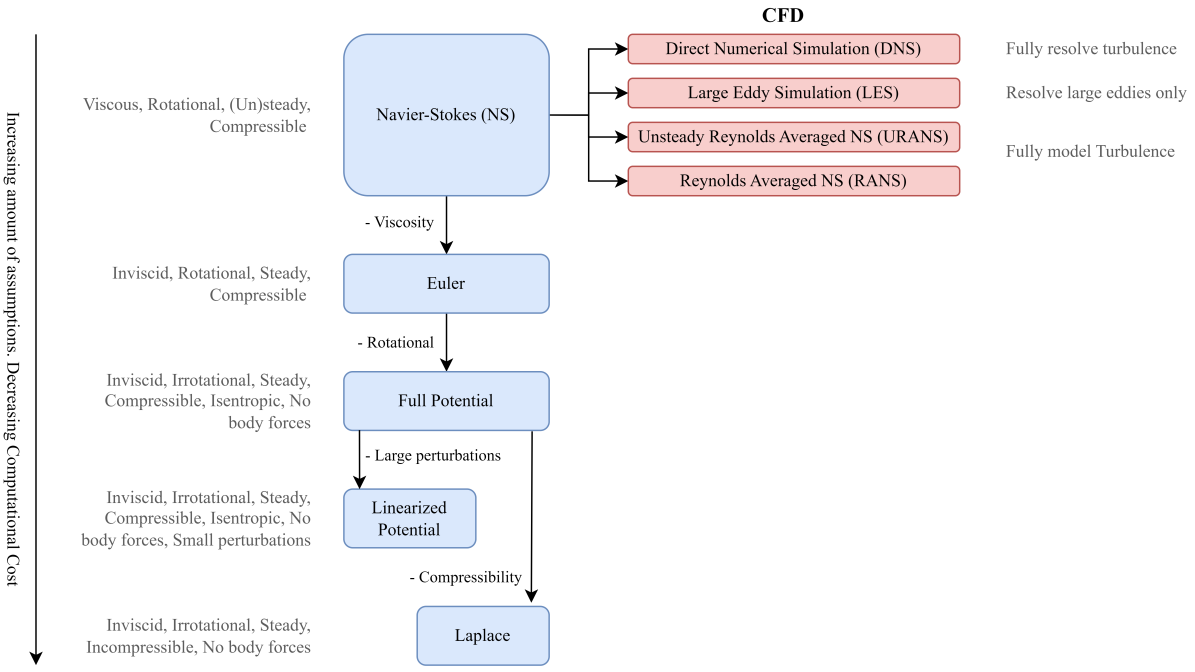

Figure 4.1: Diagram of flow models, based on the work of Jameson [38] and Peerlings [39].

The highest fidelity model, Direct Numerical Simulation (DNS), completely resolves all turbulent length scales. This makes DNS very computationally expensive, which arises from the necessity of having a sufficiently large domain to capture the largest eddies, while requiring an exceptionally fine grid to resolve the smallest eddies. According to Spalart [40], DNS might be ready for industrial applications (like full aircraft, or turbines) in 2080, assuming the rule of thumb that computer power increases by a factor of 5 every 5 years.

Large eddy simulation (LES), as the name suggests, resolves the largest and models the smaller eddies. The largest eddies carry the most mass, momentum, and energy. Hence, LES can provide a very

accurate prediction of the flow field, while the computational costs are reduced significantly compared to DNS. Nevertheless, for high Reynolds number flows ($Re > 10^6$), such as the airfoil analysis in this research, the computational cost for LES remains relatively high [41].

The computational cost can be lowered further when the RANS equations are used. The steady RANS equations are established by time-averaging the Navier-Stokes equations in mean and fluctuating components, referred to as the *Reynolds Decomposition*. The mean part of this decomposed problem can subsequently be solved numerically. RANS assumes that the flow remains steady, neglecting the unsteady or time-dependent behaviour of turbulence. This assumption limits the ability of RANS to capture time-varying phenomena, such as transonic buffet, explained in section 2.3. Unsteady Reynolds-Averaged Navier-Stokes (URANS) addresses this limitation by the implementation of ensemble averaging instead of time averaging. In contrast to inherently unsteady turbulent flows, the periodic motion of the shock occurs at relatively low frequencies. Consequently, there exists a substantial gap between the high frequencies associated with attached-shear-layer turbulence and buffet. This makes the URANS approach appropriate for predicting transonic buffet on airfoils. The assumption underlying this approach is that the unsteady mean flow is resolved, and the near-wall turbulence is effectively modelled by the same turbulence model demonstrated to be applicable for steady transonic flow with shock-induced separation [42].

Since the URANS approach will be able to capture all flow characteristics of interest, including shock capturing and transonic buffet, it has been selected as the computational framework for this work. In Sections 4.1 – 4.5, the full setup of the URANS simulations will be described. To conclude this chapter, the design space will be given in Section 4.6. Here, the set of flow conditions (M_∞, Re_c and α) for the simulations are given.

4.1. Favre-Averaged Equations

The Navier-Stokes equations for a compressible, viscous, heat-conducting, perfect gas can be written in the following form, as described by Cebeci and Smith [43].

Continuity:

$$\frac{\partial \rho}{\partial t} + \frac{\partial}{\partial x_j}\left(\rho u_j\right) = 0, \tag{4.1}$$

Momentum:

$$\frac{\partial}{\partial t}\left(\rho u_i\right) + \frac{\partial}{\partial x_j}\left(\rho u_i u_j\right) = -\frac{\partial p}{\partial x_i} + \frac{\partial \tau_{ij}}{\partial x_j}, \tag{4.2}$$

Energy:

$$\frac{\partial}{\partial t}(\rho H) + \frac{\partial}{\partial x_j}\left(\rho u_j H\right) = \frac{\partial p}{\partial t} + \frac{\partial}{\partial x_j}\left(u_i \tau_{ij} - q_j\right), \tag{4.3}$$

Here, the stress tensor is denoted by τ_{ij}, velocity in the i-th component by u_i, thermodynamic pressure by p, density by ρ, total enthalpy by H and the heat flux vector by q_j.

Even for the simplest incompressible problems, it is a serious challenge to solve the equations for turbulent flow, because of the non-linear terms. Therefore, averaging procedures are implemented in RANS simulations. The procedure involves splitting the instantaneous quantities into their mean and fluctuating components. This can be done for any quantity q, and is referred to as *Reynolds averaging*.

$$q_i\left(x_i, t\right) = \bar{q}_i\left(x_i\right) + q_i''\left(x_i, t\right), \tag{4.4}$$

Here, $\bar{q}_i\left(x_i\right)$ denotes the time-averaged quantity, and $q_i''\left(x_i, t\right)$ the fluctuations from the temporal mean. The fluctuating component becomes zero when time-averaged, following the definition of the time average.

$$\bar{q} \equiv \lim_{T\to\infty} \frac{1}{T} \int_t^{t+T} q dt, \tag{4.5}$$

When averaging over the full time domain, all unsteady phenomena disappear in the solution. For this reason, the ensemble average is taken for URANS simulations, given by Equation (4.6).

$$\hat{q} \equiv \lim_{N\to\infty} \frac{1}{N} \sum_{n=1}^{N} q_n, \tag{4.6}$$

Here, N denotes the rank of the ensemble and q is dependent on position and time.

For a compressible flow, traditional Reynolds averaging can be used, but the governing equations have a simpler form when a mass-weighted average is taken instead. This is also referred to as *Favre-averaging* [44]. We can define a mass-weighted mean velocity as,

$$\tilde{u_i} = \frac{\overline{\rho u_i}}{\bar{\rho}}, \tag{4.7}$$

where the tilde denotes the mass-weighted average. We may then write the velocity vector as a sum of the mass-weighted average $\tilde{u}_i\left(x_i\right)$, and superimposed velocity fluctuation $u_i'\left(x_i, t\right)$.

$$u_i\left(x_i, t\right) = \tilde{u}_i\left(x_i\right) + u_i'\left(x_i, t\right), \tag{4.8}$$

Multiplying Equation (4.8) by the expression for $\rho(x_i, t)$ as given by Equation (4.4) yields:

$$\rho u_i = \left(\bar{\rho} + \rho''\right)\left(\tilde{u}_i + u_i'\right) = \bar{\rho}\tilde{u}_i + \rho''\tilde{u}_i + \rho'' {u_i}' + \bar{\rho} {u_i}', \tag{4.9}$$

When averaged and the definition of $\rho(x_i, t)$ is applied, we get the following:

$$\overline{\rho u_i} = \bar{\rho}\tilde{u}_i + \overline{\rho {u_i}'}, \tag{4.10}$$

Now, recall the definition of $u_i(x_i, t)$ from Equation (4.7). We finally obtain that:

$$\overline{\rho {u_i}'} = 0, \tag{4.11}$$

Note the difference between the two averaging methods. For Reynolds averaging, $\overline{u_i''} = 0$ and $\overline{\rho u_i''} \neq 0$; while for Favre averaging, $\overline{u_i'} \neq 0$ and $\overline{\rho u_i'} = 0$.

Now that the averaging procedures are known, we can apply them to the Navier-Stokes equations, starting with Continuity from Equation (4.1). The definition for $\rho(x_i, t)$ according to Equation (4.4) and $u_i(x_i, t)$ from (4.8) are substituted into Equation (4.1).

$$\frac{\partial}{\partial t}\left(\bar{\rho} + \rho''\right) + \frac{\partial}{\partial x_j}\left(\rho\tilde{u}_j + \rho u_j'\right) = 0, \tag{4.12}$$

Averaging according to Equation 4.6 yields the mean continuity equation for compressible turbulent flow:

$$\boxed{\frac{\partial \bar{\rho}}{\partial t} + \frac{\partial}{\partial x_j}\left(\bar{\rho}\tilde{u}_j\right) = 0\ ,} \tag{4.13}$$

A similar procedure can be applied to the momentum equation, using an additional Reynolds averaged quantity for pressure $p(x_i, t)$, according to Equation (4.4). This yields the following:

$$\boxed{\frac{\partial}{\partial t}\left(\bar{\rho}\tilde{u}_i\right) + \frac{\partial}{\partial x_j}\left(\bar{\rho}\tilde{u}_i\tilde{u}_j\right) = -\frac{\partial \bar{p}}{\partial x_i} + \frac{\partial}{\partial x_j}\left(\bar{\tau}_{ij} - \overline{\rho u_i' u_j'}\right)\ ,} \tag{4.14}$$

And finally, for the Energy equation, we take the Reynolds averaged quantities for density $\rho(x_i, t)$ and pressure $p(x_i, t))$ (Equation (4.4)) and the Favre averaged quantities for velocity $u_i(x_i, t)$, and temperature $T(x_i, t)$. The mass weighted average for the total enthalpy $\tilde{H}$ becomes.

$$\tilde{H} = \tilde{h} + \frac{1}{2}\tilde{u}_i\tilde{u}_i + \frac{1}{2}\frac{\overline{\rho u_i' u_i'}}{\bar{\rho}} \tag{4.15}$$

Substitute into Equation (4.3) and the Favre-averaged Energy equation is obtained.

$$\boxed{\frac{\partial}{\partial t}(\bar{\rho}\tilde{H}) + \frac{\partial}{\partial x_j}\left(\bar{\rho}\tilde{H}\tilde{u}_j\right) = \frac{\partial \bar{p}}{\partial t} + \frac{\partial}{\partial x_j}\left(-\bar{q}_j - \overline{\rho H' u_j'} + \tilde{u}_i\bar{\tau}_{ij}\right)\ ,} \tag{4.16}$$

The above equations for continuity (4.13), momentum (4.14), and energy (4.16) are often referred to as the compressible RANS equations; and sometimes, Favre-Averaged Navier-Stokes equations (FANS).

4.2. Turbulence Model

When comparing the Favre averaged momentum (4.14) and energy (4.16) equations with the NS equations from (4.2) and (4.3), it can be observed that the averaging method has introduced additional non-zero terms. These terms are referred to as the *Reynolds stresses* denoted by τ_{ij}^t,

$$\tau_{ij}^t = -\overline{\rho u_i' u_j'}, \tag{4.17}$$

The Reynolds stresses can be subdivided in normal stress components (4.18a) and shear stresses (4.18b). In total, six terms are introduced by the momentum equation, and they will be non-zero due to interactions between turbulent fluctuations.

$$\tau_{xx}^t = -\overline{\rho u'^2} \qquad \tau_{yy}^t = -\overline{\rho v'^2} \qquad \tau_{zz}^t = -\overline{\rho w'^2}, \tag{4.18a}$$

$$\tau_{xy}^t = \tau_{yx}^t = -\overline{\rho u' v'} \qquad \tau_{xz}^t = \tau_{zx}^t = -\overline{\rho u' w'} \qquad \tau_{yz}^t = \tau_{zy}^t = -\overline{\rho v' w'}, \tag{4.18b}$$

In addition to the Reynolds stresses, averaging introduced the turbulent heat flux vector to the energy equation.

$$q_j^t = \overline{\rho H' u_j'}\,, \tag{4.19}$$

To predict the behaviour of turbulent flows in a RANS framework, the Reynolds stresses and turbulent heat flux vector are modelled by means of a turbulence model. These are often categorized by the number of additional transport equations that need to be solved. Table 4.1 shows the most common turbulence models for RANS according to Versteeg and Malalasekra [45].

No. of transport equations	**Model name**
Zero	Mixing length
One	Spalart-Allmaras
Two	$k-\epsilon$
	$k-\omega$
	Algebraic stress
Seven	Reynolds stress

Table 4.1: Most common turbulence models for RANS [45].

It should be noted that many variations and additional models exist that are not included in table 4.1. Several models can be preliminary excluded for numerous reasons. For example, because they do not predict shock-stall behaviour well, or do not capture transonic shock oscillations. We will review the literature to find the most common turbulence models implemented in transonic and unsteady flow simulations.

Catalano and Amato [46] studied the Spalart-Allmaras, Myong and Kasagi $k-\epsilon$, Wilcox $k-\omega$, Kok TNT and Menter's $k-\omega$ SST turbulence models, and a nonlinear eddy viscosity model, to assess their performance in simulating transonic flow characteristics. Two of the three cases they studied included transonic flow with a strong SBLI, inducing boundary layer separation. All models listed above were able to were able to predict the shock induced separation. The standard Wilcox $k-\omega$ model performed worst in predicting the velocity profile because it could not capture the shock location accurately. All other models performed good and lied in a narrow band, with Menter's $k-\omega$ model providing the closest match with the experimental results. They concluded that Menter's $k-\omega$ model provided the best results for all three cases, while also having he the highest numerical stiffness.

In a joint publication by Smith et al. [47], five researchers independently evaluated the SC1095 airfoil rotor airfoil for high transonic Mach numbers using CFD. Most researchers implemented a Spalart-Allmaras turbulence model, and one used Baldwin-Lomax. For comparison, some simulations were also executed using Menter's $k-\omega$ STT. It was concluded that Spalart-Allmaras and Menter's $k-\omega$ STT result in similar behaviour in the region of linear aerodynamics. For the transonic & shock-stall region, the models show some variations. However, it was not possible to draw major conclusions because the data fell within the scatter of experimental data. Furthermore, the Baldwin-Lomax model did not perform well and is not recommended.

Furthermore, transonic shock buffeting and its sensitivity to turbulence model selection should be considered. It has been mentioned already in section 2.3 that Gianellis et al. [22] published a review on the subject. In this work, it has been pointed out that there have been successes regarding transonic shock buffet simulations using a URANS framework. Nevertheless, the selected turbulence model has great influence on the accuracy of the results. Concalves and Houdeville [48] studied shock oscillations on the RA16SC1 airfoil through RANS simulations implementing various turbulence models. Figure 4.2 shows the root means square non-dimensional pressure fluctuations for the turbulence models, that did not lead to a steady solution. It can be observed that Spalart-Allmaras leads to an under-prediction of the fluctuations, while $k-\omega$ Kok model overpredicts. Menter's $k-\omega$ SST model again provides the closest match to the experimental results. A similar study has been conducted by Tahani et al. [49]. They found that Menter's SST $k-\omega$ model showed good results in predicting SBLI separation, but near the buffet boundary, the accuracy of the results was less convincing.

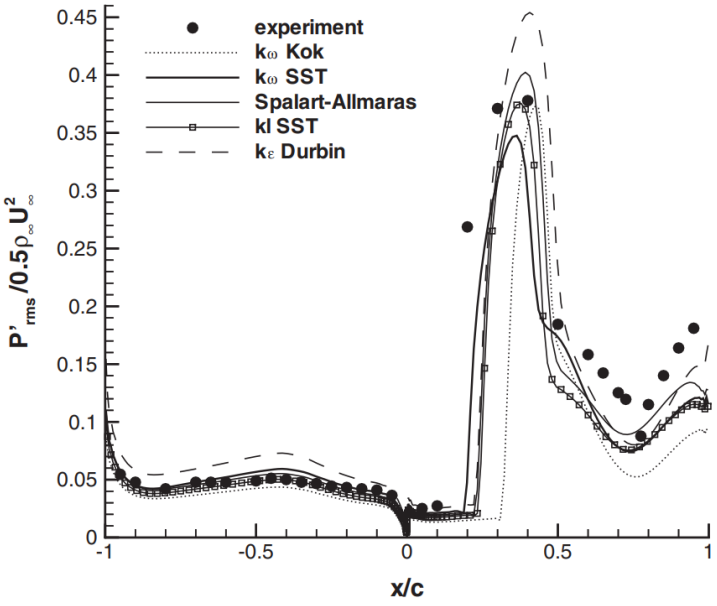

Figure 4.2: RMS pressure fluctuations for the RA16SC1 airfoil at $M_\infty = 0.732$, $Re_c = 4.2 \times 10^6$ and $\alpha = 4°$ (adapted from Concalves and Houdeville [48]).

4.2.1. Model Selection

For this research, not all available turbulence models will be considered. For most models, like Baldwin-Lomax and $k-\epsilon$ models, it has become clear from literature that they will not capture all the flow characteristics of interest. It has been decided to include two turbulence models in this research. They were selected based on the following criteria.

- Availability of validation/verification data.
- Models used in literature for a common application.
- Implementation in OpenFOAM [50] library.
- Ability to reproduce transonic buffeting behaviour.

The selected models - Spalart-Allmaras and Menter's $k-\omega$ SST – are shown in table 4.2, along with their original source and literature in which the models are implemented. Both models are linear eddy viscosity models, which means that the Boussinesq assumption is implemented for the constitutive relation:

$$\tau_{ij}^t = 2\mu_t \left(S_{ij} - \frac{1}{3}\frac{\partial u_k}{\partial x_k}\delta_{ij} \right) - \frac{2}{3}\rho k \delta_{ij} \,, \tag{4.20}$$

Here, μ_t denotes the eddy viscosity, which is obtained by the turbulence model. $S_{i,j}$ represents the strain tensor. Similarly as for the Boussinesq approximation, a relationship between the turbulent heat

flux and turbulent thermal diffusivity can be defined as,

$$q_j{}^t = -\bar{\rho}\alpha_t \frac{\partial \tilde{H}}{\partial x_j}, \quad \text{where}; \quad \bar{\rho}\alpha_t = \frac{\mu_t}{Pr_t} \tag{4.21}$$

where Pr_t denotes the turbulent Prantdl number, which is set to a fixed value of 0.85.

Table 4.2: Turbulence models to be considered.

Turbulence model	Model type	Reference	Implemented by
Spalart-Allmaras	One equation	Spalart and Allmaras [51]	Lien et al. [52] Catalano and Amato [46] Smith et al. [47]
Menter $k-\omega$ SST	Two equation	Menter [53]	Sørensen et al. [5] Hossain et al. [37] Lien et al. [52] Catalano and Amato [46] Tahini et al. [49]

A brief description of the selected models is given according to the work of Versteeg and Malalasekra [45] along with some considerations.

Spalart-Allmaras

The Spalart-Allmaras turbulence model is characterized by a single transport equation for the kinematic eddy viscosity parameter $\tilde{\nu}$. The model offers cost-effective calculations and was introduced by Spalart and Allmaras [51] in 1992. The turbulent eddy viscosity is related to the eddy viscosity parameter $\tilde{\nu}$ by Equation (4.22). f_{v1} represents a wall damping function. For high Reynolds numbers, the function tends to one; hence, the eddy viscosity parameter $\tilde{\nu}$ will becomes equal to the eddy viscosity ν_t.

$$\mu_t = \rho\tilde{\nu} f_{v1}, \tag{4.22}$$

The transport equation for the eddy viscosity parameter $\tilde{v}$ is given by Equation (4.23). Here, f_{v2} and f_w are additional wall damping functions. σ_v, κ, C_{b1}, C_{b2} and C_{w1} are model constants.

$$\frac{\partial(\rho\tilde{\nu})}{\partial t} + \operatorname{div}(\rho\tilde{\nu}\mathbf{U}) = \frac{1}{\sigma_v}\operatorname{div}\left[(\mu+\rho\tilde{\nu})\operatorname{grad}(\tilde{v}) + C_{b2}\rho\frac{\partial\tilde{\nu}}{\partial x_k}\frac{\partial\tilde{\nu}}{\partial x_k}\right] + C_{b1}\rho\tilde{\nu}\tilde{\Omega} - C_{m1}\rho\left(\frac{\tilde{\nu}}{\kappa y}\right)^2 f_w, \tag{4.23}$$

The relationship between the rate of production of $\tilde{\nu}$ and the local mean vorticity is expressed in Equation (4.24a). The mean vorticity Ω is given by (4.24b) and the mean vorticity tensor by (4.24c).

$$\tilde{\Omega} = \Omega + \frac{\tilde{v}}{(\kappa y)^2} f_{v2}, \tag{4.24a}$$

$$\Omega = \sqrt{2\Omega_{ij}\Omega_{ij}}, \tag{4.24b}$$

$$\Omega_{ij} = \frac{1}{2}\left(\frac{\partial U_i}{\partial x_j} - \frac{\partial U_j}{\partial x_i}\right), \tag{4.24c}$$

Although the literature indicates that Menter's $k-\omega$ SST model approximates shock-stall and buffeting characteristics better [46, 48, 49], Spalart-Allmaras showed proper agreement with experimental data. Combined with its computational efficiency has led to the decision to consider the model for this study.

Menter $k-\omega$ SST

According to Menter's [53] observations, the outcomes of the $k-\epsilon$ model exhibit relatively lower sensitivity to the (subjective) prescribed values in the free stream. However, when it comes to the boundary layer with adverse pressure gradients, the model's performance near the wall is considered unsatisfactory. Therefore, he proposed a hybrid model, where the standard $k-\epsilon$ by Launder and

Spalding [54] is transferred to Wilcox' $k-\omega$ model [55] for the near wall region. Towards the free stream, the standard $k-\epsilon$ model is used.

Equation (4.25) describes the transport equation for the ω. The Reynold's stress computations and the equation for turbulent kinetic energy k are the same as for the Wilcox $k-\omega$ model [55], but the expression for $epsilon$ (from standard $k-\epsilon$ [54]) is transformed to the ω equation using the simple relation $\epsilon = k\omega$, resulting in Equation (4.25).

$$\frac{\partial(\rho\omega)}{\partial t} + \operatorname{div}(\rho\omega\mathbf{U}) = \operatorname{div}\left[\left(\mu + \frac{\mu_t}{\sigma_{\omega,1}}\right)\operatorname{grad}(\omega)\right] + \gamma_2\left(2\rho S_{ij}.S_{ij} - \frac{2}{3}\rho\omega\frac{\partial U_i}{\partial x_j}\delta_{ij}\right) - \beta_2\rho\omega^2 + 2\frac{\rho}{\sigma_{\omega,2}\omega}\frac{\partial k}{\partial x_k}\frac{\partial \omega}{\partial x_k}, \tag{4.25}$$

This leads to an extra source term (the last term in Equation (4.25)), which is referred to as the *cross-diffusion* term. Ten years after Menter first introduced the equations, Menter et al. [56] reviewed the model, since it had been used extensively by the industry. They derived the revised model constants, which are shown below (4.26).

$$\sigma_k = 1.0, \quad \sigma_{\omega,1} = 2.0, \quad \sigma_{\omega,2} = 1.17, \quad \gamma_2 = 0.44, \quad \beta_2 = 0.083, \quad \beta^* = 0.09, \tag{4.26}$$

From the reviewed literature, Menter's $k-\omega$ SST model has proven to be (one of the) best performing models for numerous applications, including high-speed stall behaviour [46] and transonic buffeting [48]. It performs better for these phenomena compared to standard $k-\epsilon$ [54], Wilcox $k-\omega$ [55] and Spalart-Allmaras [51] making it the most logical choice to include in this thesis research.

4.3. Non-Dimensional Equations

Non-dimensional variables facilitate the comparison of results from various experiments and simulations. This is particularly useful for the non-dimensional coefficients we're interested in, such as the lift coefficient C_l and drag coefficient C_d. Furthermore, employing the non-dimensional system results in a better numerical accuracy, as all variables, once non-dimensionalized, share the same order of magnitude, assuming appropriate reference values.

OpenFOAM, in its default configuration, utilizes a dimensional framework. Nevertheless, it is possible to conduct non-dimensional simulations by manipulating the flow variables. Reference quantities should be defined to achieve this. The selection of these reference quantities is arbitrary, and for this particular work, we establish reference quantities for the thermodynamic variables, viscosity and thermal conductivity (which originates from writing out the energy equation fully). The dimensional quantities will be denoted with an apex $*$.

$$\rho = \frac{\rho^*}{\rho^*_\infty}, \quad p = \frac{p^*}{p^*_\infty}, \quad T = \frac{T^*}{T^*_\infty}, \quad \mu = \frac{\mu^*}{\mu^*_\infty}, \quad k = \frac{k^*}{k^*_\infty}, \tag{4.27}$$

For the flow velocity vector and energy per unit mass, we use a definition of the speed of sound as a reference quantity.

$$u_i = \frac{u^*_i}{\sqrt{p^*_\infty/\rho^*_\infty}}, \qquad E = \frac{E^*}{p^*_\infty/\rho^*_\infty}, \tag{4.28}$$

The specific heat ratios can be non-dimensionalized by the definition of the universal gas constant per unit mass for a perfect gas.

$$c_v = \frac{c^*_v}{R^*}, \quad c_p = \frac{c^*_p}{R^*}, \quad \text{where;} \quad R^* = \frac{p^*_\infty}{\rho^*_\infty T^*_\infty}, \tag{4.29}$$

The airfoil chord length c^* is used to define a non-dimensional length scale, while non-dimensional time can be constructed from the chord length and the reference velocity.

$$x_i = \frac{x^*_i}{c^*}, \quad t = \frac{t^*}{c^*}\sqrt{\frac{p^*_\infty}{\rho^*_\infty}}, \tag{4.30}$$

We aim to describe our problem in as few dimensionless groups as possible, so we now consider Buckingham's Π theorem [57], which states that: *'A physical relationship between some dimensional quantity and several dimensional governing parameters can be expressed as a relationship between a dimensionless parameter and several dimensionless products of the governing parameters. The number of dimensionless products is equal to the total number of governing parameters less the number of governing parameters with independent dimensions'*.

In total, we have $N_T = 15$ dimensional parameters arise from the governing Navier-Stokes equations, the equation of state, and Sutherland's law [58]. Furthermore there are $N_F = 4$ fundamental dimensions, namely time, length, mass, and temperature. Which would mean that the problem could be expressed with 11 independent non-dimensional groups. Luckily, we know the relations between certain quantities, such as the equation of state:

$$p^* = \rho^* R^* T^* \tag{4.31}$$

The viscosity will be coupled to temperature according to Sutherland's viscosity law,

$$\mu^* = \frac{A_s \sqrt{T^*}}{1 + T_s/T^*}\,, \tag{4.32}$$

where $T_s = 110.4$ K is the Sutherland temperature. In OpenFoam, A_s, needs to be specified:

$$A_s = \mu^*_\infty \left(1 + T_s/T_{ref}\right) / \sqrt{T^*_\infty} \tag{4.33}$$

For the heat transfer coefficient k^* and the specific heat ratios, we have the following relations:

$$k^* = \frac{\mu^* c^*_p}{\mathrm{Pr}}\,, \quad c^*_p = \frac{R^* \gamma}{\gamma - 1}\,, \quad c^*_v = \frac{R^*}{\gamma - 1}\,, \tag{4.34}$$

Here, the Prandtl number Pr is set to be equation to 0.72 for all simulations. Finally, for the energy per unit mass and specific energy, we have:

$$E^* = e^* + \frac{1}{2} u^{*2}\,, \quad e^* = c^*_v T^* \tag{4.35}$$

With the equations given above, the set of non-dimensional groups needed to characterize the problem reduces to just four. While not uniquely determined, opting for the most commonly used dimensionless quantities is an apparent and practical choice for describing flow problems. These four non-dimensional groups are:

$$\text{Chord Based Reynolds Number:} \quad Re_c = \frac{\rho^*_\infty u^*_\infty c^*}{\mu^*_\infty} \tag{4.36}$$

$$\text{Free Stream Mach Number:} \quad M_\infty = \frac{u^*_\infty}{\sqrt{\gamma p^*_\infty / \rho^*_\infty}} \tag{4.37}$$

$$\text{Specific Heat Ratio:} \quad \gamma = \frac{c^*_p}{c^*_v} \tag{4.38}$$

$$\text{Prandtl Number:} \quad Pr = \frac{\mu^* c^*_p}{k^*} \tag{4.39}$$

In theory, the reference quantities can be given any value. It is common practice to set $p^* = \rho^* = T^* = R^* = c^* = 1$. Furthermore, γ is set to be equal to 1.4, corresponding to a predominantly ideal diatomic gas (air). The Prandtl number Pr is set to a fixed value of 0.72. The free stream velocity in x and y-direction, can now be determined as,

$$u_\infty = M_\infty \sqrt{\gamma p^*_\infty / \rho^*_\infty} \cos(\alpha) = M_\infty \sqrt{\gamma} \cos(\alpha)\,, \tag{4.40}$$

$$v_\infty = M_\infty \sqrt{\gamma p^*_\infty / \rho^*_\infty} \sin(\alpha) = M_\infty \sqrt{\gamma} \sin(\alpha)\,, \tag{4.41}$$

And the free stream viscosity μ_∞ can be derived from the Reynolds number,

$$\mu_\infty = \frac{\rho^*_\infty u^*_\infty c^*}{Re_c} = \frac{M_\infty \sqrt{\gamma}}{Re_c} \tag{4.42}$$

4.4. Finite Volume Solver

The previous sections have provided the model; i.e., the governing equations, that we aim to solve. In this section, solving these equations using a numerical algorithm will be examined. Although numerous discretization methods exits, it is common practice to solve the URANS equations using the Finite Volume Method (FVM), as it provides a natural framework for effectively managing conservation laws. This makes FVM particularly well-suited for problems related to fluid flow. Additionally, FVM facilitates the straightforward treatment of intricate geometries and irregular meshes, as the method inherently deals with control volumes that can have arbitrary shapes.

The governing equations are typically written in the integral form, which expresses the conservation of mass, momentum, energy, or other quantities within each control volume. The method involves calculating the fluxes of the conserved quantities across the faces or boundaries of each cell. The fluxes represent the flow of the conserved quantities between adjacent cells and are computed using various numerical approximations, such as interpolation or gradient schemes. By applying the conservation principle to each control volume, a set of discrete equations is obtained. These equations relate the changes in the conserved quantities inside the control volumes to the fluxes across the cell boundaries.

In Section 4.1, we examined the averaging procedures of the Navier-Stokes equations in their differential form. As mentioned, for FVM it is common practise to express the equations in an integral formalism. Equation (4.43) and (4.44) show the URANS equations for a compressible ideal gas integrated over an arbitrary volume V with a vector notation.

$$\frac{\mathrm{d}}{\mathrm{d}t}\int_V \mathbf{W}\mathrm{d}V = -\int_V \left(\mathbf{F}^e - \mathbf{F}^v\right)\,\mathrm{d}V, \tag{4.43}$$

$$\mathbf{W} = \begin{bmatrix} \rho \\ \rho\mathbf{u} \\ \rho E \end{bmatrix}, \quad \mathbf{F}^e = \begin{bmatrix} \rho\mathbf{u} \\ \rho\mathbf{u}\mathbf{u} + pI \\ \rho\mathbf{u}H \end{bmatrix}, \quad \mathbf{F}^v = \begin{bmatrix} 0 \\ \sigma \\ \sigma\mathbf{u} - \mathbf{q}, \end{bmatrix}, \tag{4.44}$$

In this formalism, $\mathbf{W}$ represents the vector of conservative variables, $\mathbf{F}^e$ the Eulerian fluxes and $\mathbf{F}^v$ the viscous fluxes. The total energy per unit mass is denoted by $E = e + u^2/2$, the identity matrix by I, and σ represents the viscous-turbulent stress tensor. FVM relies on the spatial and temporal discretization of the governing equations, so the conservation quantities between adjacent cells can be computed. Spatial discretization is performed by integrating over the vector of conservative variables W taking,

$$\hat{\mathbf{W}}_i(t) = \frac{1}{|V_i|}\iiint_{V_i} \mathbf{W}(\mathbf{x}, t)\,\mathrm{d}V, \tag{4.45}$$

where V_i is the volume of the i-th mesh cell. For FVM, the volume integral on the right-hand side of Equation (4.43) can be converted into a surface integral over ∂V_i by Gauss's theorem. For a polyhedron with arbitrary m faces, this surface integral can be approximated by summing over the faces. For Figure 4.3, this will result in the following approximation:

$$\begin{gathered} \iiint_{V_i} \mathbf{F}(\mathbf{W})\,\mathrm{d}V = \iint_{\partial V_i} \mathbf{F}(\mathbf{W})\cdot n_i\,\mathrm{d}\boldsymbol{S} \approx \sum_f \hat{\mathbf{F}}\left(\mathbf{W}_f\right)\cdot \boldsymbol{S}_f, \\ \text{where}; \qquad \mathbf{F}(\mathbf{W}) = \mathbf{F}^e - \mathbf{F}^v, \end{gathered} \tag{4.46}$$

Here, n_i is the outward normal vector for the i-th face, with corresponding surface area S. Substituting Equation (4.45) and a generalized form of (4.46) into (4.43), we arrive at the spatially discretized equation.

$$|V_i|\,\frac{d\hat{\mathbf{W}}}{dt} = -\sum_{j\in N_i}\left(\hat{\mathbf{F}}_j^e - \hat{\mathbf{F}}_j^v\right)S_i = -\mathbf{R}(\hat{\mathbf{W}})_i, \tag{4.47}$$

Here, N_i represents the collection of indices corresponding to neighboring cells, while $\hat{\mathbf{F}}_j$ and $\hat{\mathbf{F}}_j^v$ denote the numerical flux approximations for the Eulerian and viscous fluxes, respectively. S_i denotes the surface area of the i-th cell. How the numerical fluxes are solved depends on the implemented numerical algorithm. Examples can found in the work of Jiang et al. [59] and Modesti and Pirozzoli [60]. In both papers, a newly developed numerical algorithm is described for compressible flows.

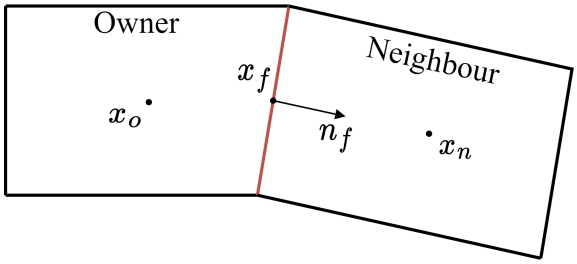

Figure 4.3: Sketch of an arbitrary cell where the numerical fluxes are evaluated.

4.4.1. Solver Selection

For this research, two finite volume solvers have been selected to be incorporated in the validations sequence outlined in Chapter 5. The first is the pressure-based solver *rhoPimpleFoam*, distributed as a baseline solver within OpenFOAM [50]. The second is denisty-based solver *rhoEnergyFoam*, developed by Modesti and Pirozzoli [60]. The selection of these solvers is based on the following considerations:

- *rhoEnergyFoam* yields a more accurate approximation of the aerodynamic coefficients and shock characteristics (see Table 4.3) for a transonic airfoil compared to the baseline central-differencing solver *rhoCentralFoam*.
- Pressure-based solver *rhoPimpleFoam* requires significantly less computational time. In case it transpires from the validation sequence that *rhoPimpleFoam* will predict the flow field and aerodynamic coefficients with sufficient accuracy, the additional computational time could be allocated to generate more data points.

Both numerical algorithms will be explained briefly below, along with their relevant references.

Table 4.3: Lift and drag coefficient of RAE 2822 airfoil at $M_\infty = 0.729$, $Re_c = 6.5 \times 10^6$, $\alpha = 2.31$ [60]

Case	C_l	C_d
rhoEnergyFoam	0.713	0.0133
rhoCentralFoam	0.725	0.0185
Experiment [61]	0.743	0.0127
RANS [62]	0.717	0.0133

rhoPimpleFoam

The PIMPLE algorithm couples the PISO (Pressure Implicit with Splitting of Operator) algorithm, introduced by Issa [63], and SIMPLE (Semi-Implicit Method for Pressure-Linked Equations) algorithm, developed by Caretto et al. [64]. While all these algorithms operate as iterative solvers, PISO and PIMPLE find applications in transient simulations, whereas SIMPLE is typically employed for steady-state cases. For a complete derivation and explanation of both the PISO and SIMPLE algorithms, the reader is referred to the work of Versteeg and Malalasekra [65]. In essence, the PIMPLE algorithm applies the SIMPLE algorithm at each time step, iterating until convergence or reaching a maximum iteration limit. At each iteration, the pressure corrector is applied, according to the PISO algorithm. A main advantage of PIMPLE compared to PISO, is that it exhibits enhanced stability even when dealing with high Courant numbers.

When the *rhoPimpleFoam* solver is applied in this research, the semi-discretized equations are advanced through time using the forward Euler method.

$$\hat{\mathbf{W}}^{(n+1)} = \hat{\mathbf{W}}^{(n)} + \Delta t \mathbf{R}\left(\hat{\mathbf{W}}^{(n)}\right), \tag{4.48}$$

rhoEnergyFoam

The motivation behind the development of the *rhoEnergyFoam* solver [60] has been the aim to minimize numerical diffusion, i.e. the simulated fluid is characterized by higher diffusivity compared to the physical case. The solver is characterized by an energy preserving numerical flux for the convective

terms of the NS-equations. The solver implements an AUSM scheme described by [66]. Furthermore, the test experiments by Modesti and Pirozzoli [60] have proven the solver to be less sensitive to numerical diffusion compared to the OpenFOAM distributed solvers.

The semi-discretized equations are advanced through time using a low-storage third-order, four-stage Runge-Kutta scheme, given by Equation (4.49). For some simulations, the time-marching method was modified to a three-stage scheme to enhance computational efficiency without impacting the results.

$$\hat{\mathbf{W}}^{(\ell)} = \hat{\mathbf{W}}^{(0)} + \alpha_\ell \Delta t \mathbf{R}\left(\hat{\mathbf{W}}^{(\ell-1)}\right), \quad \ell = 1, \ldots, 4, \tag{4.49}$$

Here, Δt denotes the time-step, $\mathbf{u}^{(0)} = \mathbf{u}^n, \mathbf{u}^{n+1} = \mathbf{u}^{(4)}$, and the values for the constants α_ℓ are: $\alpha_1 = 1/4, \alpha_2 = 1/3, \alpha_3 = 1/2$ and $\alpha_4 = 1$.

4.5. Computational Domain

This section completes the modelling approach for the two-dimensional CFD simulations. In the preceding Sections 4.1 through 4.4, we established the equations to be solved and outlined their discretization and numerical algorithm to solve them. Now, attention will be directed towards how the numerical grid is constructed in Section 4.5.1, while the treatment of the grid boundaries is explained in Section 4.5.2.

4.5.1. Mesh Strategy

Structured meshing strategies for airfoils offer three primary options; H-grids, C-grids and O-grids. H-grids are typically implemented for airfoils with both sharp leading and trailing edges, since a singular point is introduced when the leading edge is curved.

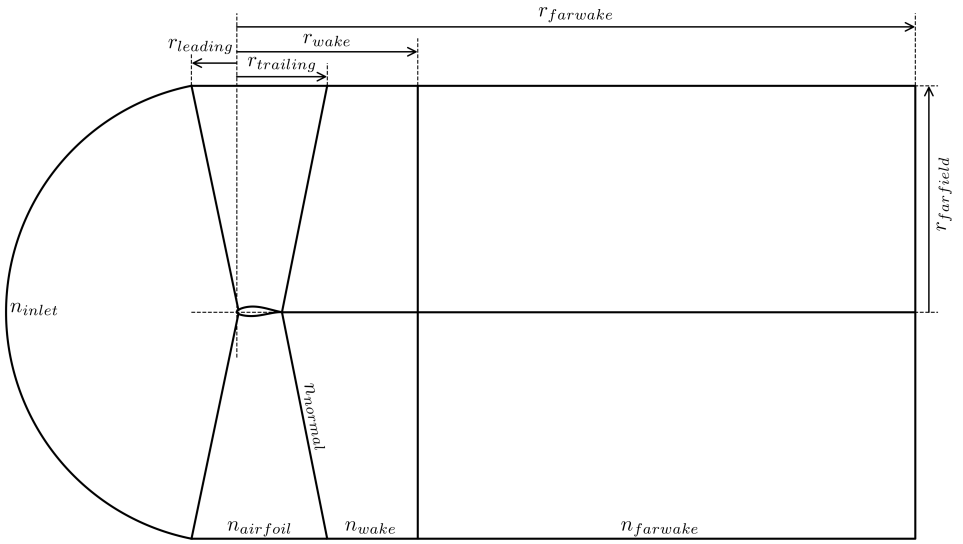

Figure 4.4: Blocking strategy for the C-mesh topology.

A better alternative is the C-grid pattern, which effectively captures the leading edge curvature without introducing singularities. Furthermore, opposed to H-type grids, the boundary layer refinement only propagates downstream. Although it would be an advantage when the refined portion of the grid is aligned with the shear layer of the wake, this alignment is rarely achieved.

The O-grid addresses some drawbacks of H and C-grids. It wraps the entire grid around the airfoil without propagating any boundary-layer fineness into the field, resulting in an optimal cell count, eliminating redundant cell propagation seen in H and C-type patterns. The major limitation of O-grids is to handle zero-thickness trailing edges, where highly skewed cells will be generated. Since this study deals with airfoils with sharp trailing edges, a C-type grid was selected consisting of 7 blocks. Figure 4.4 shows a depiction of this grid topology, accompanied by its dimensional and meshing parameters.

A good quality mesh should be independent; the results from a simulation remain consistent regardless of further refinement of the mesh. Common practice is to increase the resolution until convergence is reached. The grid parameters that will be considered are shown in Table 4.4. The parameters are continuously doubled except for Grid 3 to 4, where they are increased by 50%.

Table 4.4: Grid parameters considered for mesh independence.

	n_{normal}	n_{inlet}	$n_{airfoil}$	n_{wake}	$n_{farwake}$	Grid size
Grid 1	64	23	64	25	25	64×251
Grid 2	128	45	128	50	50	128×501
Grid 3	256	90	256	100	100	256×1002
Grid 4	384	135	384	150	150	384×1503

Furthermore, the far field boundary should have a minimal impact on the results. Although the distance of the boundaries from the studied object is not the only aspect that determines their influence (read more in Section 4.5.2), it remains a significant factor to be addressed. Three topologies have been considered where the far field boundary is placed at $R = 5$, 15 and 25 airfoil chords. The corresponding geometrical parameters of the computational domain are shown in Table 4.5. All combinations of grids and topologies have been considered. The results can be found in Section 5.1.

Table 4.5: C-mesh topology parameters (in dimensionless multiples of airfoil chord c) considered for mesh independance.

	$r_{farfield}$	$r_{leading}$	$r_{trailing}$	r_{wake}	$r_{farwake}$
Topolgy 1	5	1	2	4	20
Topolgy 2	15	3	4	8	25
Topolgy 3	25	5	6	12	30

4.5.2. Boundary Conditions

For finite volume methods, boundary conditions need to be specified in order to handle the fluxes to be evaluated at the boundaries of the domain. For the simulations within the context of this work, these need to be specified at the inlet/ far field, the outlet, the sides and at the airfoil. The quantities that need to be specified are pressure p, temperature T, velocity vector u and turbulent thermal diffusivity α_t. Furthermore, in simulations with the Spalart-Allmaras turbulence model [40], boundary conditions need to be specified for the eddy viscosity ν_t, whereas for simulations using Menter's $k-\omega$ SST model [53] boundary conditions are required for the turbulent kinetic energy k and specific dissipation rate ω.

A challenge associated with finite volume methods on a confined domain, is the absence of known conditions directly on the domain's boundary; instead, these conditions are known at infinity. Enforcing free-stream conditions within the bounded domain can introduce undesired wave reflections, potentially causing strong instabilities.

To address this, specific boundary conditions have been implemented to limit reflective behaviour. Recognizing the limitations of these measures, so-called *sponge zones* have been incorporated, which will be explored later in this section. First, the boundary conditions for each boundary will be given.

Inlet/ Far Field

At the inlet, we enforce the free stream conditions. Pressure p, temperature T, they are set at their free stream values of 1. The free stream velocity is calculated based on the Mach number M_∞ and angle of attack α according to Equation (4.41). The initial assignment for the turbulent thermal diffusivity α_t is set to the physical free stream viscosity μ_∞ but is subsequently calculated through field assignment. For simulations implementing the Spalart-Allmaras model, the eddy viscosity at the inlet is set to $\nu_t = 5\nu_\infty$. For simulations with Menter's $k-\omega$ SST model, the inlet conditions for turbulent kinetic energy k are defined by:

$$k = \frac{3}{2}(Iu_\infty)^2\,, \tag{4.50}$$

where I denotes the turbulence intensity, which is set to 0.4%. Subsequently, the turbulent dissipation ϵ is computed as:

$$\epsilon = {C_\mu}^{3/4} \frac{k^{3/2}}{l_t} , \tag{4.51}$$

Here, l_t is the turbulent length scale, which is set to $0.01c$ and the model constant $C_\mu = 0.09$. The turbulent dissipation rate can then be calculated as:

$$\omega = \frac{\epsilon}{kC_\mu} . \tag{4.52}$$

Outlet

For all flow variables, except for pressure p, zero gradient boundary conditions are imposed at the outlet, adhering to Equation 4.53 for any flow variable ϕ. In OpenFoam, this is achieved through the build-in `zeroGradient` function.

$$\frac{\partial}{\partial n}\phi = 0 \tag{4.53}$$

For pressure p, the built-in `waveTransmissive` boundary condition is used. This specific boundary condition is designed to facilitate smoother outflow conditions, mitigating wave reflections. The boundary values are evaluated by solving the material derivative:

$$\frac{Dp}{Dt} = \frac{\partial p}{\partial t} + \boldsymbol{U} \cdot \nabla p = 0 , \tag{4.54}$$

Here, $\boldsymbol{U}$ is the advection velocity. It is assumed that the advection velocity is parallel to the boundary, which simplifies Equation (4.54) to:

$$\frac{Dp}{Dt} \approx \frac{\partial p}{\partial t} + U_n \cdot \frac{\partial p}{\partial n} = 0 , \tag{4.55}$$

The advection velocity is then evaluated as the sum of velocity component normal to the boundary and the free stream speed of sound c_∞,

$$U_n = u_n + c_\infty . \tag{4.56}$$

Sides

OpenFOAM lacks specialized tools for handling two-dimensional domains. In the absence of dedicated mechanisms for 2D simulations, a 2D mesh in OpenFOAM features twice as many faces on the front and back as there are cells. To address this, the built-in `empty` boundary condition is imposed on the sides of the computational domain. Essentially, this condition instructs the solver to ignore the additional faces.

Airfoil

Given the large number of simulations required for this research, the decision has been made to utilize wall functions. This choice is motivated by the advantages of reducing the need for excessive mesh refinement near the walls, lowering the computational requirements. Wall functions are empirical relations employed to capture the physical flow behavior in the vicinity of walls. The law of the wall, first introduced by von Kármán [67], defines the non-dimensionalized velocity u^+ and normal distance y^+ as follows:

$$u^+ = \frac{u}{u_\tau} , \quad y^+ = y\frac{u_\tau}{\rho} , \tag{4.57}$$

Here, u_τ denotes the shear velocity, which has no physical meaning.

$$u_\tau = \sqrt{\frac{\tau}{\rho}} , \quad \tau = \mu\frac{du}{dy} , \tag{4.58}$$

The relation between u^+ and y^+ for the log-law region is given by Equation 4.59, where κ, E and C^+ are constants.

$$u^+ = \frac{1}{\kappa} \ln E y^+ + C^+ , \tag{4.59}$$

OpenFOAM implements the logarithmic wall law when the grid is appropriately spaced ($y^+ > 30$). The other quantities, derived from Favre-avaraging the Navier-Stokes equations, can also be

transformed to self-similar variables. For the eddy viscosity ν_t, we use the OpenFOAM function `nutUSpaldingWallFunction`, which uses the following relation for the eddy viscosity in the near-wall region:

$$\nu_t = \nu \cdot \left(\frac{\kappa y^+}{\ln\left(E y^+\right)} - 1 \right) \tag{4.60}$$

To calculate y^+, the logaritmic law from Equation (4.59) is slightly modified. The left-hand side of the equation is multiplied by $(y/\nu)/(y/\nu)$,

$$\frac{u}{u_\tau y/\nu} \cdot (y/\nu) = \frac{u}{y^+} \cdot (y/\nu) = \frac{1}{\kappa} \ln\left(E y^+\right) \,, \tag{4.61}$$

from which we obtain:

$$y^+ \ln\left(E y^+\right) - \frac{\kappa y U_p}{\nu} = 0 \,, \tag{4.62}$$

which is solved using the iterative Newton-Raphson method:

$$y^+_{n+1} = y^+_n - \frac{f\left(y^+\right)}{f'(y+)} = y^+_n - \frac{y^+_n \ln\left(E y^+_n\right) - \frac{\kappa y U_c}{\nu}}{1 + \ln\left(E y^+_n\right)} = \frac{y^+_n + \frac{\kappa y U_c}{\nu}}{1 + \ln\left(E y^+_n\right)} \,. \tag{4.63}$$

The built-in OpenFOAM function `kqRWallFunction` is applied for the turbulent kinetic energy k, which imposes Neumann boundary conditions. For turbulent dissipation rate ω, the `omegaWallFunction` is used. The function calculates the value for the viscous and log law layer at the cell face, subsequently blending them and calculating the value at each cell center. The `compressible::alphatWallFunction` provides a boundary condition for the turbulent thermal diffusivity α_t.

Lastly, boundary conditions are necessary for the velocity, temperature, and pressure at the wall. The no-slip condition is applied for the velocity, which means that the velocity $\mathbf{u}_{wall}$ at the wall is set to zero. The temperature is fixed at a constant value of $T_{wall} = 1$, equal to the free stream temperature. For the pressure, the `zeroGradient` conditions is used (refer to Equation (4.53)).

Sponge Zones

As previously highlighted, the issue of wave reflections poses a considerable challenge for Finite Volume (FV) methods. While certain implemented boundary conditions mitigate these effects to some extent, perfect non-reflectivity will not be achieved. Consequently, sponge zones have been integrated into the setup. A sketch of the sponge zone is shown in Figure 4.5.

In this area, the solution is damped to a known reference solution; i.e., the free stream values. Damping is introduced through the addition of a non-physical term in the Favre-Averaged Navier-Stokes equations (4.13) - (4.16). Consequently, the governing equations to be solved in the sponge zone are modified as follows:

$$\frac{\partial \bar{\rho}}{\partial t} + \frac{\partial}{\partial x_j}\left(\bar{\rho}\tilde{u}_j\right) = x_{k,damp} \cdot \left(\rho - \rho_\infty\right) \,, \tag{4.64}$$

$$\frac{\partial}{\partial t}\left(\bar{\rho}\tilde{u}_i\right) + \frac{\partial \bar{p}}{\partial x_i} + \frac{\partial}{\partial x_j}\left(\bar{\rho}\tilde{u}_i\tilde{u}_j - \bar{\tau}_{ij} + \overline{\rho u_i' u_j'}\right) = x_{k,damp} \cdot \left(\rho u_i - (\rho u_i)_\infty\right) \,, \tag{4.65}$$

$$\frac{\partial}{\partial t}(\bar{\rho}\tilde{H} - \bar{p}) + \frac{\partial}{\partial x_j}\left(\bar{\rho}\tilde{H}\tilde{u}_j + \bar{q}_j + \overline{\rho H' u_j'} - \tilde{u}_i\bar{\tau}_{ij}\right) = x_{k,damp} \cdot \left(E - E_\infty\right) \,, \tag{4.66}$$

The vector $x_{k,damp}$ contains the damping factors in x, y and z-direction (recall that OpenFOAM is strictly a 3D-solver). The damping factor is determined by an exponential relation that varies between 0 at the sponge boundary to 1 at the domain boundary. For the x-component of the damping factor, this becomes:

$$\text{if } \; x < x_{s,\,left} \; : \quad x_{damp} = \left(\frac{x - x_{s,\,left}}{x_{min} - x_{s,\,left}} \right)^3 \,, \tag{4.67}$$

$$\text{if } \; x > x_{s,\,right} \; : \quad x_{damp} = \left(\frac{x - x_{s,\,right}}{x_{max} - x_{s,\,right}} \right)^3 \,. \tag{4.68}$$

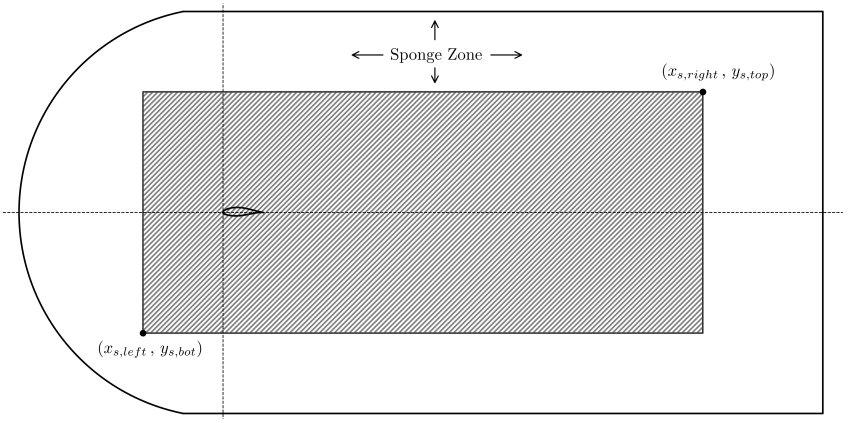

Figure 4.5: Geometry of the sponge zone within the computational domain. The hashed zone is evaluated without the damping term.

4.6. Design Space

The problem can be formulated using four dimensionless groups: the free stream Mach number M_∞, chord-based Reynolds number Re_c, specific heat ratio γ, and Prandtl number Pr, with the latter two kept at fixed values. In addition, an airfoil needs to be specified with an angle of attack α for each simulation. The selected airfoil is the company's design airfoil: NACA 63(4)-421. Consequently, we have three quantities for which a specific set must be determined: M_∞, Re_c and α. In this section, considerations will be given on how this set is derived.

The primary outputs from the CFD simulations are lift and drag polars, serving as input for the lifting line method detailed in Part III of this work. Consequently, it must be known what range of angles of attack and Mach numbers the simulated rotor will be subjected to. This poses a problem, as simulations under compressible conditions require the possession of these coefficients. Despite this limitation, an initial (conservative) estimate of typical flow conditions can be obtained since we have access to the following:

- The in-house lifting line code.
- Incompressible polars for the NACA 63(4)-421 airfoil generated by xFoil [68].
- The test rotor for the lifting line simulations of Part III, as described in Section 7.2.
- Incoming wind speed U_0 is derived according to Gonzalez-Aparicia et al. [69]. Wind speeds exceeding $30\,\mathrm{m/s}$ occurred five times in 2020 at the North Sea. Hence, a wind speed of $U_0 = 30\,\mathrm{m/s}$ is considered, since the primary focus of this work is simulating the rotor under critical conditions.

Lastly, we need an estimate of the tip speed ratio λ, where compressible effects would be significant. Assuming the drag divergence occurs at $M_\infty = 0.65$, we can calculate the tip speed ratio as,

$$\begin{aligned} \lambda &= \frac{\bar{M}_{\infty,tip}\; c_\infty}{U_0}\,, \\ \lambda &= \frac{0.65 \times 340\,\mathrm{m/s}}{30\,\mathrm{m/s}} \approx 7.4\,, \end{aligned} \tag{4.69}$$

where $\bar{M}_{\infty,\text{tip}}$ is the average Mach number at the tips (recall that a tilted rotor has an advancing and retreating side).

The tip conditions along the azimuth ϕ resulting from these preliminary simulations are illustrated in Figure 4.6 for angle of attack α and free stream Mach number M_∞. The figure reveals that on the advancing side, where the Mach number peaks, the angle of attack is at its lowest. Conversely, on the retreating side ($\phi \approx 180°$), the angle of attack reaches its maximum. In general, the angle of attack is confined to very low angles at these wind speeds for various tilt angles α_r. It should be noted that this is in contrast with traditional HAWTs, where the blades will be pitched out and operate in stall ($\alpha < -8°$). As indicated by De Tavernier and von Terzi [4], this is the critical operating regime where local supersonic flow could emerge for these types of turbine.

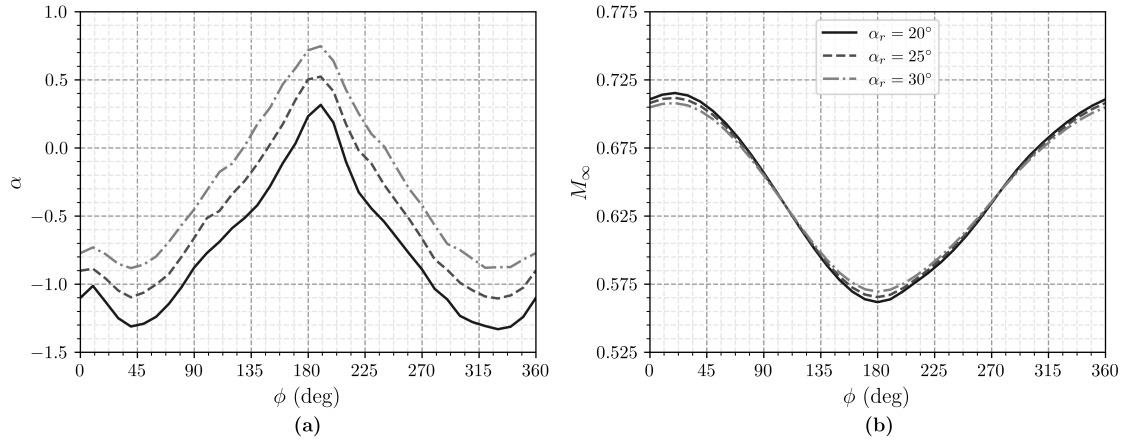

Figure 4.6: Conservative estimate of typical blade tip conditions for angle of attack α **(a)** and tip Mach number $M_{\infty,tip}$ **(b)** under varying tilt angle α_r.

Furthermore, Figure 4.7 shows the variation in angle of attack and chord-based Reynolds number for the full rotor during a complete rotation. Near the blade's root, on the retreating side, conditions associated with stall and post-stall are encountered. The Reynolds number shows significant variation dependent on blade position and distance from the root, ranging from 5.0×10^6 to 80.0×10^6.

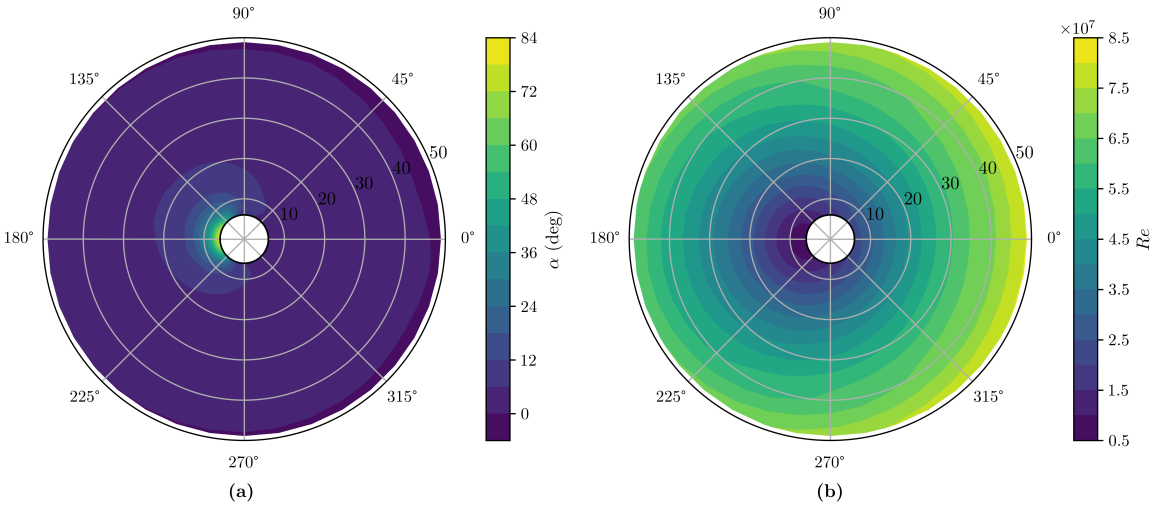

Figure 4.7: Conservative estimate of typical flow conditions for angle of attack α **(a)** and chord-based Reynolds number Re_c **(b)**.

It should be stressed that what has been presented in this section is purely indicative and serves to provide a reference point from which an efficient design space can be derived (i.e., minimal amount of unnecessary data points). However, the aim of this research is not confined to simulating a rotor using a lifting line method. It also seeks to provide insights in the governing physics of a thick airfoil under high subsonic and transonic flow conditions, which necessitates a sufficient amount of data points. The following considerations will outline the decisions that have been made for the three input quantities:

Angle of attack α

It has been shown that the blades are predominantly subjected to low angles of attack during critical conditions. Consequently, simulations ranging from $-5°$ to $5°$ have been deemed adequate. This also allows for the analysis of cases where a shock wave will terminate on both the suction and pressure side of the airfoil. Unlike for incompressible flow, the lift polar in the transonic regime will not be linear, necessitating a sufficiently

small interval, which has been set to $1.25°$. Additionally, stall and post-stall have to be accounted for. While post-stall coefficients can be approximated using various methods, the accuracy of these methods depends on accurate coefficients for the stall. Therefore, additional data points will be created within a range of $-10° \leq \alpha \leq 15°$. These conditions are only found near the root; therefore, only subsonic cases have been included.

Free stream Mach number M_∞

The Mach number range has been set from 0.2 to 0.8. This will span the full range of Mach numbers perceived by the rotor blades. The lower boundary will serve as a reference, or incompressible, Mach number, which is used to assess the adequateness of the compressibility corrections explained in Section 2.2. While the upper limit is highly theoretical in the context of wind turbine operation, it can provide insights into the behavior of shock waves and transonic buffet.

Chord-based Reynolds number Re_c

Figure 4.7b shows a wide range of Reynolds numbers encountered by the blades. In numerical approaches that rely on polars, accommodating for every minor variation in Reynolds number is not feasible. Typically, only a few sets of polars with large steps in Reynolds number are utilized. Variations in Mach number inevitably lead to changes in Reynolds number, but as also indicated by Wood [6] the effect of the Mach number is much more significant in the high-speed configurations that will be studied. Additionally, as has been pointed out in Section 4.5.2, the implementation of wall functions limits us to simulating a turbulent boundary layer only, while the state of the boundary layer is one of the main effects of the Reynolds number. Hence, drag will still be overestimated when simulating low Reynolds number flows (conditions near the root). It should also be noted that this work primarily focuses on the impact of Mach number. The theoretical test rotor described in Section 7.2 is theoretical, and we're interested in trends rather than simulating the rotor as accurately as possible. Considering the aforementioned factors, it has been decided to prioritize data points for variations in angle of attack and Mach number, while keeping the Reynolds number fixed at 18.0×10^6.

The final design space is shown in Figure 4.8. The boundary between the subsonic (light blue) and supersonic (dark blue) regimes denotes the estimation of the flow conditions where the critical pressure coefficient $C_{p,crit}$ (refer to Equation (2.16)) is reached. These are calculated according to the corrections described in Section 2.2. For clarity, the test points related to stall are not included in Figure 4.8. These simulations will be run at a Mach number of $M_\infty = 0.2$.

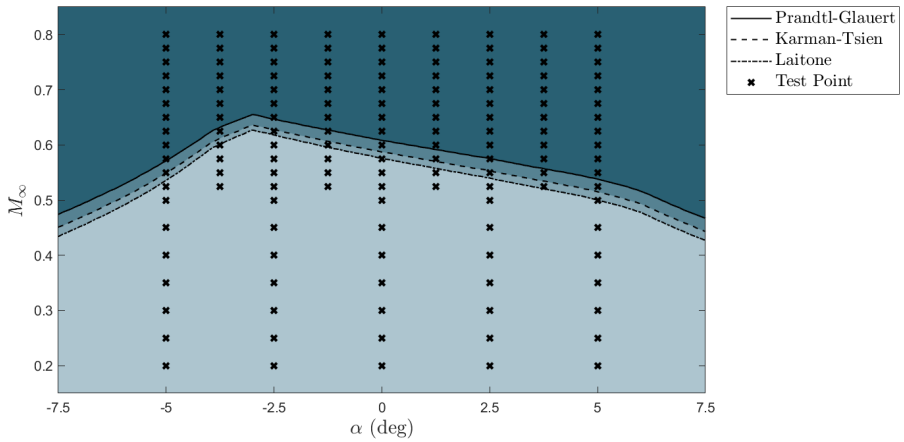

Figure 4.8: Design space for the CFD simulations. The subsonic (light blue) and supersonic (dark blue) regimes have been estimated using xFoil [68].

5

CFD: Verification/ Validation

For all numerical simulations, errors will emerge from either assumptions or the employed numerical schemes. The primary objective of this chapter is to examine these errors and, most importantly, assess whether they fall within acceptable margins. *Verification* is a quality control process and in the context of this CFD setup, it refers to the mesh independence study. Furthermore, it is common practice to compare CFD outcomes to experimental findings, a quality assurance process referred to as *validation*.

The first section of this chapter will present the results of the mesh independence study. The objective of this section is to mitigate the influence of mesh resolution and the size of the computational domain on simulation outcomes. The numerical grids that will be evaluated in this section have been described in section 4.5.

After a mesh has been established that is deemed independent, the setup can be validated. A primary requirement is its capability to simulate both low-speed and high-speed flows ($0.1 < M < 0.8$). Section 5.2 will present the validation results for two thick airfoils at flow velocities that can be viewed as incompressible ($M = 0.2$). Both profiles have a relative thickness of $t/c = 21\%$, common for wind turbine applications.

Section 5.3 addresses the high-speed validation of the setup. Again, Two airfoils will be examined in this context. Since wind turbine profiles have never been experimentally tested at transonic flow velocities, supercritical profiles are chosen for investigation. Firstly, a steady case will be studied at a Mach number of $M = 0.723$. Subsequently, an unsteady flow case is examined, considering the anticipated unsteady behavior arising from transonic buffet.

For all validation cases, except for the unsteady high-speed validation, two finite volume solvers and two turbulence models are considered. These have been selected based on literature in Section 4.2 and 4.4 respectively.

5.1. Mesh Independence

For the assurance of an independent mesh, four grids and three topologies have been defined in Section 4.5.1. From Grid 1 to 3 the resolution is multiplied by 2 (in normal and tangential direction) for each step and by 1.5 for Grid 3 to 4 (refer to Table 4.4). For the considered topologies, the far field boundary is placed at 5, 15 and 25 chords from the airfoil for Topology 1, 2 and 3 respectively (refer to Table 4.5). Furthermore, the flow conditions for this study should be representative for the simulations of the design space; specifically, the presence of a shock wave is deemed essential. A steady flow field is desirable to avoid averaging errors. Consequently, the specified flow conditions are a Mach number M_∞ of 0.65, a chord-based Reynolds number Re_c of 18.0×10^6, and an angle of attack α of $0°$. The employed numerical finite volume solver is *rhoEnergyFoam*, with Menter's $k - \omega$ SST serving as closure model for the turbulent calculations.

Firstly, attention can be directed towards the simulated aerodynamic coefficients given in Table 5.1. When specifically addressing grid refinement, the findings indicate that a satisfactory level of convergence is reached with Grid 3. Subsequent refinement to Grid 4 results in marginal differences of the simulated lift and drag, suggesting mesh independence is achieved. Convergence of the mesh for transonic flows is primarily dominated by the resolution around the shocked area of the flow. For Grid

Table 5.1: Aerodynamic coefficients obtained for mesh independence and topology study.

	Topology 1		**Topology 2**		**Topology 3**	
	C_l	C_d	C_l	C_d	C_l	C_d
Grid 1	0.382	0.0177	0.398	0.0170	0.404	0.0167
Grid 2	0.377	0.0172	0.392	0.0165	0.396	0.0164
Grid 3	0.390	0.0176	0.408	0.0168	0.413	0.0167
Grid 4	0.392	0.0176	0.410	0.0169	0.414	0.0167

1, the shock resolution is approximately $0.022\,c$, whereas for the finest Grid 4, this value decreases to $0.0036\,c$.

The influence of the resolution in the vicinity of a shock becomes evident when examining the pressure coefficients in Figure 5.1. The curves align well across all grid configurations, except for shock region. A magnified view of the pressure coefficient near the shock in Figure 5.1b reveals the pronounced effect of mesh refinement on the shock wave's properties. For an increasing shock resolution, the static pressure rise associated with the shock becomes more abrupt and the shock's strength is also affected. The differences between Grid 3 and Grid 4, while present, are considered insufficient to justify the significant increase in computational time.

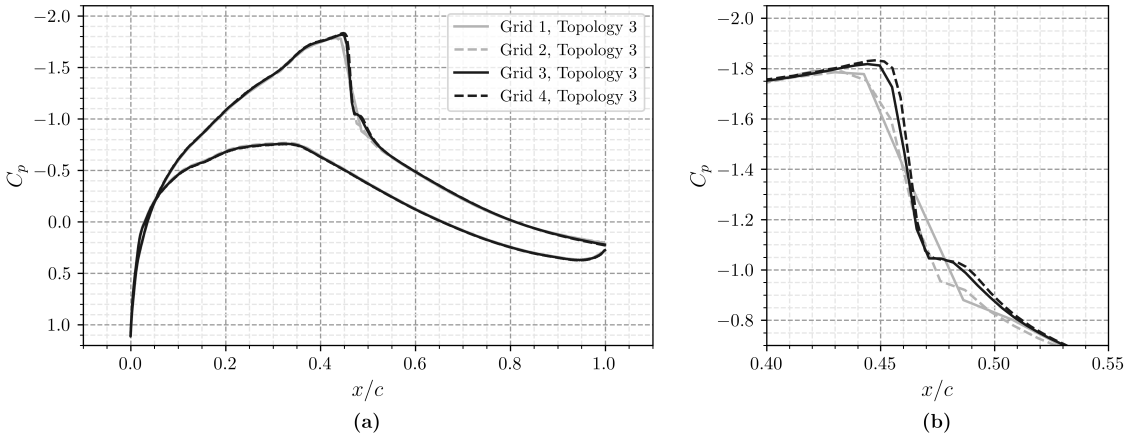

Figure 5.1: Effect of grid refinement on the pressure coefficient C_p: **(a)** shows the continuous curve, whereas **(b)** provides a magnified view of the shock. $M_\infty = 0.65$, $Re_c = 18.0 \times 10^6$ and $\alpha = 0°$.

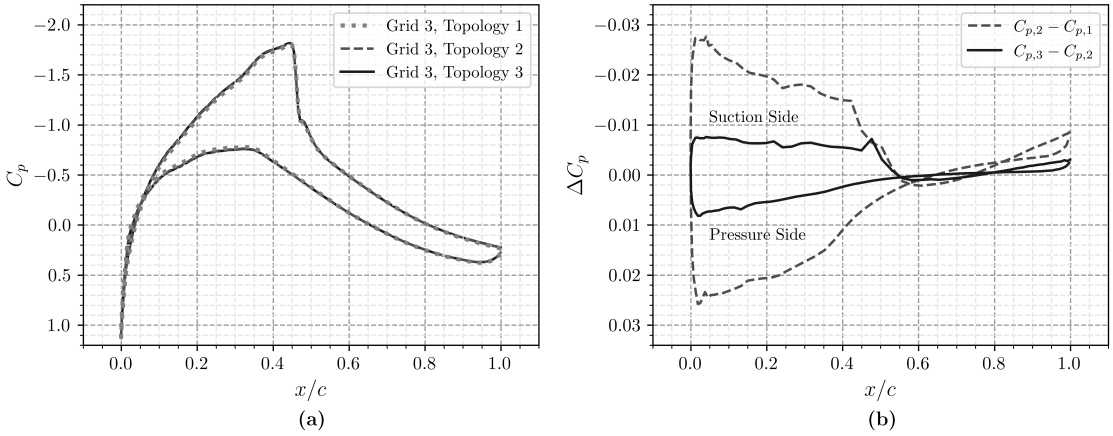

Figure 5.2: Effect of far field boundary distance on the pressure coefficient C_p for $x/c \in [0.1, 0.5]$: **(a)** shows suction side and **(b)** the pressure side. $M_\infty = 0.65$, $Re_c = 18.0 \times 10^6$ and $\alpha = 0°$.

The pressure fields at the suction side are shown in Figure 5.3. Examining the supersonic flow region and the shock wave reveals notable disparities between the first three grids, consistent with what has been stated before. Grid 3 (Figure 5.3c) and Grid 4 (Figure 5.3d) can barely be distinguished

Upon revisiting Table 5.1, it becomes clear that the impact of the far field boundary on the aerodynamic coefficients is significant. Although this impact diminishes from Topology 2 to 3. The calculated pressure coefficients for Grid 3, shown in Figure 5.2a, do not immediately provide a clear distinction between the topologies. For better clarity, Figure 5.2b shows the difference in pressure coefficient between Topologies 1 and 2, as well as between 2 and 3. Here, we can clearly see that the suction side experiences an increased pressure when the far field boundary is located in closer proximity to the airfoil, while the pressure side encounters a reduction. This leads to a lower simulated lift coefficient C_l, consistent with the results from Table 5.1.

Placing the boundary 25 chords away from the airfoil (Topology 3), instead of 15 (Topology 2), has a marginal effect on the results ($|\Delta C_p| < 0.01$). Nevertheless, it does not incur additional computational costs. Therefore, Topology 3 is selected for subsequent simulations.

In conclusion, Grid 3 and Topology 3 are selected for the subsequent simulations of this research. The selected computational mesh is shown in Figure 5.4 for the NACA 63(4)-421 airfoil, with a wall spacing appropriate for a chord-based Reynolds number Re_c of 18.0×10^6. The Reynolds number will vary for different simulations of the validation sequence. The grid will be stretched towards the wall accordingly, so that the first cell center will remain well within the log layer.

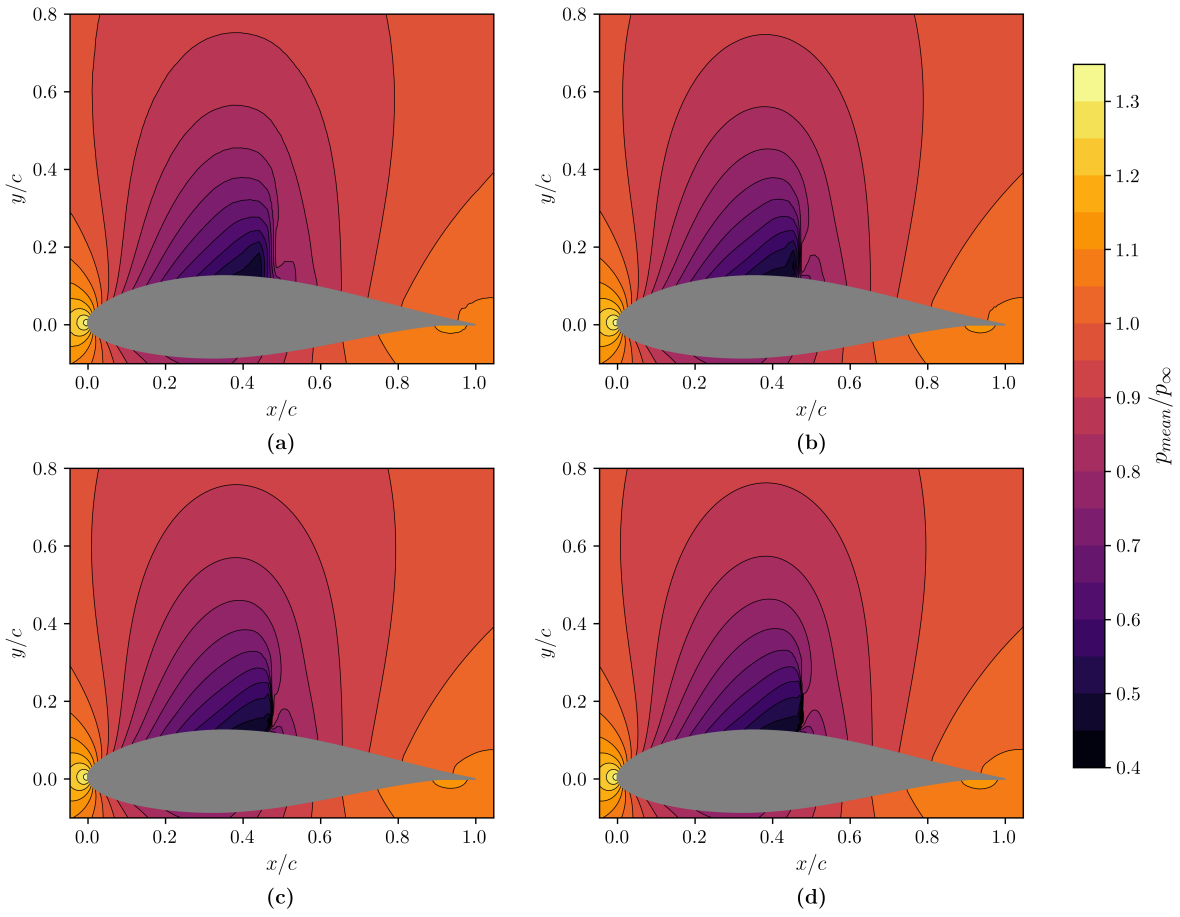

Figure 5.3: Mean non-dimensional pressure field p_{mean}/p_∞ from coarsest (Grid 1) **(a)** to finest (Grid 4) **(d)** with Topology 3. $M_\infty = 0.65$, $Re_c = 18.0 \times 10^6$ and $\alpha = 0°$.

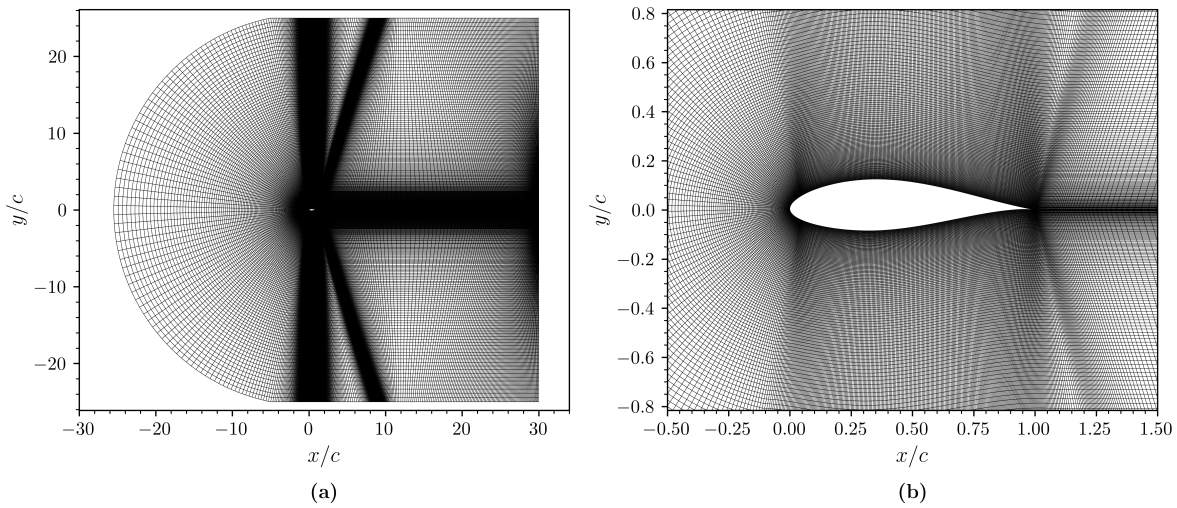

Figure 5.4: Selected C-mesh with grid dimensions 256×1002: **(a)** shows the entire computational domain and **(b)** an enlarged view around the NACA 63(4)-421 airfoil.

5.2. Low-Speed Validation

We consider flow conditions where the incompressible assumption remains valid ($M < 0.3$). The interest of the low-speed validation is dedicated to the solver's ability to predict the aerodynamic coefficients for lift C_l and drag C_d, since these will serve as input to the lifting line model treated in Part III of this research.

The selected airfoils are the NACA 63(4)-421 and the S809, shown in Figure 5.5. The NACA profile serves as the primary selection, being the current design airfoil for TouchWind which will be used for the design space simulations. The experimental data for the NACA profile is characterized by a free boundary layer transition from laminar to turbulent. The state of the boundary layer (laminar or turbulent) mildly influences lift and greatly influences drag. As has been explained in section 4.5.2, wall functions are implemented, meaning that the simulated boundary layer is characterized by a turbulent state. This will result in an overprediction of the simulated drag coefficient compared to the experimental data.

Since no experimental data is available for the NACA profile with a fixed transition, an additional airfoil is considered: The S809. For this airfoil, experiments have also been conducted for a tripped boundary layer.

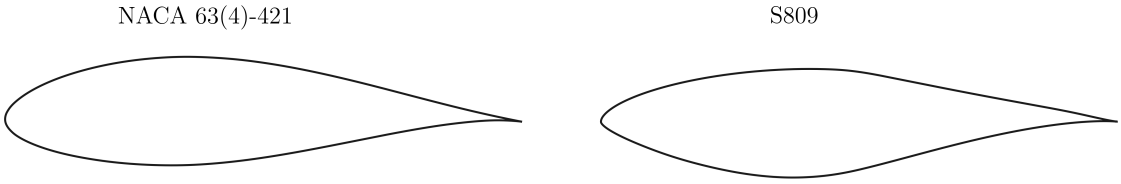

Figure 5.5: Airfoils considered for low-speed validation.

5.2.1. NACA 63(4)-421

The 21% thick, NACA 63(4)-421 airfoil, has been experimentally tested [70] for chord-based Reynolds numbers $Re_c = 3.0$, 6.0 and 9.0×10^6. The latter data set is selected for validation. The experimental data, xFoil data [68] (forced transition at $x/c = 0.02$) and URANS results are shown in Figure 5.6. The lift polar shows to be in good accordance with the experiment for all selected solvers and turbulence models. As expected, drag is overestimated due to the boundary layer being modeled as turbulent. Compared to xFoil [68], the data seems to match well, especially for the *rhoEnergyFoam* solver with Menter's $k - \omega$ SST closure model. Nevertheless, it is questionable to draw a qualitative conclusion for the best performing combination of solver and turbulence model based on a low-fidelity method as xFoil.

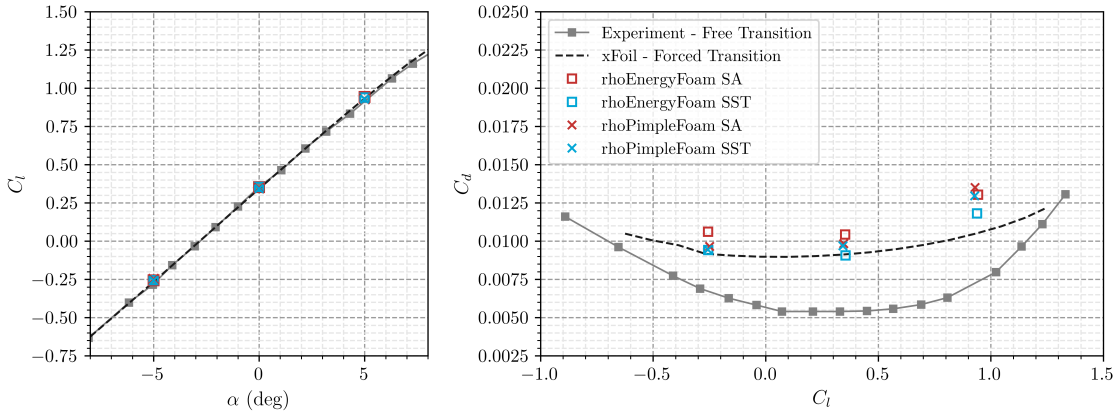

Figure 5.6: Lift **(a)** and drag **(b)** polars for NACA 63(4)-421 validation sequence at $Re_c = 9.0 \times 10^6$. For the URANS simulations the Mach number was set at $M_\infty = 0.2$.

The validation data is also given in Table 5.2, including the error compared to the experimental and xFoil data for lift and drag, respectively. Among the various solver-turbulence model combinations, the *rhoEnergyFoam* solver coupled with Menter's $k-\omega$ SST turbulence model exhibits the lowest error, amounting to $\epsilon_{mean} = 4.15\%$. The highest error is observed for the same solver paired with the Spalart-Allmaras model, yielding $\epsilon_{mean} = 9.70\%$.

Table 5.2: Aerodynamic coefficients for the NACA 63(4)-421 airfoil validation sequence at $Re_c = 9.0 \times 10^6$. Errors are calculated with respect to bold reference value.

		$\alpha = -5.00°$		$\alpha = 0.00°$		$\alpha = 5.00°$	
		C_l	C_d	C_l	C_d	C_l	C_d
Experiment [70]	Free Transition	**-0.285**	0.0069	**0.354**	0.0054	**0.913**	0.0071
xFoil [68]	Forced Transition	-0.266	**0.0095**	0.341	**0.0093**	0.926	**0.0109**
rhoEnergyFoam	Spalart-Allmaras	-0.256 (10.1%)	0.0106 (12.1%)	0.353 (0.29%)	0.0104 (12.4%)	0.943 (3.24%)	0.0130 (20.0%)
	$k-\omega$ Menter SST	-0.255 (10.5%)	0.0094 (0.52%)	0.335 (0.21%)	0.0091 (2.24%)	0.939 (2.77%)	0.0118 (8.73%)
rhoPimpleFoam	Spalart-Allmaras	-0.249 (12.7%)	0.0096 (1.87%)	0.347 (2.03%)	0.0098 (6.03%)	0.930 (1.84%)	0.0135 (24.3%)
	$k-\omega$ Menter SST	-0.257 (9.96%)	0.0094 (0.29%)	0.343 (3.13%)	0.0097 (4.41%)	0.928 (1.62%)	0.0129 (19.2%)

5.2.2. S809

Due to the lack of tripped experimental data for the NACA 63(4)-421 airfoil, the low-speed validation procedure is repeated for the S809 airfoil. The profile has a thickness to chord ratio of 21% has been developed specifically for wind turbine applications. The design and experimental campaign has been performed by Somers [71] at the TU Delft low-speed wind tunnel facility. Its primary design objectives were restrained maximum lift and low profile drag. Both free and forced transition measurements were documented for a Reynolds number $Re_c = 3.0 \times 10^6$. For the forced transitions, the boundary layer was tripped utilizing a surface roughness at $x/c = 0.02$ on the suction side and $x/c = 0.05$ on the pressure side.

A comparison of the calculated and experimental polars is shown in Figure 5.7. Overall, the URANS simulation results correspond well with the experimental data for tripped conditions, accurately reproducing both the lift and drag coefficients. This is not true for the results obtained using the *rhoPimpleFoam* solver coupled with the Spalart-Allmaras turbulence model.

The validation data, along with its corresponding errors, is given in Table 5.3. It is important to highlight that the errors for lift are computed relative to the experiments with free transition, while the

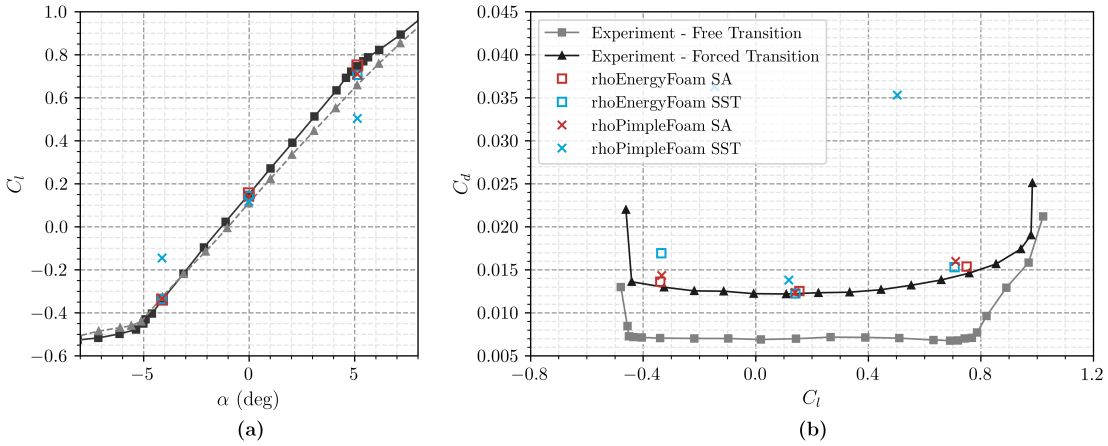

Figure 5.7: Lift **(a)** and drag **(b)** polars for S809 validation sequence at $Re_c = 3.0 \times 10^6$. For the URANS simulations the Mach number was set at $M_\infty = 0.2$.

drag errors are calculated with respect to the forced transition experiments. This distinction is made since surface roughness in the wind tunnel experiments adversely affects the lift of the airfoil. This can be regarded as a secondary effect independent of the boundary layer development. This roughness effect observed in the wind tunnel experiments is not present in the CFD simulations.

The smallest mean error resulted from the *rhoEnergyFoam* solver coupled with the Spalart-Allmaras turbulence model, where $\epsilon = 3.90\%$, closely followed by *rhoPimpleFoam* with Spalart-Allmaras and *rhoEnergyFoam* with $k-\omega$ Menter SST, where $\epsilon = 6.54\%$ and $\epsilon = 8.63\%$ respectively. As mentioned before, *rhoPimpleFoam* with $k-\omega$ Menter SST performed very poorly, leading to a mean error of $\epsilon = 92.89\%$.

Table 5.3: Aerodynamic coefficients for the S809 airfoil validation sequence at $Re_c = 3.0 \times 10^6$. Errors are calculated with respect to bold reference value.

		$\alpha = -4.12°$		$\alpha = -0.01°$		$\alpha = 5.13°$	
		C_l	C_d	C_l	C_d	C_l	C_d
Experiment [71]	Free Transition	**-0.339**	0.0071	**0.148**	0.0070	**0.747**	0.0070
	Forced Transition	-0.325	**0.0130**	0.109	**0.0122**	0.659	**0.0138**
rhoEnergyFoam	Spalart-Allmaras	-0.339 (0.00%)	0.0136 (4.61%)	0.155 (4.72%)	0.0125 (2.46%)	0.750 (0.04%)	0.0154 (11.6%)
	$k-\omega$ Menter SST	-0.336 (0.88%)	0.0169 (30.0%)	0.141 (4.70%)	0.0122 (0.00%)	0.707 (5.35%)	0.0153 (10.9%)
rhoPimpleFoam	Spalart-Allmaras	-0.334 (1.47%)	0.0143 (10.0%)	0.140 (5.41%)	0.0124 (1.63%)	0.711 (4.8%)	0.0160 (15.9%)
	$k-\omega$ Menter SST	-0.145 (142.6%)	0.0363 (179.2%)	0.118 (20.3%)	0.0138 (13.1%)	0.502 (32.8%)	0.0340 (146.3%)

5.3. High-Speed Validation

The primary focus of the low-speed validation, discussed in the previous section 5.2, was solely dedicated to evaluating the solver's capability of predicting the aerodynamic coefficients. While this remains a crucial aspect for the high-speed validation, there is an additional interest in assessing the solver's proficiency in accurately capturing the characteristics of the shock wave. Furthermore, the objective extends to examining the solver's capability to predict the unsteady flow phenomena associated with transonic buffet.

The airfoils selected for the high-speed validation sequence are the RAE2822 and OAT15a, as illustrated in Figure 5.8. Since experimental transonic data for thick airfoils is unavailable, supercritical

profiles have been utilized. This type of airfoil is designed specifically for transonic to supersonic flow velocities. The profiles are characterized by a flattened upper surface, positioning the shock as far aft as possible. This design aims to minimize wave drag and mitigate shock-induced boundary layer separation.



Figure 5.8: Airfoils considered for high-speed validation.

5.3.1. Steady Flow: RAE 2822

The RAE 2822 airfoil has been experimentally tested by Cook et al. [61] at the Royal Aircraft Establishment (RAE) transonic wind tunnel facility. Various flow conditions were considered. However, the most widely used test case for code validation used the following flow conditions: $M_\infty = 0.729$, $\alpha = 2.31°$ and $Re_c = 6.5 \times 10^6$. Furthermore, boundary layer transition has been fixed at $x/c = 0.03$ on the suction and pressure side.

The simulations have again been executed for the four combinations of solver and turbulence model. The resulting aerodynamic coefficients are summarized in Table 5.4. It follows that the drag is very well estimated by the *rhoEnergyFoam* solver combined with Menter's $k-\omega$ SST model. For the lift coefficient, all simulations are in good accordance with the experiment, except for the *rhoPimpleFoam* solver coupled with Spalart-Allmaras turbulence model.

Table 5.4: Aerodynamic coefficients for the RAE2822 airfoil validation sequence at $M_\infty = 0.729$ $Re_c = 6.5 \times 10^6$ and $\alpha = 2.31°$.

		C_l	Error	C_d	Error
Experiment [61]	Forced Transition	0.743	-	0.0127	-
rhoEnergyFoam	Spalart-Allmaras	0.704	5.24%	0.0143	12.60%
	$k-\omega$ Menter SST	0.701	5.65%	0.0129	1.57%
rhoPimpleFoam	Spalart-Allmaras	0.670	9.83%	0.0143	12.60%
	$k-\omega$ Menter SST	0.710	4.44%	0.0137	7.87%

Aside from the aerodynamic coefficients, the reference data from Cook et al. [61] includes pressure measurements along the airfoil surface. The results are shown in Figure 5.9. The differences between

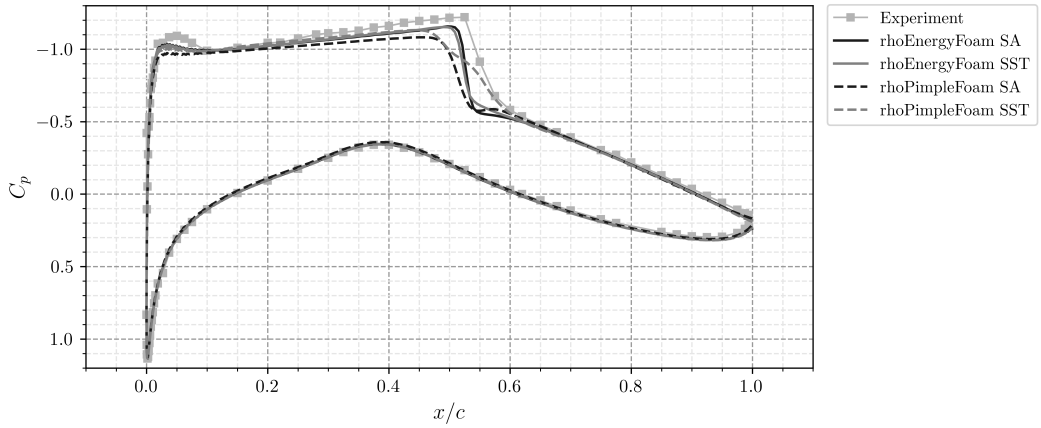

Figure 5.9: Pressure Coefficient C_p for the RAE 2822 airfoil.

the simulated and experimental results are minimal outside the shocked flow regime. For the shock itself, both solvers predict the shock positions slightly upstream compared to the experiment. It should be noted that Figure 5.9 shows the mean quantities for C_p. The simulations using the *rhoPimpleFoam* solver coupled with Menter's $k-\omega$ SST model showed transient behaviour. Hence, the shock seems less abrupt in Figure 5.9. Furthermore, the simulations executed with the *rhoEnergyFoam* solver show to be in accordance with the experimental results. The Mach number contours are depicted in Figure 5.10, with the thick lines indicating the sonic condition ($M = 1$). The contour lines produced by the *rhoEnergyFoam* solver demonstrate the closest alignment with the NASA verification data produced by Slater [72], retrieved from the WIND code.

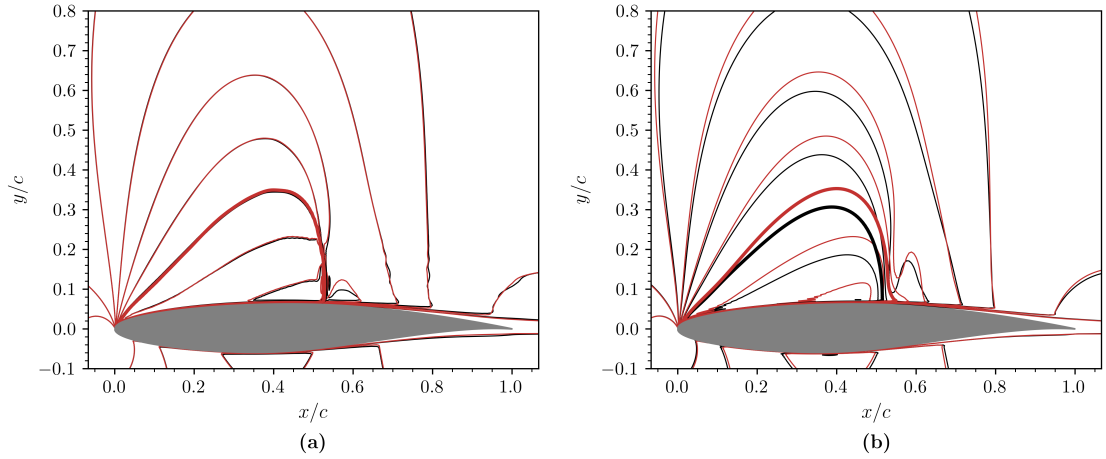

Figure 5.10: Mach contours for *rhoEnergyFoam* **(a)** and *rhoPimpleFoam* **(b)** solvers. Black and red contours correspond to Spalart-Allmaras and Menter $k-\omega$ SST models, respectively. $M_\infty = 0.729$, $Re_c = 6.5 \times 10^6$ and $\alpha = 2.31°$.

5.3.2. Unsteady Flow: OAT15a

Jacquin et al. [26] conducted an experimental campaign in the transonic S3 wind tunnel at the ONERA Centre of Chalais Meudon. The experiments were aimed at examining shock-induced oscillations on the OAT15a airfoil; a supercritical profile with blunt trailing edge ($e/c = 0.5\%$) and a thickness-to-chord ratio of $t/c = 12.5\%$. The wind tunnel model had a chord length of $c = 230$ mm and was tested at a Mach number of $M_\infty = 0.73$ and chord-based Reynolds number $Re_c = 3.0 \times 10^6$. The study encompassed a range of angles of attack, spanning conditions from pre-buffet onset to well within the buffet regime. The flow was tripped on both the suction and pressure side at $x/c = 0.07$. The airfoil has been altered slightly from the original definition so that it closes at $c = 1$ with a sharp trailing edge. This adjustment was made to account for the C-mesh strategy detailed in Section 4.5.1. For this part of the validation,

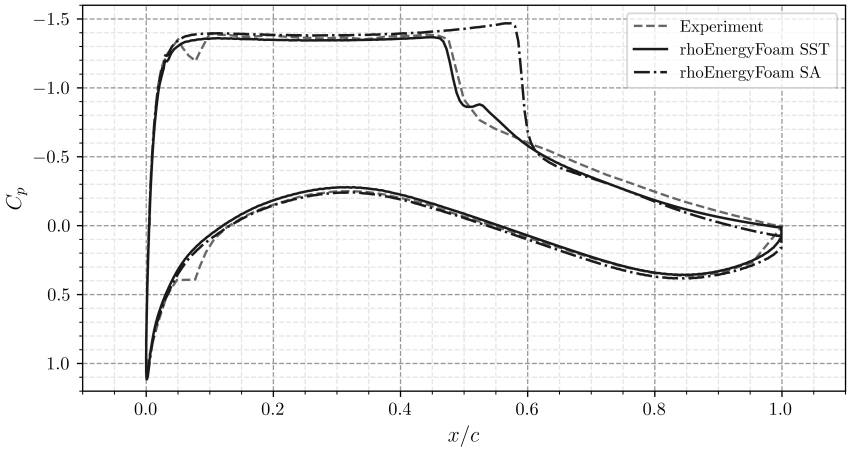

Figure 5.11: Pre-buffet onset pressure coefficient C_p for the OAT15a airfoil. $M_\infty = 0.73$, $Re_c = 3.0 \times 10^6$ and $\alpha = 3.0°$.

the *rhoPimpleFoam* solver has been excluded, based on the unsatisfactory outcomes it produced for the steady transonic case detailed in Section 5.3.1.

Firstly, Figure 5.11 shows the pressure coefficient for pre-buffet onset conditions. the Spalart-Allmaras model positions the shock significantly further downstream compared to the experiment. For the Menter $k-\omega$ SST model, the calculated pressure shows better alignment with the experimental results.

When the angle of attack is increased, experimental data from [26] shows the onset of transonic buffet. Figure 5.12 shows the non-dimensionalized root-mean-square pressure fluctuations p_{rms} along the airfoil surface. Simulations with the Spalart-Allmaras model were unable to reproduce any of the shock-induced oscillations. Consequently, Figure 5.12 exclusively shows the results from Menter's $k-\omega$ SST model. The simulations reveal weak oscillations compared to the experimental observations, an underestimation also found by Thiery and Coustols [10], who also solved the URANS equations and used Menter's $k-\omega$ SST turbulence model. They indicate that the disparities might be attributed to the tripping mechanism used in the experiments. The flow was tripped using grains, and the height could not be optimized for all the considered angles of attack. This potentially lead to over-thickening of the boundary layer, leading to more pronounced shock oscillations.

Although the oscillations are weaker than those reported in the experimental data, a distinct pattern is observed downstream of the shock: The root-mean-square pressure fluctuations initially decrease, then rise again as they approach the trailing edge. This pattern is indicative of shock-induced separation, simultaneously originating from the bubble's rearward expansion and the trailing edge, which periodically collapse into a single recirculation region. This phenomenon aligns the shock-induced boundary layer separation mechanism recorded in the experiments, aligning with Model B separation classification as described by Lachmann and Pearcy [7].

In conclusion, the results do not replicate the experimental tests to a satisfactory level. Nevertheless, simulations with Menter's $k-\omega$ SST model captured unsteady oscillations to some extent. It should also be noted, that the simulations of the design space (refer to Section 4.6) are conducted using a "thick" profile. Adverse pressure gradients will be significantly larger, thus narrowing the margin between buffet offset and onset. Nonetheless, it's important to acknowledge that the solver might still be prone to underestimating the magnitude of these fluctuations.

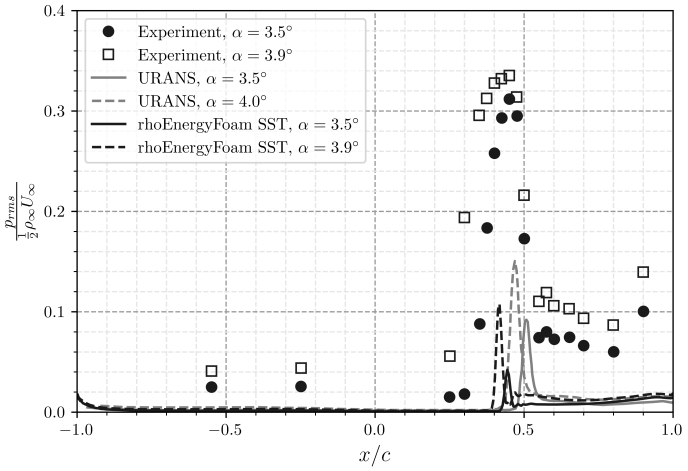

Figure 5.12: Root-mean-square pressure fluctuations p_{rms} along the OAT15a airfoil at $M = 0.73$ and $Re = 3.0 \times 10^6$. Experimental data is from Ref. [26] and URANS from Ref. [10]. Negative x/c corresponds to the airfoils pressure side.

5.4. Conclusion

The quantitative outcomes from the validation steps outlined in Sections 5.2 and 5.3 have been translated into a qualitative evaluation, ranging from – – (poor prediction) to + + (excelent prediction), presented in Table 5.5.

Overall, the *rhoEnergyFoam* solver, when combined with Menter's $k-\omega$ SST turbulence model, yielded the most reliable predictions across the evaluated scenarios. This set-up managed to capture the shock-induced oscillations for the OAT15a airfoil to a certain extent, which was not achieved by the Spalart-Allmaras model. Moreover, *rhoPimplefoam* produced inconsistent results for the low-speed cases

and did not accurately simulate the flow field for the RAE 2822 validation case, leading to its preliminary exclusion. In conclusion, the design space simulations will be carried out using the *rhoEnergyFoam* solver with Menter's $k-\omega$ SST turbulence model. Furthermore, in Section 5.1 it has already been established that the calculations will be performed on a grid of 256×1002 cells (Grid 3), with the far-field boundary positioned 25 chords away from the airfoil (Topology 3).

Table 5.5: Qualitative assessment of the validation cases.

	rhoEnergyFoam		*rhoPimpleFoam*	
	Spalart-Allmaras	Menter $k-\omega$ SST	Spalart-Allmaras	Menter $k-\omega$ SST
NACA 63(4)-421	+ –	+ +	+	+
S809	+ +	+	+	– –
RAE 2822	+	+ +	–	–
OAT15a	– –	+ –	n/a	n/a

6

CFD: Results & Discussion

In this chapter, the results of the URANS simulations are presented, with a particular focus on the implications of compressibility and transonic flow phenomena. The chapter first addresses the results related to the subcritical regime, which is mainly concerned with assessing the adequateness of the compressibility corrections. Subsequently, the results related to the onset of local supersonic flow will be presented in Section 6.2. Here, attention will be directed towards the shock characteristics and its impact on the resulting forces and unsteadiness. The obtained polar field will be presented in Section 6.3, which will serve as input for the lifting line method described in Part III of this work. In addition to the field's dependence on the angle of attack and Mach number variations, aerodynamic coefficients for stall within the subsonic regime will also be given. The chapter concludes with a discussion of the obtained results.

To introduce the phenomena that will be encountered, an example is given here first. Figure 6.1 shows the instantaneous pressure contours and streamlines, for a Mach number from 0.60 to 0.75 at zero angle of attack. The effect on the aerodynamic coefficients can be found in Figure 6.1a. The following observations can be been made from Figure 6.1b-e when sequentially exploring the effect of and increasing Mach number:

- **Mach number $M_\infty = 0.60$:** The flow remains entirely within the subsonic regime. Lift has been steadily increasing due to compressibility. While it is less clear from the figure, a similar increasing trend is also true for the drag coefficient C_d. Compressibility corrections (refer to Section 2.2) have been developed to predict these trends. Their ability to predict the pressure coefficient for increasing Mach number will be assessed is Section 6.1.
- **Mach number $M_\infty = 0.65$:** Increasing the Mach number has resulted in the emergence of a shock-wave, characterized by the discontinuity observed in the pressure field. In contrast, the streamlines remain largely unchanged in comparison to those depicted in Figure 6.1b. The flow remains attached to the upper side of the airfoil, preserving the lifting capabilities to a great extent. The drag coefficient rises substantially as a result of the drag induced by the shock-wave, which is referred to as *wave drag* (a component of pressure drag).
- **Mach number $M_\infty = 0.70$:** The adverse pressure gradient associated with the wave has reached sufficient magnitude to cause shock-induced separation. Pressure fluctuations in the separated flow region cause the flow to become unsteady, marking the onset of *transonic buffet*. The shock will periodically travel up- and downstream, causing the boundary layer to separate and subsequently reattach. Naturally, this induces fluctuations of the aerodynamic coefficients as well. Looking at the mean quantities; lift experiences a significant decline, while drag continues to increase. Transonic buffet and its implications will be explained in more detail in Section 6.2.
- **Mach number $M_\infty = 0.75$:** A shock wave now also terminates on the airfoil's pressure side, resulting in phase-locked shock oscillations where the positions of the upper and lower shocks exhibit a 180° phase shift. Flow separation and wave drag continue to degrade lifting capabilities and increase drag.

Upon further increasing the Mach number to $M_\infty = 0.80$, the flow will no longer be able to reattach, marking the buffet offset Mach number. Consequently, the flow field will return to a steady state.

Further examination of the phenomena that have now been identified will follow in the upcoming sections.

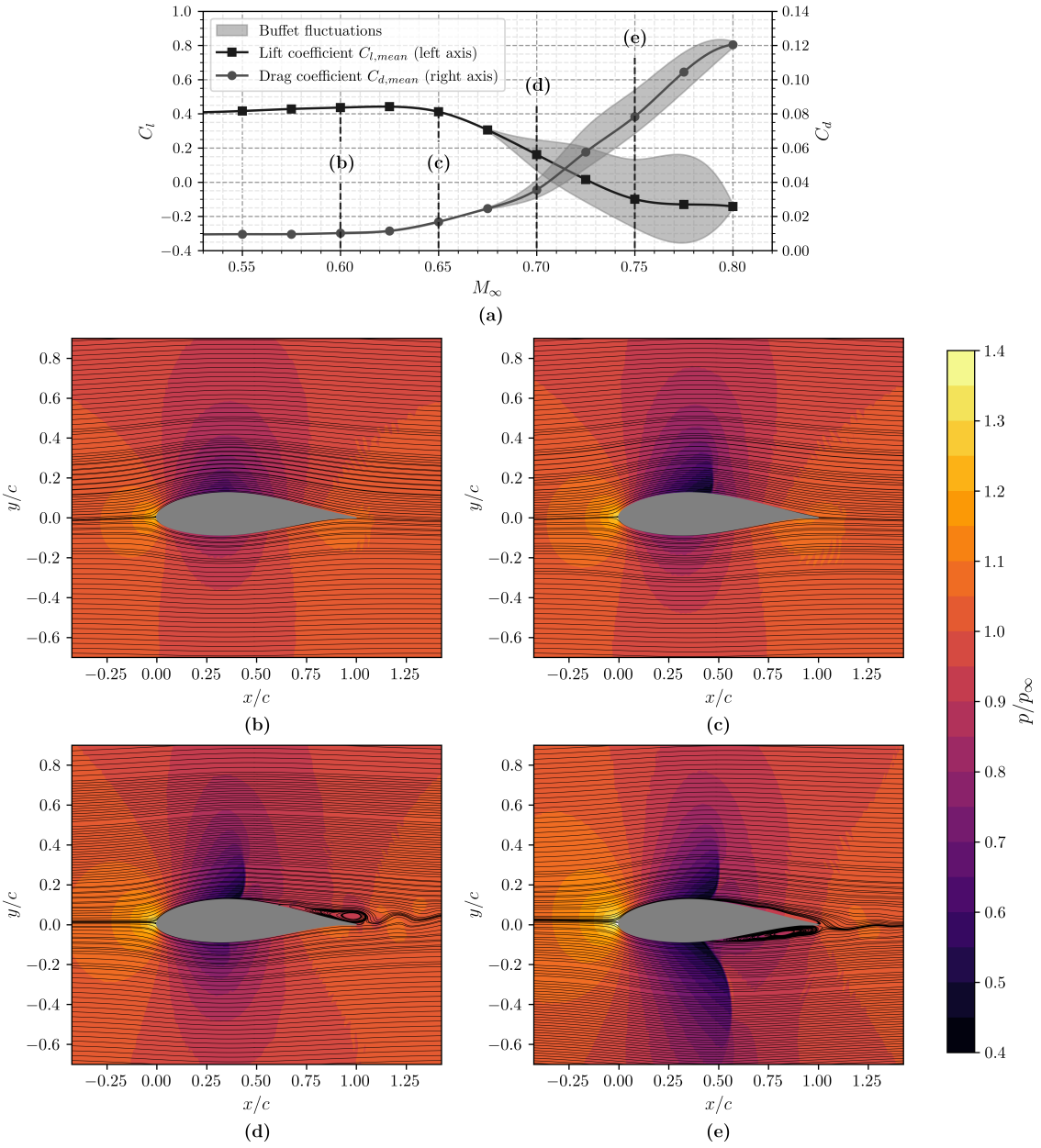

Figure 6.1: Influence of Mach number M_∞ on the flow field: **(a)** shows the effect on drag coefficient C_d, whereas **(b)** - **(e)** show the pressure field and streamlines for Mach numbers $M_\infty = \{0.60, 0.65, 0.70, 0.75\}$ at $Re_c = 18.0 \times 10^6$ and $\alpha = 0°$.

6.1. (Sub)critical Compressibility

Research question **Q-1-1** is concerned with the adequacy of the compressibility corrections given by Equations (2.7), (2.10) and (2.11) in Section 2.2. A main feature of the compressibility corrections lies in their predictive ability to determine the free stream Mach number at which the local Mach reaches one, referred to as the critical Mach number M_{crit}. Surpassing this threshold Mach number marks the onset of local supersonic flow. Hence, the critical Mach number is defined as the free stream Mach number at which the minimum pressure coefficient $C_{p,min}$, equals the critical pressure coefficient, $C_{p,crit}$. The critical pressure coefficient can be calculated using Equation (2.16), derived from the isentropic relations. The intersection of this equation with the compressibility corrections can serve as a predictor for M_{crit}.

The curves corresponding to the three aforementioned corrections are calculated from reference Mach number $M_\infty = 0.2$. These are plotted in Figure 6.2, along with the minimum pressure coefficients $C_{p,min}$, as obtained from the URANS simulations. The data points for which shock waves have been recorded are indicated here as well.

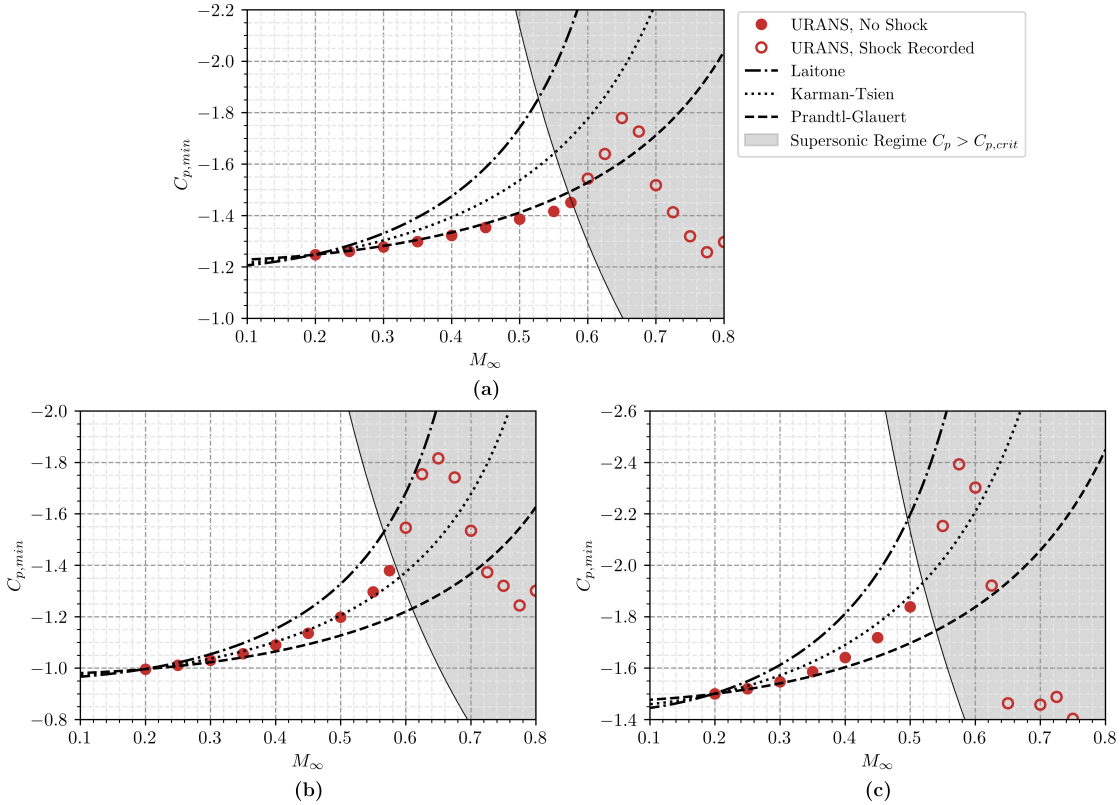

Figure 6.2: Comparison of minimal pressure coefficient $C_{p,min}$ from the compressibility corrections and the URANS simulations at $\alpha = \{-5°, 0°, 5°\}$ from **(a)-(c)** respectively at $Re_c = 18.0 \times 10^6$. The supersonic regime is derived from Equation (2.16).

It can be observed from Figure 6.2 that none of the corrections consistently outperforms the others across the evaluated angles of attack. The Prandtl-Glauert correction emerges as the most accurate in predicting the critical pressure coefficient at an angle of attack of $\alpha = -5°$. In contrast, the von Karman-Tsien correction provides preferable estimates at higher angles of attack. This observation also holds for the results at angles of attack at $-2.5°$ and $2.5°$, which are not included in Figure 6.2.

The Prandtl-Glauert rule allows for direct application of compressibility corrections to lift and drag coefficients according to Equations (2.8) and (2.9). This direct approach is not valid for the Karman-Tsien and Laitone corrections due to the non-linear terms of these equations. Nevertheless, they can be applied by first correcting the pressure coefficient and subsequently numerically integrating the corrected pressure coefficient over the airfoil surface to finally obtain the coefficients. It's important to note that this method does not account for the viscous components of lift and drag, aligning with the assumption of inviscid flow inherent to the corrections.

Given the significant impact of viscous forces on drag, our focus will shift towards evaluating the accurateness of the corrections applied to the lift coefficient. Figure 6.2 shows the lift coefficient as calculated by the URANS simulations, along with the predications obtained from the corrections. To obtain the lift coefficients, as predicted by the three corrections, the following steps are taken:

1. The pressure coefficient is transformed to its incompressible counterpart $C_{p,inc}$ from the pressure coefficient that has been obtained at $M_\infty = 0.20$.
2. The corrections are applied to the established Cp, inc, which yield a set of pressure coefficients for the full Mach number range.

3. The pressure coefficients are numerically integrated over the airfoil surface (in normal direction) to obtain the inviscid lift coefficient $C_{l,inv}$.

The findings reaffirm that the Prandtl-Glauert rule is most effective for an angle of attack of $-5°$, whereas the von Karman-Tsien correction shows better agreement for $\alpha = 0°$ and $\alpha = 5°$. Interesting to note, is that the corrections continue to be valid slightly beyond the critical Mach number. The extent to which they remain valid is heavily influenced by the onset of shock-induced separation. At higher angles of attack, this separation tends to occur shortly after exceeding the critical Mach number. However, for angles of attack at zero or negative values, it's observed that the lift estimates remain fairly accurate for Mach numbers up to 0.075 beyond the critical Mach number.

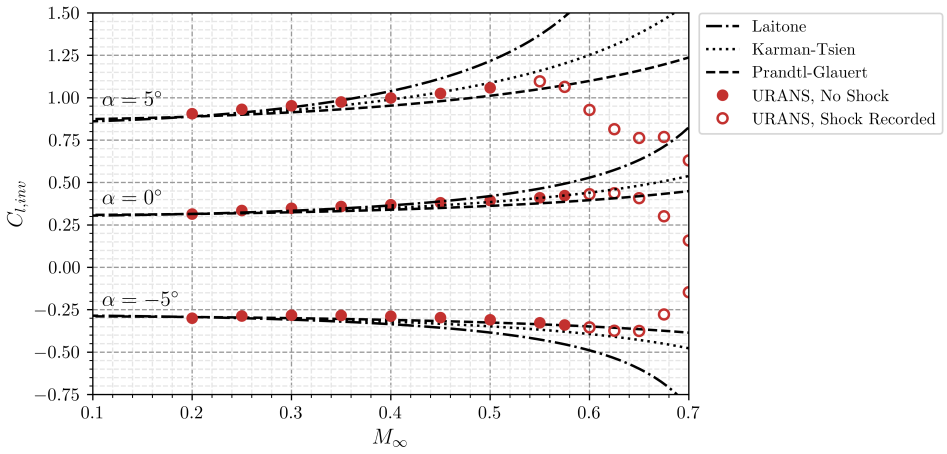

Figure 6.3: Comparison of inviscid lift coefficient $C_{l,inv}$ from the compressibility corrections and the URANS simulations at $\alpha = \{-5°, 0°, 5°\}$ and $Re_c = 18.0 \times 10^6$.

6.2. Transonic Flow & Buffet

The approximate boundary for the onset of local supersonic flow is shown in Figure 6.4b. With a further increment in free stream Mach number, as has been shown in Figure 6.1, the lower boundary of transonic buffet is reached. Additionally, the figure shows the regions where shockwaves have been detected either on the pressure side, the suction side, or on both. Figure 6.4a gives the amplitude of the

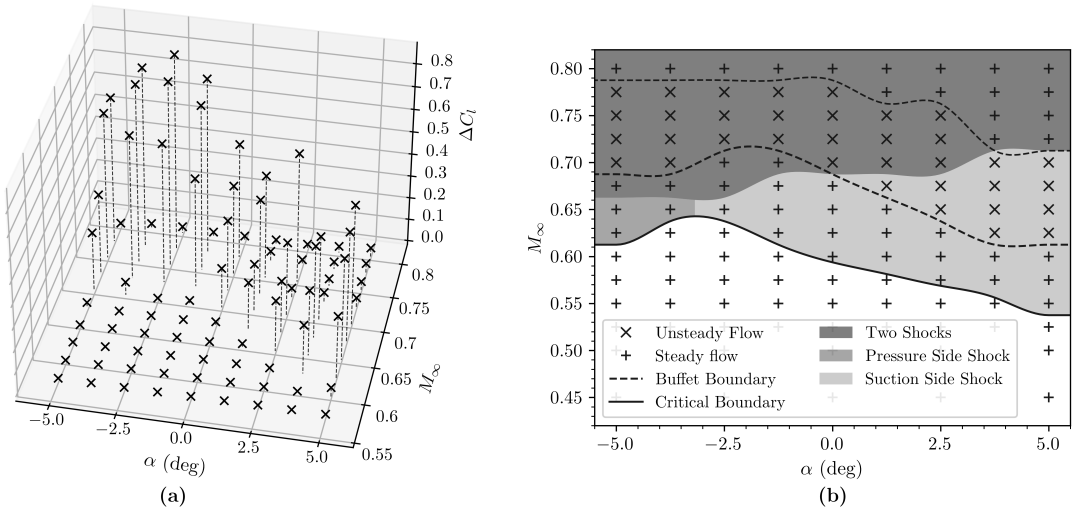

Figure 6.4: Buffet fluctuations for lift coefficient C_l **(a)** and estimated critical and buffet boundary **(b)** for NACA 63(4)-421 airfoil at $Re_c = 18.0 \times 10^6$.

lift coefficient fluctuations. Comparing this with 6.4b, it is observed that the highest amplitude for C_l is found in the lower angle of attack region, where a shock is present on both the suction and pressure side of the airfoil.

As has been described in 2.3.1, buffet can be subdivided into two main types, where Type I is characterized by an oscillating shock wave on both the suction and pressure side. The shocks produce a self-sustained oscillatory motion, where the shock strength and position vary with a 180° phase shift. Type II buffeting is characterized by an oscillating shock wave on the airfoils suction side. Both types of buffeting have been encountered in the URANS simulations.

Firstly, Figure 6.5 shows the buffet cycle for type 2 buffet at a Mach number $M_\infty = 0.65$ and angle of attack $\alpha = 0.65$. The time signal of the aerodynamic coefficients are shown in Figure 6.5a where the marked time instants correspond with numerical Schlieren ($\nabla\rho$) images of subfigures (b)-(g). The

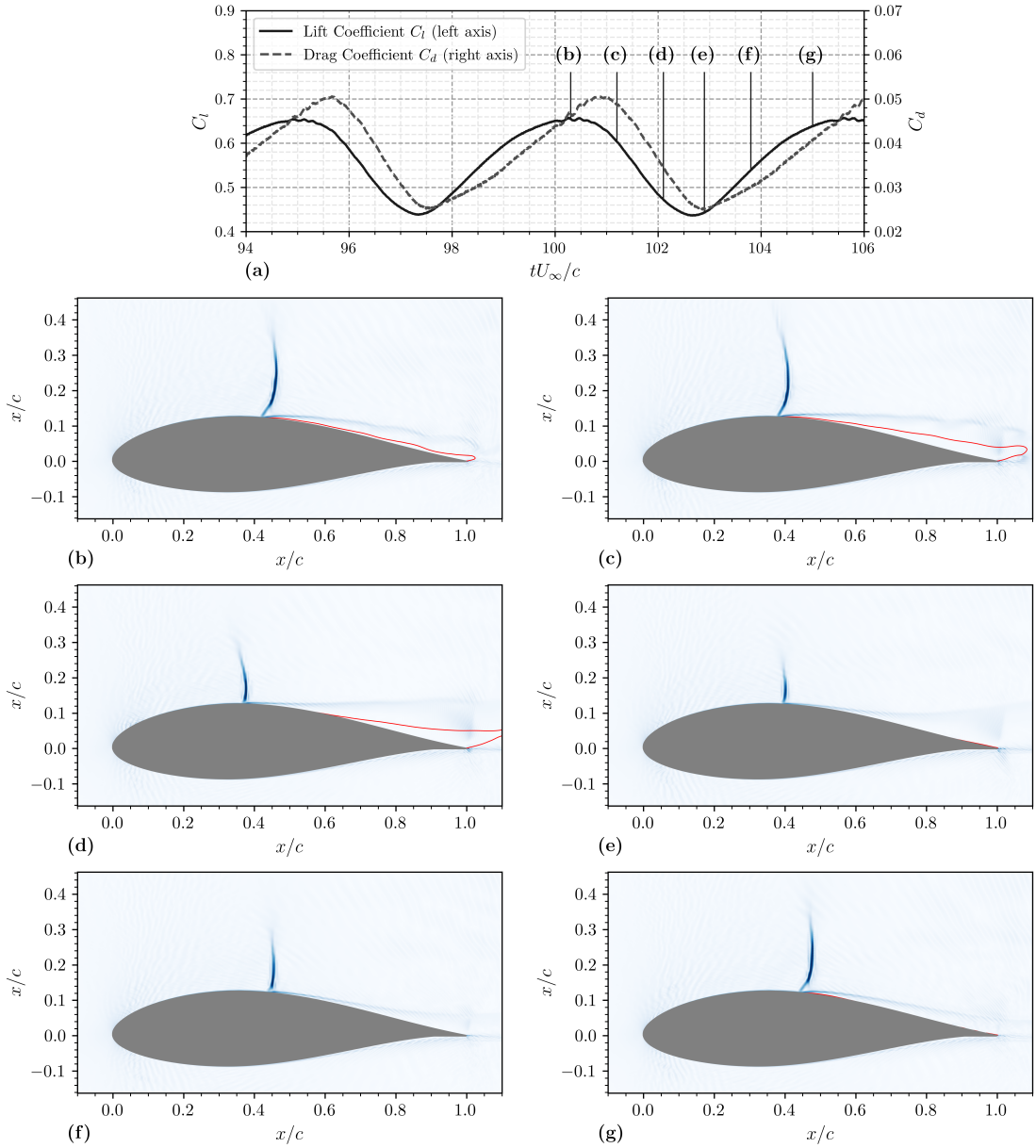

Figure 6.5: Buffet cycle of the NACA 63(4)-421 airfoil. Fluctuations of the aerodynamic coefficients are shown in **(a)**, whereas **(b)** - **(g)** provide numerical Schlieren ($\nabla\rho$) images with red lines marking the $u_1 = 0$ contour. $M_\infty = 0.65$, $Re_c = 18 \times 10^6$ and $\alpha = 2.5°$

red lines represent the contour where the velocity component in x-direction equals zero, marking the centerline of the recirculation zone.

Starting from Figure 6.5b, the boundary layer undergoes separation while the shock travels upstream. Conversely, during the downstream motion the shock weakens, while the boundary layer reattaches starting from the shock foot. Finally, as depicted in Figure 6.5g, the formation of the separation bubble is once again evident at the shock's foot. The numerical Schlieren images from Figure 6.5 do not explicitly illustrate the mechanism of the shock-induced boundary layer separation, which unfolds as follows: Initially, the separation bubble develops at the shock foot. In addition, the strong adverse pressure gradient induced by the shock results in thickening of the boundary layer, leading to flow separation at the trailing edge as well. Subsequently, the separation bubble grows downstream while the trailing edge separation expands upstream until collision, followed by full separation downstream of the shock.

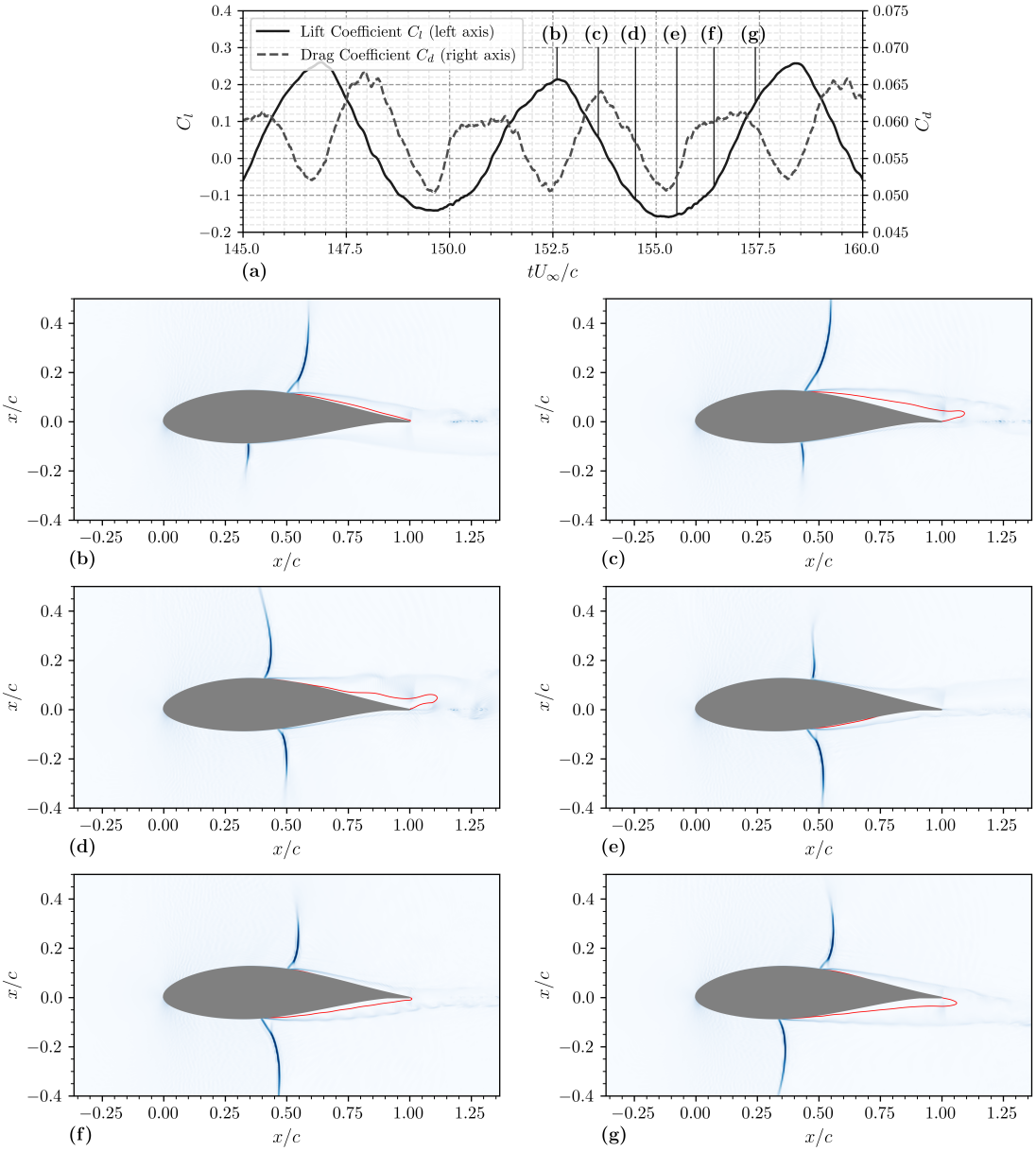

Figure 6.6: Buffet cycle of the NACA 63(4)-421 airfoil. Fluctuations of the aerodynamic coefficients are shown in **(a)**, whereas **(b)** - **(g)** provide numerical Schlieren ($\nabla\rho$) images with red lines marking the $u_1 = 0$ contour. $M_\infty = 0.725$, $Re_c = 18 \times 10^6$ and $\alpha = -1.25^\circ$

This observation aligns with Model B of the first kind shock-induced boundary layer separation, as described by Lachmann and Pearcy [7] (refer to Section 2.3.1, Figure 2.5). The reduced frequency of the oscillations was found as $k_r \approx 0.76$.

In the regime where shocks are found on both suction and pressure side, the observed fluctuations of the lift coefficient increase compared to a suction side shock only. Furthermore, the characteristics of the cycle change significantly. Figure 6.6 shows the cycle for Mach number $M_\infty = 0.725$ at an angle of attack α of -1.25°. Firstly, looking at the temporal evolution of the aerodynamic coefficients, the drag coefficient exhibits fluctuations at twice the frequency of those in the lift coefficient. This behavior is in accordance with Type I buffet, also observed by Zhang et al. [73] for a biconvex airfoil.

Moreover, the numerical Schlieren images ($\nabla\rho$) reveal 180° phase locked oscillations of the upper and lower shock. Starting from Figure 6.6b, we observe the expansion of the recirculation region on the suction side as the shock moves upstream, while the pressure side shock travels downstream. Subsequently, flow reattaches on the suction side, whereas the separation bubble grows on the pressure side, followed by a full separation downstream of the pressure side shock. Eventually, the flow reattaches during the upstream motion and the cycle repeats. The reduced frequency of the lift coefficient fluctuations (full buffet cycle) was found as $k_r \approx 0.64$.

In contrast to the buffet cycle from Figure 6.5, flow separation is induced by rearward growth of the recirculation bubble exclusively, classified as Model A separation by Lachmann and Pearcy [7]. On the suction side, the adverse pressure gradient is comparatively lower, attributed to the reduced angle of attack. Hence, the separation mechanism in the buffet region varies for different angles of attack. For the pressure side, model A (rearward growth of bubble) separation has been found exclusively, regardless of angle of attack or Mach number, resulting from the airfoil's curvature near the trailing edge.

It is important to clarify that the onset of shocks on both the suction and pressure sides does not inherently guarantee oscillatory behavior of the shock on the suction side. The boundary illustrated in Figure 6.4b between the "Two Shocks" and "Suction Side Shock" regimes, merely signifies the presence of a shock on the suction side. This does not necessarily imply that the shock has sufficient strength to induce separation. In this case, the characteristics of the buffet cycle would have similar oscillations as depicted in Figure 6.5 (Type II). Furthermore, no instances have been found in the simulations where the shock weakens to the point of disappearing; i.e., degenerating in weak compression waves.

6.3. Polars

Figure 6.7 shows the interpolated mean aerodynamic coefficients as field values for free stream Mach number M_∞ and angle of attack α. The figure includes projections on the (x, z)- and (y, z)-planes

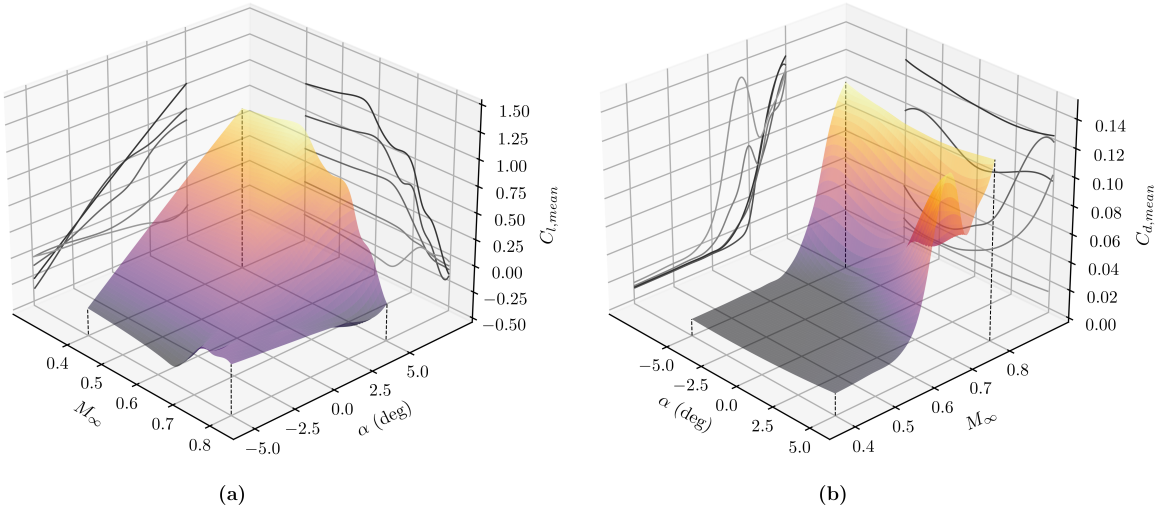

(a) (b)

Figure 6.7: Calculated (URANS) field for mean lift coefficient $C_{l,mean}$ **(a)** and drag coefficient $C_{d,mean}$ **(b)** at $Re_c = 18.0 \times 10^6$. Contour projections are shown for sets $M_\infty = \{0.4, 0.65, 0.7, 0.75, 0.8\}$ and $\alpha = \{-5°, -2.5°, 0°, 2.5°, 5°\}$

.

showing the contour lines for sets $M_\infty = \{0.4, 0.65, 0.7, 0.75, 0.8\}$ and $\alpha = \{-5°, -2.5°, 0°, 2.5°, 5°\}$. The darkest lines indicate the contours closest to the coefficient planes. Note that the α- and M_∞-axis are interchanged between the two subfigures to enhance visibility. The polars that are presented here, will be used for the lifting line method described in Part III of this work.

For the mean lift coefficient $C_{l,mean}$ in Figure 6.7a, the polar remains linear for the lower free stream Mach numbers. The linearity disappears as the Mach number increases, first observed at the higher angles of attack. Further increasing the mach number leads to severe degradation of lift as a result of shock-stall. Ultimately, the mean lift coefficient drops to subzero values across the entire polar range.

As expected, the mean drag coefficient $C_{d,mean}$ shows to be rapidly increasing as the drag divergence Mach number M_{DD} is surpassed. For the lower angles of attack ($\alpha < 2.5°$), the curve continuously increases. Conversely, at higher angles of attack, a peak is observed within the buffet regime. In this regime, the upstream position of the shock is located very close to the leading edge, inducing a large separation zone. The associated maximum drag exerts a substantial influence on the mean drag. It is worth noting that this peak has not been reported in prior studies, which introduces some uncertainty regarding its accuracy.

6.3.1. Stall

As has been explained in section 4.6, stall and post-stall flow conditions are anticipated in the rotor's root region. To ensure continuity for the polars utilized in the lifting line method (refer to Part III), simulations in the stall region have been conducted at a free stream Mach number of $M_\infty = 0.20$. Figure 6.8 presents the resulting lift and drag polar for an angle of attack extending from $-7.5°$ to $20°$. It is observed that $C_{l,max}$ is found at $\alpha = 14°$, that is, the maximum lift coefficient at stall conditions. Further increment of angle of attack initially leads to a slight decline of the lift coefficient. Subsequently, lift Recovery is observed starting from $\alpha = 18°$.

In the absence of experimental data for the NACA 63(4)-421 airfoil in conditions of a fully turbulent boundary layer under stall, the results cannot be validated. The xFoil results [68] for a forced transition at $x/c = 0.02$ are shown in Figure 6.8 as well. The predictions show proper agreement in the linear portion of the polar. However, xFoil's capabilities are restricted to scenarios with limited separation regions only, and accuracy greatly diminishes when approaching $C_{l,max}$.

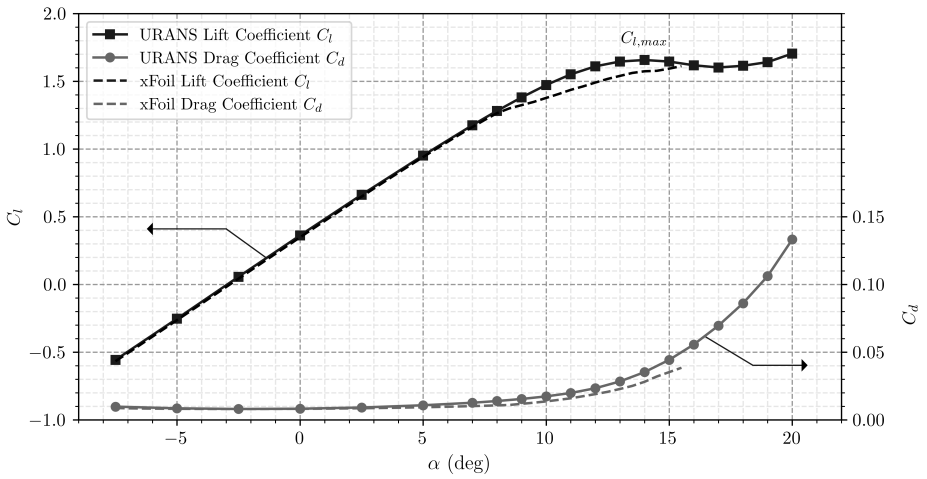

Figure 6.8: Lift and drag polar for the NACA63(4)-421 airfoil including stall region. $M_\infty = 0.20$ and $Re_c = 18.0 \times 10^6$

Therefore, examining the flow field provides a more insightful evaluation of the accuracy of stall behavior. Airfoils are often subdivided in either "thin" or "thick" according to their stall characteristics. These include trailing edge stall, leading edge stall, and thin airfoil stall. Given that the NACA 63(4)-421 airfoil can be classified as a "thick" airfoil, trailing edge stall is anticipated. Figure 6.9 shows the pressure field and streamlines for angles of attack $\alpha = 16°$ and $\alpha = 20°$. Consistent with expectations, the flow separation is observed to initiate at the trailing edge and progressively extends upstream as the angle of attack increases. These characteristics align with the trend seen in the polar from Figure 6.8, where the lift coefficient gradually declines post-stall. In contrast, leading edge stall would be characterized by an

abrupt decline in lift just passed $C_{l,max}$.

As previously stated in Section 4.8, the angle of attack in the root region will exceed the values that have been simulated. This will be addressed through post-stall extrapolation, further explained in Section 7.2.2.

In conclusion, the URANS simulations are consistent with the anticipated behavior of the NACA 63(4)-421 airfoil at stall conditions, though the findings lack validation. It's important to note the inherent limitations of RANS methods in accurately predicting highly separated flow regions. Large Eddy Simulations (LES) or hybrid methods usually provide better results.

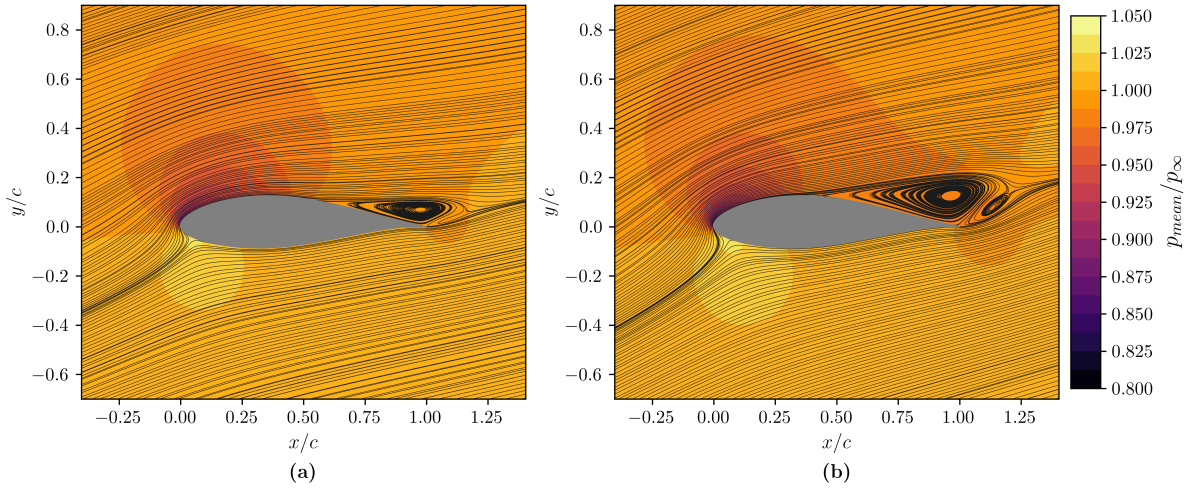

Figure 6.9: Mean pressure field and streamlines for the NACA 63(4)-421 airfoil in stall region at $\alpha = 16°$ **(a)** and $\alpha = 20°$ **(b)**. $M_\infty = 0.20$ and $Re_c = 18.0 \times 10^6$

6.4. Discussion

This part of the research addresses the characteristics of the "thick" NACA 63(4)-421 airfoil when subjected to high subsonic and transonic Mach numbers. Central to this investigation is the exploration of aerodynamic behavior under various conditions, including the onset of shocked flow and transonic buffet, their corresponding influence on loads, and the suitability of existing corrections for incompressible aerodynamic coefficients in the subcritical compressible regime.

To commence with the evaluation of the compressibility corrections, the results did not reveal a unanimously superior correction among Prandtl-Glauert [13], Karman-Tsien [15], and Laitone [16]. The Prandtl-Glauert rule most accurately predicted the critical Mach number at the lowest examined angle of attack of $-5°$, whereas Karman-Tsien provided more accurate estimates for angles of attack of $\alpha \geq -2.5°$). Furthermore, predictions of the lift coefficient by correcting for the pressure coefficient showed similar trends. Supporting literature, including Bonilla et al. [19] and Wang et al. [20], presented varying views as well: while the former found superior accuracy of the Prandtl-Glauert rule in predicting the critical Mach number, the latter indicates that none of the corrections provided satisfactory approximations. Therefore, it was hypothesized that the adequateness is highly dependent on applications, which the obtained results support. This study has been limited to a single airfoil, and broad generalizations about "thick" airfoils should therefor be approached with caution. In summary, the findings of this work show a clear preference for the Karman-Tsien rule. Nevertheless, given that the Prandtl-Glauert rule also delivers reasonably satisfactory outcomes, coupled with its documented effectiveness in prior studies and inherent simplicity (directly applicable to the aerodynamic coefficients), it also presents itself as a viable option.

Moreover, this study has successfully identified the boundary for the critical and buffet regime, and the resulting loads on the NACA 63(4)-421 profile within these domains. The transition into the critical regime rapidly triggers shock-induced separation, leading to the onset of transonic buffet. This aligns with expectations, as the pronounced curvature of the airfoil implies a greater susceptibility to separation in comparison with supercritical airfoils, which have been the primary subject of previous research.

The results have provided the first identification of the buffet characteristics specific to a "thick" profile. In previous studies, buffet has been categorized into two main types, where type I was confined to biconvex (symmetrical) airfoils. However, this study has identified type I buffet cycles on the non-symmetrical NACA 63(4)-421 airfoil, with the shock-induced separation mechanism exclusively attributed to the rearward growth of the bubble (Model A separation). Furthermore, for the higher angles of attack, type II buffet has been found, which has mostly been studied in the context of supercritical airfoils. Here, the shock-induced separation emerges from both the bubble and trailing edge separation (Model B). In essence, this study provides valuable initial insights into the susceptibility of "thick" airfoils to buffet and the consequential impact on aerodynamic coefficients.

On a more critical note, the effectiveness of URANS at predicting transonic buffet should be approached with some caution. While studies like those conducted by Concalves and Houdeville [48] have demonstrated its effectiveness in predicting frequency and amplitude, URANS tends to have limitations in accurately capturing large regions of separated flow. In the context of the thick airfoil addressed in the present study, such separated regions are notably larger compared to supercritical airfoils (which form the primary profiles of interest for prior studies). Research by Fukushima and Kawai [74], as well as Memmolo [75], indicates that despite the ability of URANS to successfully predict the buffet frequencies, the load amplitudes were more accurately reproduced through higher fidelity methods, such as (Wall-Modelled) LES or hybrid methods.

Furthermore, it should be noted that a fundamental assumption has been the implementation of wall functions and a single chord-based Reynolds number of $Re_c = 18.0 \times 10^6$ throughout all simulations. This approach inherently assumes a fully turbulent boundary layer. As has been shown by Moise et al. [76], tripped boundary layers yield significant buffet, whereas only weak shock oscillations are found for transitional flows. Despite this, the assumption of a turbulent boundary layer could be considered justifiable in the context of wind turbines. Over time, contamination of the leading edge due to environmental conditions roughen the blade surface [77]. Given a rougher surface, in combination with the high operational Mach numbers examined in this study, the boundary layer in the rotor tip areas will likely be forced to turbulent near the leading edge.

Lastly, some remarks can be given regarding the implications of the current findings to Part III of this work, where a full rotor will be simulated through implementation of a lifting line model. Here, it will be assessed whether shock-stall can be used as an overspeed protection mechanism for an unloaded rotor. As stated before, Wood [6] has previously tested this hypothesis for a small (< 3 kW) turbine with a uniform airfoil (NACA 0012) throughout the blade. His findings indicated that drag-divergence occurred too slowly to prevent overspeeding. The NACA 63(4)-421 profile that has been studied here, shows to have a considerably lower drag divergence Mach number, suggesting potential differences in the effectiveness of shock-stall for overspeed protection.

Furthermore, the onset of buffet occurs rapidly past drag divergence and the associated load fluctuations are so pronounced they cannot be disregarded. Accurately capturing the buffet phenomenon for a wind turbine, and particularly for a tilted turbine with varying Mach number for each azimuthal angle, would necessitate comprehensive approaches such as experimental studies or full three-dimensional CFD simulations, which is past the scope of the current study. Nevertheless, some implications can be given using the obtained reduced frequencies and load fluctuations.

Part III

LIFTING LINE

7

Lifting Line: Methodology

This chapter addresses the approach regarding the lifting line model. Firstly, the computational approach will be given in Section 7.1. This section not only lays out the mathematical background essential for formulating the problem, but also details the integration into the company's in-house lifting line code that will be utilized for the rotor analysis of this study. Additionally, this section discusses the key settings of the solver that have significant impact on the solution.

Subsequently, Section 7.2 presents the definition of the rotor to be analyzed. Given the absence of a finalized design for a large-scale rotor by the company, the existing 6 m diameter prototype rotor will be upscaled to match the specifications of a $3MW$ turbine. Furthermore, this section addresses the implementation of the polars derived in Part II, as well as the extrapolation method of these polars into the post-stall regime.

Finally, the operational conditions to be simulated for the rotor are detailed in Section 7.2.3. Storm scenarios dictate the emphasis of these conditions, since the objective of this study is to assess the rotor's performance as shocks emerge in the blade tip region.

7.1. Computational Approach

The lifting line method is a numerical technique employed to compute the forces exerted on a blade and the flow field at any given point in space. This model adopts a blade element approach; i.e., the blade is discretized into segments along its span. Within each segment, loads are calculated based on the local velocity at a specified *control point*. The velocity at the control point is ascertained through potential flow theory, which will be briefly explained first in Section 7.1.1. This involves the superposition of the undisturbed wind field and the velocity field emerging from the vorticity distribution along the blade. This vorticity distribution, in turn, is a consequence of the blade's loading.

For the implementation of the lifting line method in this study, the company's in-house (free wake) lifting line code will be used. A schematic representation of the model's workflow is provided in Figure 7.1. The process commences with the setup of the rotor geometry, derived from the rotor specifications outlined in Section 7.2. Additionally, the operational conditions to which the rotor will be subjected are specified, as detailed in Section 7.2.3.

Potential flow problems are described by superposition of *perturbation elements*. In the context of a lifting line model, the *vortex filament* serves as the selected perturbation element. A sequence of these vortex filaments can effectively represent a rotor blade, as will be explained in Section 7.1.2. After the geometry is discretized into this set of vortex filaments, blade velocities are computed based on the induced velocities from the bound and wake vortices. These can be calculated from the Biot-Savart law elaborated in Section 7.1.3. Once the velocities at the control points are established, the angles of attack at the control points can be calculated. Since the vorticity distribution is a consequence of the blade loading, it cannot be calculated directly; instead, an iterative approach is employed to find the correct distribution. The procedure is explained in Section 7.1.5. Upon convergence of the solution, the

instantaneous forces acting on the individual blade segments can be calculated as (refer to Figure 3.3),

$$F_t = F_l \sin\Phi - F_d \cos\Phi \tag{7.1}$$

$$F_n = F_l \cos\Phi + F_d \sin\Phi \tag{7.2}$$

Subsequently, the bound vorticity is shed into the wake, and the model advances to the next time step. The time-loop continues until the predefined number of blade rotations is achieved. It is determined that following 6 complete rotations, the wake is fully developed, and the periodic forces exhibit negligible variation, prompting the code to exit the time-loop. As a final post-processing step, calculations for rotor thrust and power, along with their respective coefficients, are performed. This involves averaging the forces across a full rotation. The coefficients provide information about the rotor's aerodynamic efficiency, and are given by,

$$C_P = \frac{P}{\frac{1}{2}\rho U_0^3 \pi R^2}\,; \quad C_T = \frac{T}{\frac{1}{2}\rho U_0^2 \pi R^2}\,, \tag{7.3}$$

The code also incorporates additional functions like Snel's dynamic stall model, Himmelskamp effect, and modelling for ground effects. However, within the context of this study, these functions have been omitted to isolate the effects of shock-stall phenomena on rotor performance.

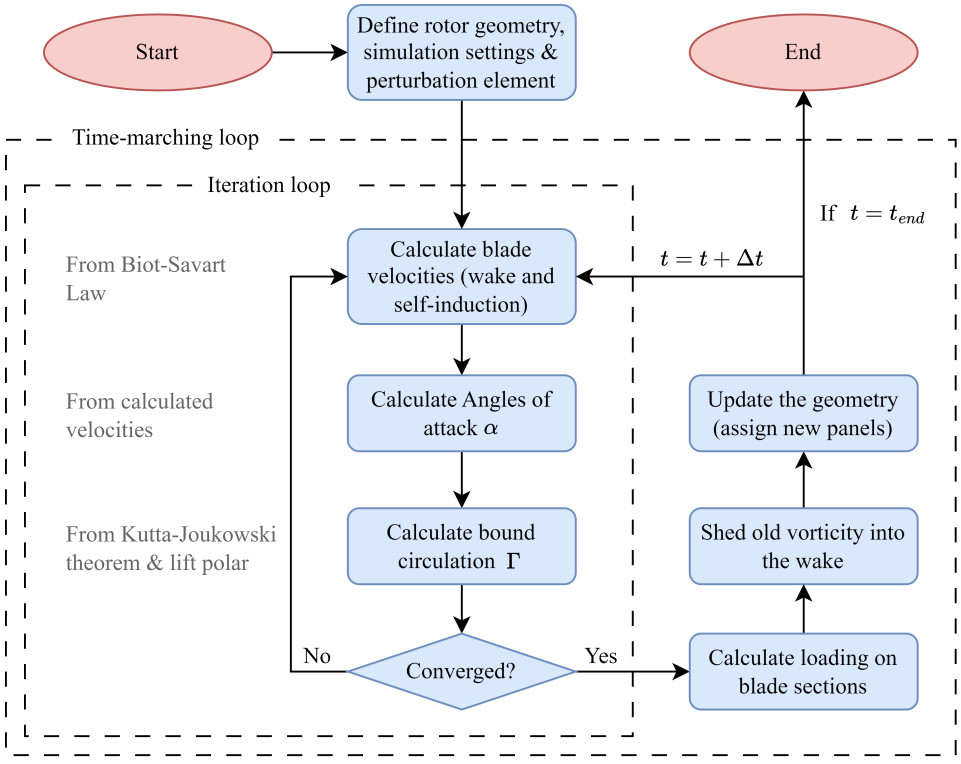

Figure 7.1: Flow chart of the in-house lifting line code.

7.1.1. Potential Flow

Like the Favre-Averaged Navier-Stokes formulation outlined in Section 4.1, the foundation of potential flow theory originates from the Navier-Stokes equations (Equations (4.1) - (4.3)). The distinction arises from the number of assumptions made. Referring to Figure 4.1, compressibility, friction, and heat transfer are neglected. This simplifies the continuity equation to the following:

$$\nabla \cdot \mathbf{u} = 0\,, \tag{7.4}$$

Similarly, the momentum equation from (4.2) reduces to,

$$\frac{\partial \mathbf{u}}{\partial t} + (\mathbf{u}\cdot\nabla)\mathbf{u} + \nabla\frac{p}{\rho} = 0\,, \tag{7.5}$$

Equations (7.4) and (7.5) are commonly referred to as the *Euler equations*. Furthermore, potential flow theory assumes the flow to be irrotational; i.e., the curl of the velocity vector equals the null vector. Consequently, the velocity can be represented as the gradient of a scalar potential Φ, so that,

$$\nabla\Phi = \mathbf{u}\,, \tag{7.6}$$

Now, when Equation (7.6) is substituted into the expression for continuity from (7.4), the Laplace equation is obtained,

$$\nabla^2\Phi = 0\,, \tag{7.7}$$

Equation (7.7) describes a partial differential equation, which can be solved given a set of boundary conditions. Important to note, is the linear nature of the Laplace equation, which means the principle of superposition holds: The sum of two or more individual solutions also constitutes a valid solution. Once a solution is found for the velocity field, each field value can be related to the local pressure through the use of Equation (7.5).

In summary, singular solutions to the Laplace equation can be superimposed to define a flow field. These solutions are often referred to as *perturbation elements*. For the lifting line method, the selected perturbation element is the vortex filament, explained in Section 7.1.2. For a general comprehension of this concept, A brief description of the fundamental solutions for 2D flow is given here first, according to the work of Katz and Plotkin [78].

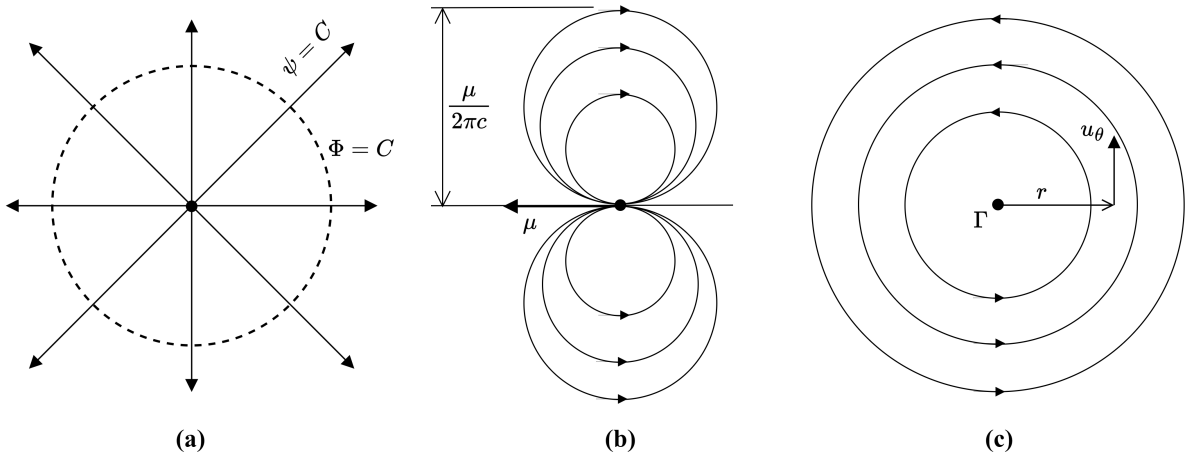

Figure 7.2: Basic singular solutions to the Laplace equation: **(a)** source/ sink, **(b)** doublet and **(c)** vortex. Sketches are based on the work of Katz and Plotkin [78].

Source/ Sink

A source is characterized as a point from which flow propagates uniformly in all directions, as depicted in Figure 7.2a. The potential generated by such an element, in spherical coordinates, is represented by:

$$\Phi = -\frac{\sigma}{4\pi r}\,, \tag{7.8}$$

Here, σ denotes the strength of the source, while r is the radial distance from the source itself. Conversely, a sink is analogous to a source but with an inverse sign for the strength σ. Calculating the gradient of this potential results in the velocity field induced by the element:

Doublet

Secondly, a doublet represents a fundamental solution to the potential flow equations, described by a combination of source and sink positioned at an infinitesimally small distance from each other. The potential function associated with a doublet is formulated as:

$$\Phi = \frac{-\boldsymbol{\mu}\cdot\mathbf{r}}{4\pi r^3}\,, \tag{7.9}$$

where $\boldsymbol{\mu}$ represents the doublet strength and $\mathbf{r}$ denotes the distance from its core. The doublets orientation is defined by a vector, as depicted in Figure 7.2b.

Vortex

The third type of solution involves a point around which streamlines rotate, and the velocity diminishes with distance from that point. This is shown in Figure 7.2c. Mathematically, a two-dimensional vortex can be described by:

$$u_\theta = \frac{\Gamma}{2\pi r} \tag{7.10}$$

From the Kutta-Jouwkowski theorem, it is derived that circulation Γ is required for a body to generate lift. Hence, a vortex (distribution) can be used to describe the flow for a lifting airfoil. For the lifting line method, the vortex element is extended to a 3D element; the vortex filament.

The most important feature of potential flow, is the ability to solve the Laplace equation (7.7) through the superposition of singular solutions along the boundaries of the problem. These fundamental solutions intrinsically satisfy the boundary conditions. Subsequent sections will demonstrate how a solution can be formulated by extending the vortex solution described above to a three-dimensional framework. Note how this method differs from the URANS approach from Part II of this work. To obtain a result required calculating a solution for every cell within the domain. In contrast, potential flow modeling only requires solving for the boundary condition on the boundary surface itself.

7.1.2. Perturbation Element: Vortex Filament

The lifting line method solves the Laplace equation by discretizing the body as an array of vortex filaments, which collectively compose the lifting line. The force distribution across the blade's surface induces vorticity, which then propagates along the blade's surface and convects with the flow. The vorticity that adheres to the blade's surface is referred to as the *bound vorticity*, while the vortices that are convected with the flow compose the *wake vorticity*. A depiction of the wake's temporal development, based on the work of van Garrel [79], is provided in Figure 7.3.

The bound vortex is placed at $x/c = 0.25$. Furthermore, the boundary condition must be satisfied that there is no flow passing through the blade; A Neumann boundary condition that can be described in terms of potential by,

$$\nabla \left(\Phi + \Phi_\infty\right) \cdot \mathbf{n} = 0\,, \tag{7.11}$$

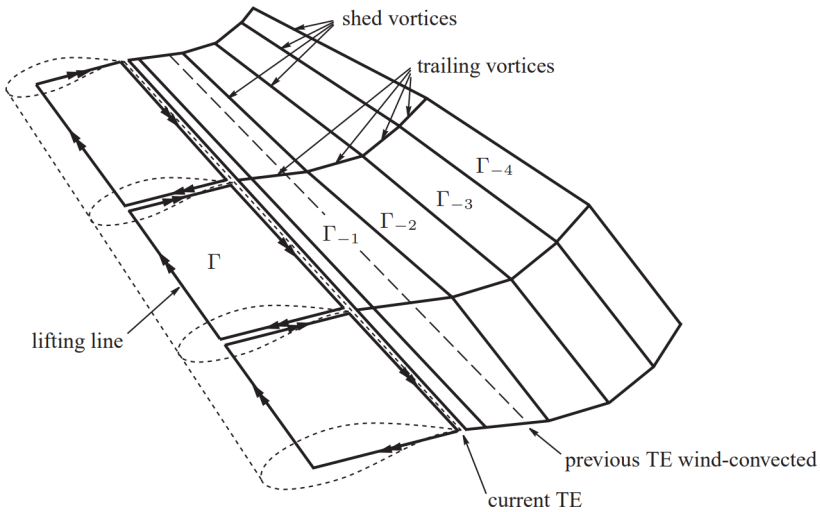

Figure 7.3: Sketch of the geometry of bound vortex filaments and shedded wake (adapted from van Garrel [79]).

This condition is enforced on the *collocation point*, placed at $x/c = 0.75$. This placement is strategic, ensuring the Kutta condition is satisfied. The Kutta condition is a fundamental principle in aerodynamics

that ensures a physically realistic and mathematically stable solution for the flow around an airfoil. It states that the flow must leave the trailing edge of an airfoil smoothly, without any abrupt changes in direction or velocity. This condition effectively dictates that the circulation around the airfoil is such that it counteracts the inherently sharp pressure gradient at the trailing edge. In the context of potential flow theory, it necessitates that the total circulation around the airfoil is set to a value that nullifies the velocity component perpendicular to the chord at the trailing edge, ensuring a streamlined flow off the airfoil.

Furthermore, some important principles hold for vortex filaments, since they must comply with Helmholtz's theorems. These are:

- The strength of a vortex line is constant along its length.
- A vortex line cannot end in a fluid; it must extend to the boundaries of the fluid or form a closed path.
- A fluid element that is initially irrotational remains irrotational.

Moreover, vortex filaments must also comply with Kelvin's theorem, which states that:

- The circulation around a closed curve (which encloses the same fluid elements) moving with the fluid remains constant with time.

Hence, the material derivative of circulation Γ with respect to t equals zero.

7.1.3. Calculation of Blade Velocities

The first step of the time loop shown in the Flowchart from Figure 7.1 is to calculate the perceived velocities for each blade section i. This is given by the following summation:

$$\mathbf{u}_{i,tot} = \mathbf{u}_{i,wake} + \mathbf{u}_{i,body} + \mathbf{u}_{i,rel} \,, \tag{7.12}$$

Here, $\mathbf{u}_{i,wake}$ and $\mathbf{u}_{i,body}$ denote the induced velocities from the wake and body at the control point of a panel, respectively. The relative velocity $\mathbf{u}_{i,rel}$ follows from the addition of geometric velocity components (refer to Figure 3.3).

The velocity that is induced by the vorticity can be calculated using the Biot-Savart law. This states that if the vorticity is concentrated on a curve from point a to b, having a uniform circulation Γ, the induced velocity u_i at point x_p by segment dl, can be calculated by the integral formulation given in Equation (7.13).

$$\mathbf{u}_i = \frac{\Gamma}{4\pi} \int_a^b \frac{\mathbf{dl} \times \mathbf{r}}{|r^3|} \,, \tag{7.13}$$

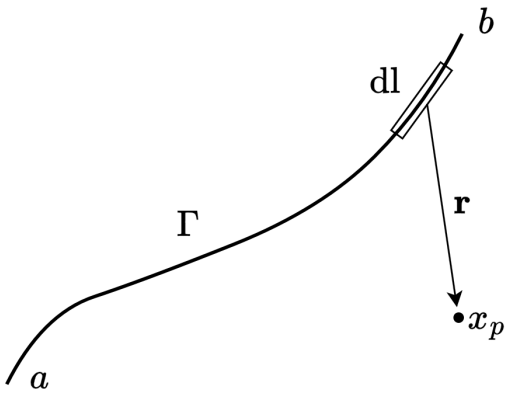

Figure 7.4: Nomenclature for Biot-Savart law from Equation 7.13.

If the vortex segments are straight, which is achieved trough discretization, the integral can be solved analytically and becomes a simple geometric relation. The discretization of the lifting line will be given in Section 7.2

7.1.4. Vortex Core Desingularization

The Biot-Savart law from Equation 7.13, exhibits a singularity at the vortex core where,

$$\lim_{\mathbf{r}\to 0} u_\theta = \infty \,, \tag{7.14}$$

indicating that the velocity induced by a vortex line approaches infinity at an infinitesimally small distance from the vortex line. To mitigate this singularity's impact on simulation stability and to more accurately represent the physical behavior of the viscous core of both bound and wake vortices, a model for the viscous vortex core has been implemented. The parameter r_c, denoting the vortex core radius, is introduced. This parameter delineates the region where viscous effects dominate the vortex behavior, ensuring that the induced velocity smoothly transitions towards zero as the core of the vortex is approached.

Numerous models are available, and for this work, the Lamb-Oseen vortex model has been selected. It is described in Lamb's publication [80] based on the early work of Oseen [81]. The function used for desingularization in this model is expressed as follows:

$$\bar{u}_\theta = \frac{1}{\bar{r}} \left(1 - e^{-1.2526\bar{r}^2}\right) \,, \tag{7.15}$$

In this context, the non-dimensionalized azimuthal velocity and core radius are defined as:

$$\bar{u}_\theta = \frac{u_\theta}{\Gamma_\infty/(2\pi r_c)} \,; \quad \bar{r} = \frac{r}{r_c} \,, \tag{7.16}$$

The radius of the vortex core is calculated using the expression:

$$r_c = \sqrt{r_0^2 + 4\alpha_L \nu \left(1 + a_1 Re_v\right) t} \,, \tag{7.17}$$

In this equation, r_c denotes the vortex core radius; r_0 represents the initial core radius, α_L is an empirical constant set to 1.25643, a_1 is another empirical constant valued at 6.5×10^5, and t represents the wake age. The vortex Reynolds number, Re_ν, is defined as the ratio of the vortex circulation strength and kinematic viscosity is denoted by ν. The initial core radius is determined by,

$$r_0 = \sqrt{4\delta_\nu \alpha_L \nu \left(t_0 + S\right)} \,, \tag{7.18}$$

where δ_ν represents the turbulent eddy viscosity which is in the order of $\mathcal{O}(10^1)$ for small rotors and from $\mathcal{O}(10^2)$ to $\mathcal{O}(10^3)$ for full-scale rotors, as suggested by Sant et al. [82]. The variable S in introduced to ensure the radius does not go to 0 at $t = 0$ s. Good results have been obtained by Balduzzi et al. [83] using $S = 0.0001$ s.

7.1.5. Iteration Loop for Bound Circulation

The calculation of the velocity at the control points from Section 7.1.3 marks the first step of the iteration loop from Figure 7.1 initiates. Subsequently, the angle of attack is calculated for each blade, which directly follows from the total velocity vector u_{tot}. Given that the bound circulation Γ is dependent on the blade loading, an iterative method, developed by van Garrel [79], is implemented. The required steps of this scheme are given below. Here, subscript i denotes the i-th panel, whereas j corresponds to the j-th iteration.

1. An initial guess is made for the section circulation strength $\Gamma_{i,j=0}$.
2. For each blade section, the total velocity $u_{tot,i}$ at the quarter-chord point is calculated, given by Equation (7.12).
3. For each blade section, the local angle of attack α_i is calculated at the control point from the velocity vector $\mathbf{u}_{rel}$.
4. The corresponding lift coefficients $C_{l,i}$ are obtained from the established data from Part II (Figure 6.7). For stall conditions near the root, the lift data from Section 7.2.2 is used.

5. For each blade section i, an additional guess for the bound circulation is established, denoted by Γ_{C_l}. This is calculated using the following relation:

$$\Gamma_{C_l,i} = C_l\left(\alpha_i\right) \frac{\frac{1}{2}\left(\left(\mathbf{u}_{tot,i}\cdot\mathbf{n}_{1,i}\right)^2 + \left(\mathbf{u}_{tot,i}\cdot\mathbf{n}_{2,i}\right)^2\right) dA}{\sqrt{\left(\left(\mathbf{u}_{tot,i}\times \mathrm{dl}\right)\cdot\mathbf{n}_{1,i}\right)^2 + \left(\left(\mathbf{u}_{tot,i}\times \mathrm{dl}\right)\cdot\mathbf{n}_{2,i}\right)^2}}\,, \tag{7.19}$$

   The establishment of Equation (7.19) is rooted in the principles of the Kutta-Joukowski theorem. The quantities $\mathbf{n}_1$ and $\mathbf{n}_2$ denote the unit vectors in chordwise and normal direction of panel i, respectively.
6. The difference between the newly established Γ_{C_l} and initial guess for bound circulation Γ_j is calculated.

$$\Delta\Gamma_i = \Gamma_{Cl,i} - \Gamma_{i,j}\,, \tag{7.20}$$

7. From the resulting difference in vortex strength $\Delta\Gamma$, an updated value for bound circulation Γ_j is calculated as,

$$\Gamma_{i,j} = \Gamma_{i,j} + \theta\Delta\Gamma_i\,, \tag{7.21}$$

   where θ represents the underrelaxation factor which has been set at $\theta = 0.01$ for this work.
8. The criterion for convergence is given by Equation 7.22. The loop reinitiates from step 2 as long as this condition is not satisfied.

$$\frac{|\Delta\Gamma|}{|\Gamma|_{\max}+1} > 0.02\,. \tag{7.22}$$

Convergence is achieved upon meeting the condition specified in (7.22). Now, the instantaneous forces acting on the blade can be calculated. Subsequently, the bound vorticity is shed into the wake, and the updated geometry is configured. The iteration loop reinitiates the subsequent time step.

7.2. Implementation

With the computational framework for the lifting line method outlined in the previous Section 7.1, this section focuses on integrating the test rotor into the established code. The rotor under investigation is defined in Section 7.2.1, where its discretization into vortex filaments is also detailed. The lifting line method necessitates the use polars for the aerodynamic coefficient, which have been obtained in Part II of this thesis. Given that these polars do not cover the full range of angles of attack encountered, extrapolation is required for modeling the post-stall region, as described in Section 7.2.2. Finally, Section 7.2.3 will specify the flow conditions the rotor will be subjected to in the simulations.

7.2.1. Rotor Definition & Dicretization

The company has no final design for a large, commercially viable rotor. Nevertheless, the second prototype, featuring a diameter of $D = 6m$, is available. Since the focus of this research is directed at large rotors subjected to high wind speeds at sea, the prototype rotor has been upscaled to a 3 MW counterpart. The characteristics of this upscaled rotor are as follows:

- The rotor diameter is set at $D = 100$ m.
- The blade span uniformly employs the NACA 63(4)-421 airfoil.
- Zero twist and pitch throughout the entire blade span.
- The chord distribution is derived from the TU Delft rotor B, as documented by Michallef [84].

The latter has been selected, since directly scaling the 6m prototype would result in unrealistically large chords; where the tip chords would extend to approximately $c = 12$ m. The distribution described by Michallef [84] has been adjusted for the root region, where the indentation from the original definition has been removed. This adjustment ensures better alignment with the conceptual large-scale rotor envisioned by the company.

Discretization of the rotor is shown in Figure 7.5. In this figure, the solid lines represent the panels, where circulation Γ is constant along the boundaries (recall from Helmholz's theorems in Section 7.1.2). It has been observed that increasing the panel density beyond $n_b = 20$, has minor influence on the results. Therefor, the total number of panels is set to 40 (for two blades). The control points are placed

at quarter-chord, coinciding with the lifting line. The collocation points, where the Neumann boundary conditions is enforced, are placed at $0.75c$. Finally, the vortex filaments, control points and collocations points are shifted towards the axis of rotation with $0.3c$.

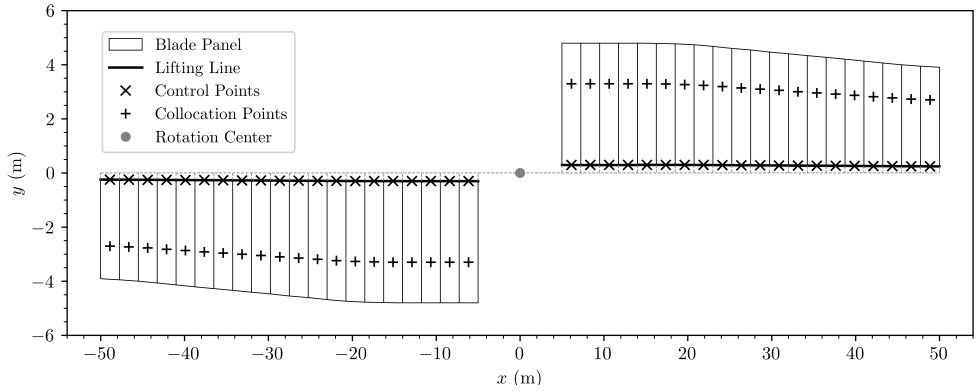

Figure 7.5: Geometry and discretization of the test rotor.

7.2.2. Polar Extrapolation

As described in Section 7.19, the iteration loop for bound circulation relies on polar data for the aerodynamic coefficients. The implemented data in this lifting line study are derived from polar data outlined in Section 6.3. It's noteworthy that near the rotor's root, particularly during its retreating motion, the rotor will be subjected to deep stall; conditions which extend beyond the angle of attack range provided by the polar data. To address this, various methodologies for extrapolating polars across a complete $360°$ range have been developed. This study considers three extrapolation techniques: the approach by Montgomerie [85], the Viterna method [87], and the Aerodas method developed by Spera [86]. These approaches use polar data up to stall conditions as input and utilize different techniques to predict the aerodynamic coefficients beyond stall.

Figure 7.6 shows the predicted outcomes of the three methods under consideration. Notably, there's a significant variation in their predictions of the lift coefficient, while the drag coefficient predictions appear more aligned. As will be discussed in Chapter 5, the selection of model can have a substantial impact on the results regarding power and thrust for a full rotor simulation. For the NACA 63(4)-421 airfoil, central to this study, no experimental data exists for deep stall conditions. Therefore, two selection can be based on two criteria: (1) The URANS calculations that extend beyond the maximum lift coefficient at stall (angles of attack ranging from $14°$ to $20°$) to identify which model most accurately reflects the observed trends. (2) Given the classification of the airfoil as "thick", where trailing edge stall is the driving mechanism, the post-stall behavior can be compared with similar patterns observed in

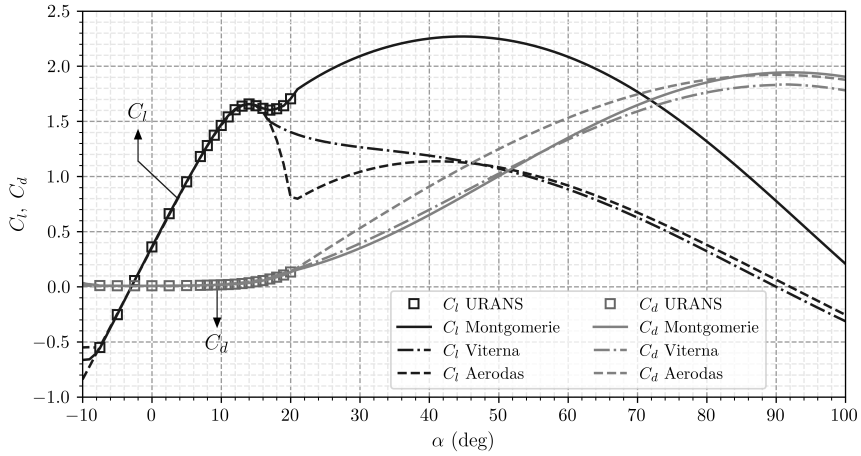

Figure 7.6: Extrapolation of lift and drag coefficients for NACA63(4)-421, as calculated by the Montgomerie [85], Aerodas [86] and Viterna [87] method.

other thick airfoils.

Figure 7.6 demonstrates that of the methods evaluated, only the Montgomerie method successfully reproduces the lift recovery under post-stall conditions, which have been observed in the URANS simulations. On the other hand, the Aerodas model appears to align better with the characteristics of leading-edge separation stall. When this is compared with the post-stall data of the S809 airfoil [71], also a "thick" airfoil, the lift coefficient's trend most closely resembles that predicted by the Montgomerie method. Based on these observations, the Montgomerie model has been chosen for use in this study.

7.2.3. Flow Conditions

The company has stated its specific aim for their rotor to operate under wind speed conditions exceeding typical cut-off speeds for convential HAWTs. Their target is to achieve operational capability in wind speeds up to 70 m/s; a condition that will not be found for all marine environments. To operate under these conditions necessitates an exceptionally small rotor plane tilt angle. Given the varying design requirements based on the rotor's geographical location, particularly concerning structural integrity, the evaluation is divided into two scenarios. The first scenario addresses environmental conditions typical of the North Sea, while the second scenario focuses on conditions associated with tropical typhoons in the Western Pacific.

Scenario 1: North Sea
Based on the wind data study by Gonzalez-Aparicia et al. [69], it's noted that the North Sea experiences wind speeds reaching 30 m/s about five times annually. The highest recorded wind speed from 2016 to 2022 was 39.22 m/s. Consequently, the wind speeds considered for this scenario range from $U_0 = 20$ to 40 m/s. The set of rotor plane tilt angles is determined from $\alpha_r = \{20°, 25°, 30°, 35°\}$

Scenario 2: Western Pacific
This scenario focuses on the intense typhoon winds that frequently occur in the Western Pacific. Typhoon season typically starts in April with milder storms and extends until November, with the most severe typhoons usually striking in August and September. When examining wind data off the coast of Japan, an average of 18 typhoons are recorded annually [88]. During these events, wind speeds reach up to 65 m/s and beyond. For the Western Pacific scenario, the considered wind speeds range from $U_0 = 40$ to 65 m/s. Rotor plane tilt angles considered here are $\alpha_r = 10°$ and $15°$.

The inclusion of lower wind speeds aims to identify viable operational points. These points describe a combination of rotor plane tilt angle, $\alpha_{r,oper}$, and tip speed ratio, λ_{oper}, that meet the requirement of the rotor to produce at its rated power of 3 MW. Recall that the primary objective of this study is to examine the feasibility of using shock-stall as a passive mechanism for overspeed protection. This is assessed by: (1) Defining initial points of operation. (2) Subsequently assuming a generator failure; i.e, the rotor becomes fully unloaded. As a consequence, the rotor accelerates towards its runaway tip speed ratio, λ_{run}. By analyzing the runaway tip speed ratio across various wind speeds and tilt angles, insights can be gained into the effectiveness of shock-stall in decelerating the rotor and preliminary judgements can be made regarding the safety during generator failure.

8

Lifting Line: Verification/ Validation

Similarly as for the CFD study presented in part II of this work, it is desired to establish a verification (quality control) validation (quality assurance) process to ensure the accuracy of the lifting line approach, which has been described in Section 7.1.

Firstly, a runaway scenario for the 3MW rotor described in Section 7.2.1 will be examined in Section 8.1. Here, it is ascertained that the blade loading for a full rotation converges after a specific number of rotations.

The emphasis for the validation procedure is on the proficiency of the code in accurately simulating the real-world physical behaviors of wind turbines. This validation has been conducted internally within the company, and this chapter will highlight two validation cases.

The first case involves the NREL Phase VI turbine, widely used for code validation. Only axial flow is considered for this case. The code's ability to predict rotor power and thrust at varying wind speeds at fixed rotational velocity is presented in Section 8.2.

Since the lifting line simulations in this study will incorporate rotor tilt, it is desired to validate the code for non-axial inflow as well. Given the novelty of rotor tilt, experimental observations from a rotor subjected to yaw have been considered. Fundamentally, yaw and tilt are analogous in their effects, excluding ground effects. The Mexico project rotor has been tested for a yaw angle of $\psi = 30°$, which corresponds to a complementary rotor plane tilt angle of $\alpha_r = 60°$. Details on the calculated forces at various sections along the rotor span are presented in Section 8.3.

8.1. Verification

The aim is to confirm that the computed rotor power and thrust do not vary with the number of rotations designated for a single simulation. Once a certain number of rotations is completed, both the power coefficient C_P and the thrust coefficient C_T, assessed over a full rotation, are expected to reach a steady state. If this condition is satisfied, the wake can be considered as *developed*.

A simulation of the lifting line model under runaway conditions; i.e, unloaded rotor where $C_P = 0$, is shown in Figure 8.1 for an incoming wind speed of $U_0 = 40$ m/s, rotor plane tilt angle $\alpha_r = 25°$ and tip speed ratio $\lambda = 5.84$. Figure 8.1a shows the temporal development of the rotor's power coefficient and torque over 6 full rotations. It can be observed that after approximately 3.5 rotations, the power coefficient reaches a steady state. Note that the instantaneous torque varies with the azimuthal position of the blades, exhibiting a sinusoidal motion. Therefore, the power coefficient is calculated by averaging over a full rotation. The convergence time of the power coefficient displays some variation across simulations for varying flow conditions. Thus, to ensure a fully developed wake, all simulations reported in the results chapter 9 are conducted for six rotations.

Moreover, Figure 8.1b illustrates the trajectory of the vortex panels through three-dimensional space after six rotations. The findings are in line with expectations, as the following observation can be made:

- Roll-up of the tip vortices in the blade tip region.
- Downward deflection of the wake, attributed to the thrust, which exerts a non-axial force on the flow.

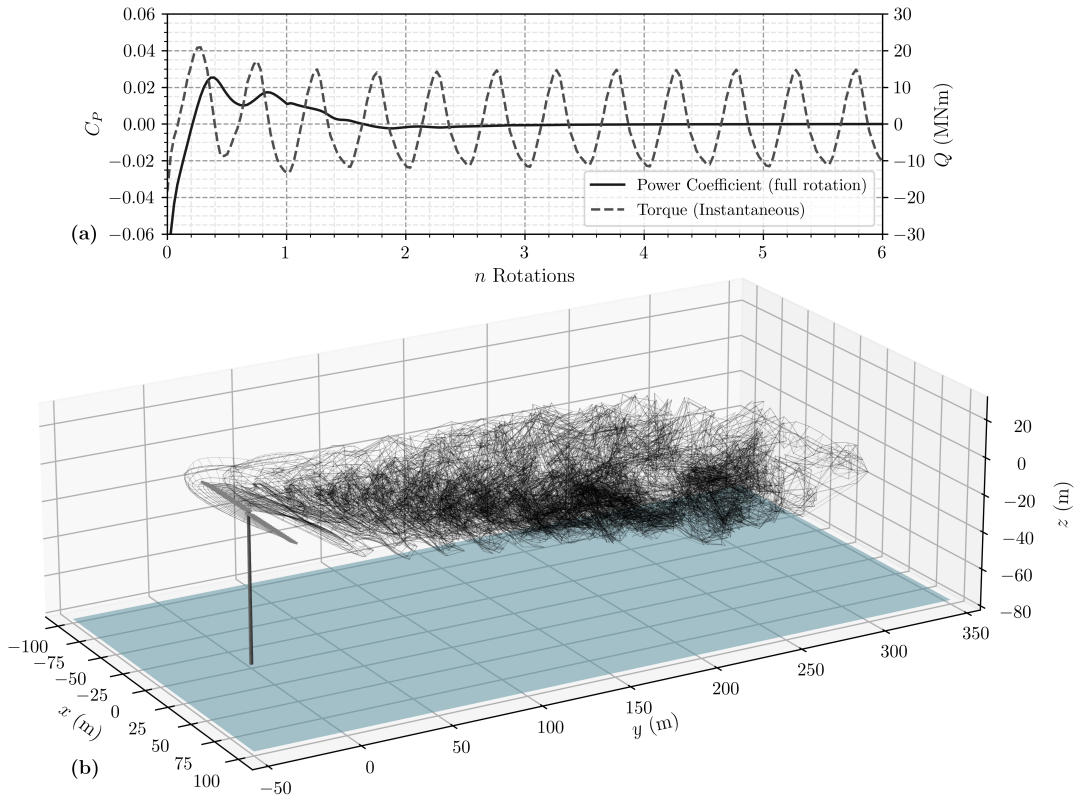

Figure 8.1: Convergence of power coefficient C_P. Temporal development of C_P and torque Q shown in **(a)**, whereas **(b)** shows the convection of wake panels. $U_0 = 40$ m/s, $\alpha_r = 25°$ and $\lambda = 5.84$.

8.2. NREL Phase VI

As an integral part of the Unsteady Aerodynamics Experiment (UAE), the objective of the NREL Phase VI turbine has been to provide information on the aerodynamic behavior of full-scale HAWTs. The turbine features a two-bladed rotor with a radius of $R = 5.029$ m, where the S809 airfoil spans the cross-section profile for the entire blade. The experimental campaign performed by Hand et al. [89] was conducted in the 24 x 36-m wind tunnel at NASA's Ames Research Center – the only facility capable of accommodating a rotor of this size. For the purposes of validation within this study, the experimental data from Sequence S has been selected. The data includes wind speeds ranging from $U_0 = 5$ up to 25 m/s for a constant rotational speed of $\Omega = 72$ rpm and pitch angle of $\theta = 3°$.

Polar data for the S809 airfoil were obtained from the work of Somers [71] for Reynolds numbers $Re_c = 7.5 \times 10^5$ and $Re_c = 1.0 \times 10^6$. These polars were extrapolated using the Montgomerie model [85]. The simulation advances through time with an azimuthal step size of $d\phi = 10°$. Furthermore, the simulation incorporates Snel's dynamic stall model and the Himmelskamp correction to account for stall delay.

The comparison of power and thrust is shown in Figure 8.2, showcasing the results from the lifting line method, the experimental data from Hand et al. [89] with associated uncertainty bands, and CFD predictions by Hashem et al. [90]. The results from lifting line code closely align with the experimental observations, fitting within the experimental uncertainty ranges across all tested wind speeds. For wind speeds exceeding $U_0 = 10$ m/s, the blades experience stall and while the CFD data deviates from the experimental data, the lifting line method remains in good accordance. It's important to acknowledge the substantial influence of the extrapolation method on the outcomes. While the Montgomerie [85] and Aerodas [86] methods have yielded satisfactory results, the Viterna model [87] tends to overestimate power and thrust when wind speeds exceed 10 m/s, indicating the onset of stall conditions for a significant portion of the blade.

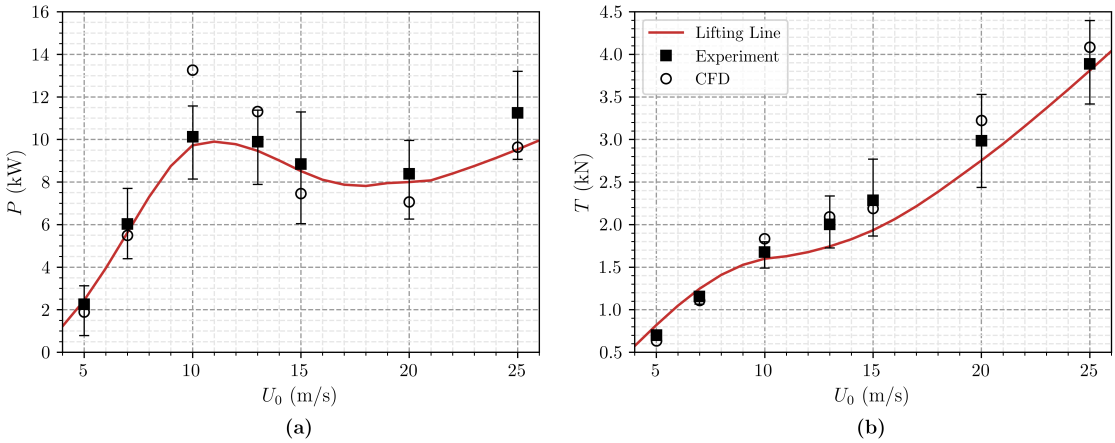

Figure 8.2: Power **(a)** and Thrust **(b)** at constant rotational speed ($\Omega = 72$ rpm) for NREL Phase VI turbine. Experimental data retrieved from Hand et al. [89] and URANS data from Hashem et al. [90].

8.3. Mexico Project

For the MEXICO (Model Rotor Experiments In Controlled Conditions) project, a collaborative effort involving 10 institutions, experiments were conducted on a three-bladed wind turbine with a diameter of 4.5 meters. This turbine has been experimentally tested in the 9.5 by 9.5 meter open wind tunnel of the DNW's Large Low-speed Facility in the Netherlands. Schepers et al. [91] documented the experimental campaign, which included tests under yawed inflow conditions. Specifically, the yaw angle was set at $\psi = 30°$ (equivalent to a rotor plane tilt angle of $\alpha_r = 60°$), for a wind speed of $U_0 = 15$ m/s. The collective pitch angle of the blade has been set at $\theta = -2.3°$. Furthermore, the turbine's blades incorporated three different airfoils, details of which are presented in Table 8.1. Since the original study by Schepers et al. [91] did not provide the required polar data, alternative sources have been used. Table 8.1 also shows the chord-based Reynolds numbers corresponding to these polars. Blade pressure distributions were captured using 148 Kulite pressure sensors, positioned across five blade sections at 0.25, 0.35, 0.60, 0.82, and 0.92 r/R.

Table 8.1: Airfoils spanning the MEXICO project rotor, including Reynolds number Re_c for available polar data.

Airfoil	Radial Section	Polar Re_c
DU91-W2-250	$[0, 0.5]$ r/R	3.0×10^6
RISØ A1-21	$[0.5, 0.72]$ r/R	1.6×10^6
NACA 64(3)-418	$[0.72, 1]$ r/R	3.0×10^6

For the configuration of the lifting line method, the polars were extrapolated using the Aerodas method [86]. Additional functions related to dynamic stall and the Himmelskamp effect were not utilized.

Figure 8.3 shows the normal and tangential forces at radial positions r/R= 0.60, 0.82 and 0.92 over a full rotation derived from the lifting line analysis, alongside the forces recorded during the experimental study. The lifting line method demonstrates it can accurately predict these forces. However, some discrepancies are observed, particularly at the radial station r/R=0.60, where the forces are slightly overestimated. The total thrust resulting from the lifting line analysis is $T = 1505$ N, compared to approximately 1340 N recorded in the experiment. The total power output was computed at $P = 10.3$ kW, which is slightly higher than the experimental value of around 9.7 kW. Overall, the lifting line method demonstrates to be capable of handling non-axial inflow conditions with sufficient accuracy. Especially considering the results of other institutions, which can be found in the original source from Schepers et al. [91].

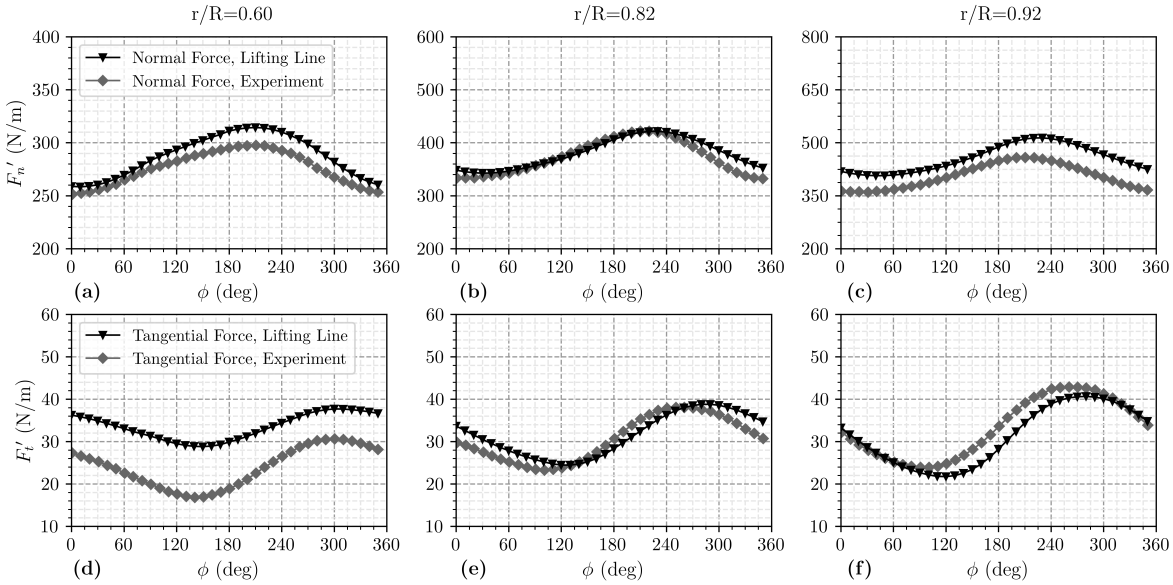

Figure 8.3: Azimuthal variations of normal force F_n **(a) - (c)** and tangential force F_t **(d) - (f)** for Mexico Rotor at radial stations $r/R = \{0.60, 0.82, 0.92\}$, where $U_0 = 15$ m/s, $\lambda = 6.67$ and $\psi = 30°$.

8.4. Conclusion

The lifting line code has demonstrated its proficiency in handling various turbine configurations and flow scenarios. Specifically, for the NREL Phase VI turbine, the method was able to predict rotor power and thrust accurately, aligning well within the experimental uncertainty ranges. This validation process highlighted the critical role of selecting the appropriate extrapolation method for airfoil polars. In this case, both the Montgomerie and Aerodas methods yielded satisfactory results, whereas the Viterna model showed a tendency to overestimate power and thrust when a large portion of the blade undergoes stall. However, it's important to note that broad conclusions regarding the effectiveness of these methods cannot be drawn, as their accuracy depends on the selected airfoil and its associated stall behavior.

Additionally, the model's performance for the MEXICO project rotor showcased its ability to manage non-axial inflow conditions. This is particularly relevant for the highly tilted cases examined in the results chapter 9. The analysis underscored the model's accuracy in predicting forces under azimuthal variations, despite minor overpredictions of the forces at certain radial stations.

9

Lifting Line: Results & Discussion

In this concluding chapter of Part III, the results of the lifting line model will be presented. The predefined scenarios outlined in Section 7.2.3 will be treated first, where Section 9.1 examines storm conditions at the North sea, whereas Section 9.2 addresses the significantly higher wind speeds encountered during typhoons in the Western Pacific. The primary focus for these two scenarios is directed towards understanding how the rotor's rotational speed responds to variations in wind speed, with a particular emphasis on the behavior of an unloaded rotor under these conditions. Furthermore, Section 9.3 offers an introductory exploration of the rotor's susceptibility to and potential effects from transonic buffet. The chapter concludes with a discussion, offering insights into the implications of the obtained results.

9.1. Scenario 1: North Sea

For the lifting line analysis of the rotor subjected to storm conditions at the North Sea, the considered wind speeds range from $U_0 = 20$ m/s to $U_0 = 40$ m/s. For these wind speeds, four rotor plane tilt angles, varying from $\alpha_r = 20°$ to $\alpha_r = 35°$ are considered. the rotor's potential operating points can be determined for an initial assessment at $U_0 = 20$ m/s. Given the rotor's rated power of 3 MW, the operational power coefficient, $C_{P,oper}$, is calculated as,

$$C_{P,oper} = \frac{P = 3\text{MW}}{0.5\rho_\infty \pi R^2 {U_0}^3} \approx 0.078. \tag{9.1}$$

where the free stream density $\rho = 1.225$ kg/m^3 and rotor radius $R = 50$ m. Figure 9.1 shows the resulting power coefficient curves, illustrating the flexibility in choosing operational points. Numerous combinations of tilt angle α_r and tip speed ratio λ exist, that satisfy $C_P = 0.078$. Furthermore, for a fixed

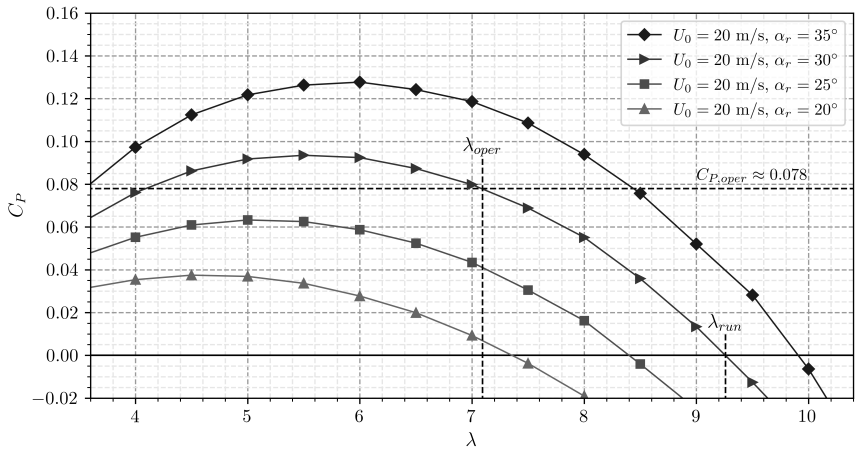

Figure 9.1: Power Coefficient C_P- curves for varying rotor plane tilt angle α_r at incoming wind speed $U_0 = 20$ m/s.

tilt angle, the operational point is not unique; the curves intersect with the operational power coefficient twice. The focus will be on the rightmost operational tip speed ratio. This has the company's preference, since operating at the lower tip speed ratios can lead to backflow issues on the blade's retreating side. Figure 9.1 also illustrates the runaway tip speed ratios λ_{run}, representing the maximum rotational speed for an unloaded turbine ($C_P = 0$). The evaluation of shock-stall as a potential overspeed protection mechanism (referred to as the "braking effect") involves analyzing the variation of the runaway tip speed ratio for increasing wind speeds. The power coefficient is an output variable of the lifting line analysis, while λ is an input parameter. To find the runaway tip speed ratio, a Brent's scheme [92] is employed, which iterates towards the tip speed ratio satisfying $C_P = 0$.

Before continuing towards the analysis of shock-stall as a breaking mechanism, an important preliminary observation can be made from Figure 9.1. Namely, reducing rotor tilt angle α_r acts as an effective method of braking by itself. Consider the rotor operates at $\alpha_r = 30°$ and $\lambda \approx 7.1$, as indicated in Figure 9.1. In the event of a generator failure, the rotor will accelerate towards its runaway tip speed ratio of $\lambda_{run} \approx 9.25$, given that the tilt angle remains fixed. In contrast, when the tilt angle is reduced to $\alpha_r = 20°$, the tip speed ratio is restrained to $\lambda_{run} \approx 7.35$.

Regarding the braking effect as a result of shock stall, reviewing an example first will help to clarify the examined mechanism. The effect can clearly be identified when comparing wind speeds of $U_0 = 20$ m/s and $U_0 = 30$ m/s at a fixed tilt angle of $\alpha_r = 30°$. Figure 9.2 shows the radial distribution of tangential force over a full rotation at runaway tip speed ratio. At $U_0 = 20$ m/s, the highest Mach number observed at the blade tips is $M_\infty = 0.57$, indicating operation fully within the subsonic regime. Increasing the wind speed to 30 m/s (Figure 9.2b), leads to a considerable increase in drag on the advancing side, attributed to the onset of shock-stall. The resulting tangential force from the increased drag contributes significantly to the resulting rotor torque, thereby substantially lowering the runaway tip speed ratio.

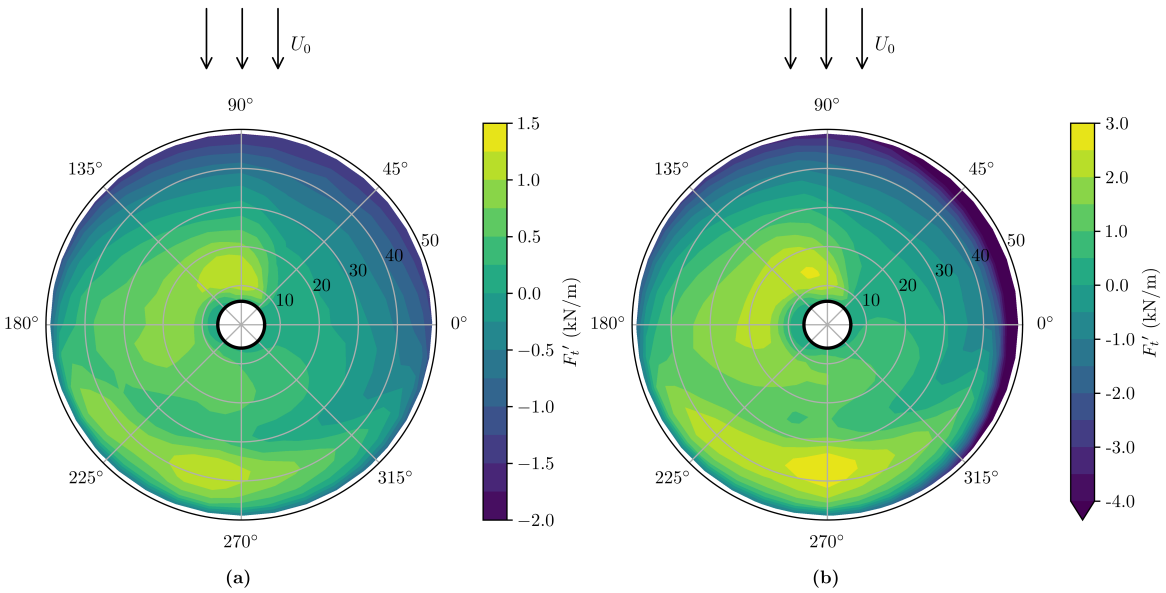

Figure 9.2: Radial distribution of tangential force F_t' across a full rotation, as seen from above (rotation in counter-clockwise direction). Presented for incoming wind speeds $U_0 = 20$ m/s **(a)** and $U_0 = 30$ m/s **(b)**, evaluated at runaway tip speed ratio with a tilt angle of $\alpha_r = 30°$.

The occurrence of the braking effect due to compressibility has been demonstrated, but its efficacy remains a point of inquiry. Figure 9.3a depicts the runaway tip speed ratios across wind speeds from $U_0 = 20$ m/s to $U_0 = 40$ m/s, and for reference, a comparison where the flow is assumed to be incompressible is also shown. For the incompressible calculations, the tabulated lift and drag polars are retrieved for a constant Mach number ($M_\infty = 0.2$). This naturally leads to a constant runaway tip speed ratio, since the power coefficient curve is now independent of wind speed U_0. When compressibility effects are accounted for, a notable reduction of the runaway tip speed ratio is observed for increasing

wind speeds as a result of shock-stall. Examination of Figure 9.3b, which presents the rotor's rotational speed, reveals a diminishing increase in rotational speed under compressibility effects. Nevertheless, the gradient does not go towards zero; hence, the rotational speed does not reach a maximum value.

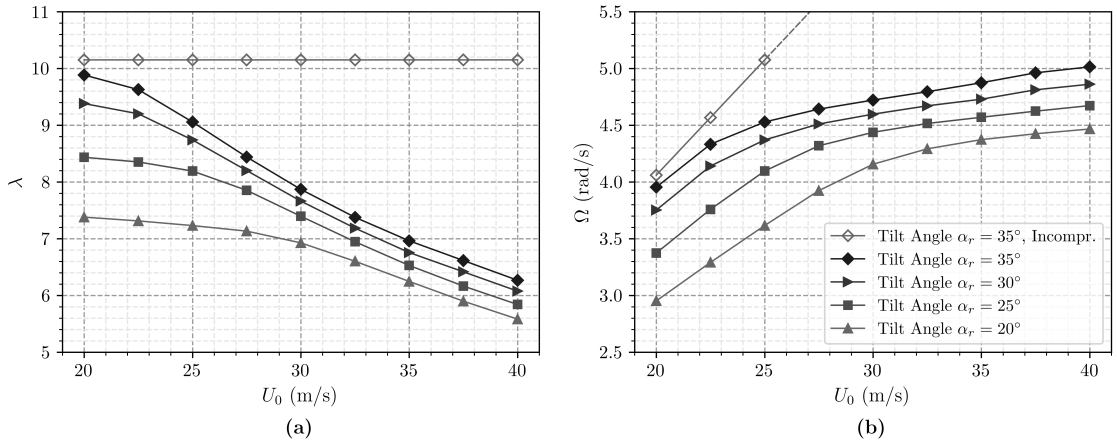

Figure 9.3: Tip speed ratio λ_{run} **(a)**, angular velocity Ω_{run} **(b)** at runaway for incoming wind speeds $U_0 \in [40, 60]$ at rotor plane tilt angles $\alpha = 10°, 15°$.

9.2. Scenario 2: Pacific

For the second scenario, the focus shifts towards higher wind speeds prevalent in the Western Pacific, off the coast of Japan. The considered wind speeds range from $U_0 = 40$ m/s to 65 m/s. These extreme conditions necessitate a significant reduction in rotor plane tilt angle. Figure 9.4 shows the power coefficient curves for an incoming wind speed of 40 m/s at tilt angles $\alpha_r = 10°$ and $15°$. The operational power coefficient can be calculated using Equation 9.1, which results in $C_P \approx 0.0097$. This indicates that establishing a stable operational point becomes considerably more challenging, compared to those encountered in the North Sea (discussed in Section 9.1). Minor fluctuations in tip speed ratio or wind speed will significantly impact the turbine's power output.

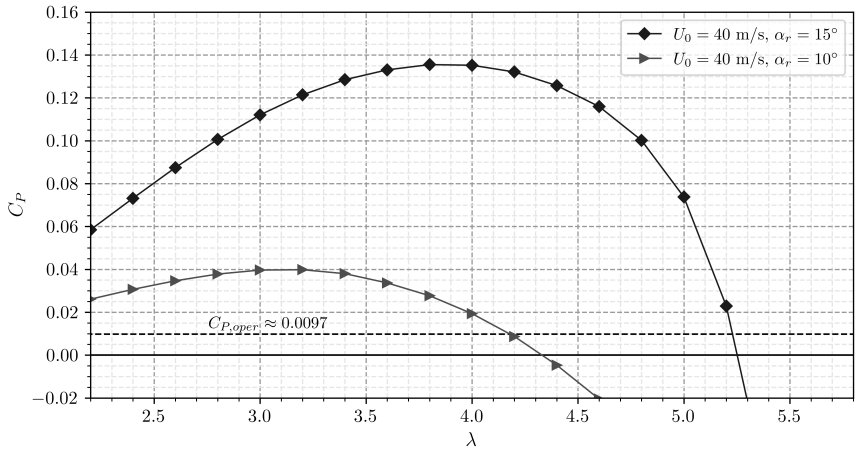

Figure 9.4: Power Coefficient C_P-curves for varying rotor plane tilt angle α_r at incoming wind speed $U_0 = 40$ m/s.

The runaway tip speed ratios are depicted in Figure 9.5. Again, a notable decrease is observed with increasing wind speeds, attributed to shock-stall effects. Examining the rotor's rotational velocity, as shown in Figure 9.5b, it becomes evident that for these wind speeds a maximum is found. Specifically, for a tilt angle of $10°$, this peak is reached at $U_0 = 57.5$ m/s, where rotational speed is 3.99 rad/s. Beyond this wind speed, the rotational speed starts to decline slightly. This might be a counterintuitive observation, but Figure 9.5c helps to explain this trend. Here, the maximum Mach number at the blade tips is shown. While the rotational velocity nears and exceeds its peak, the Mach number on

the advancing side of the blade continues to rise. This is a result of the continually increasing relative incoming wind speeds. In essence, the difference between the minimum (retreating side) and maximum (advancing side) Mach number grows as the incoming wind speed increases. The tangential force working on the tips, which is dominated by the drag force (near-zero inflow angle Φ, refer to Equation (7.2)), experiences a more pronounced increase on the advancing side. This can be observed from the polar field presented in Chapter 6, Figure 6.7. A large gradient can be observed past the drag divergence Mach number M_{DD}. Since the retreating side operates in the subcritical regime, the impact on this side is comparatively minor. Hence, the tangential force working on the advancing side of the blade continues to increase, and the rotor cannot accelerate beyond $\Omega = 3.99$ rad/s.

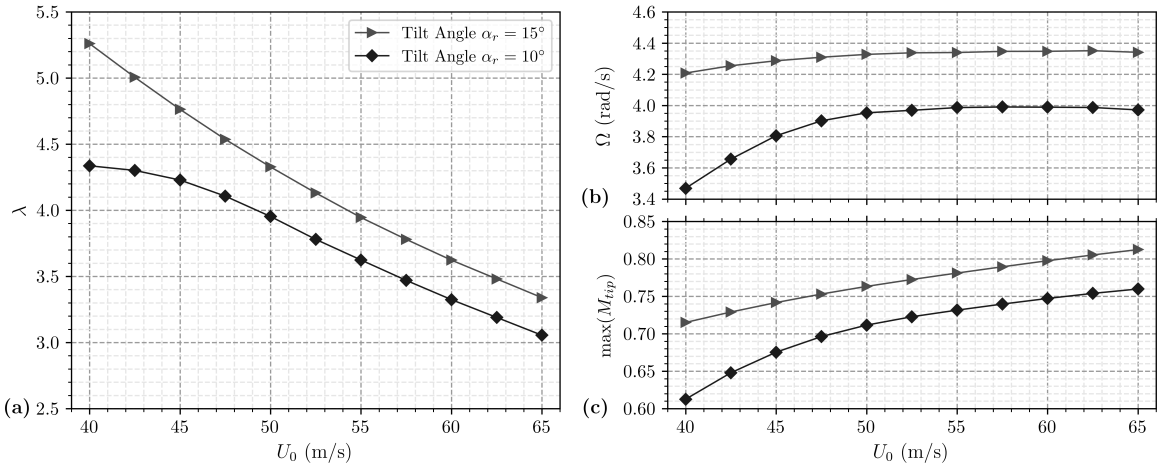

Figure 9.5: Tip speed ratio λ_{run} **(a)**, angular velocity Ω_{run} **(b)** and maximum tip Mach number M_{tip} **(c)** at runaway for incoming wind speeds $U_0 \in [40, 60]$ at rotor plane tilt angles $\alpha = \{10°, 15°\}$.

9.3. Susceptibility to Buffet

Until now, the analysis has not considered the effects related to the onset of transonic buffet. Instead, the polars that have been implemented assumed the averaged lift and drag coefficients. However, insights from the CFD study presented in Part II of this work highlight that as the flow enters the supersonic regime, it rapidly becomes prone to shock-induced separation, resulting in buffet.

Given that the local conditions for Mach number and angle of attack vary for each radial and azimuthal position of the blade, full CFD computations are required to model buffet on a rotor with considerable accuracy. Nevertheless, some preliminary insights into the rotor blades' susceptibility to buffet can be given. Figure 9.6 shows the Mach number and local angle of attack in the blade tip region

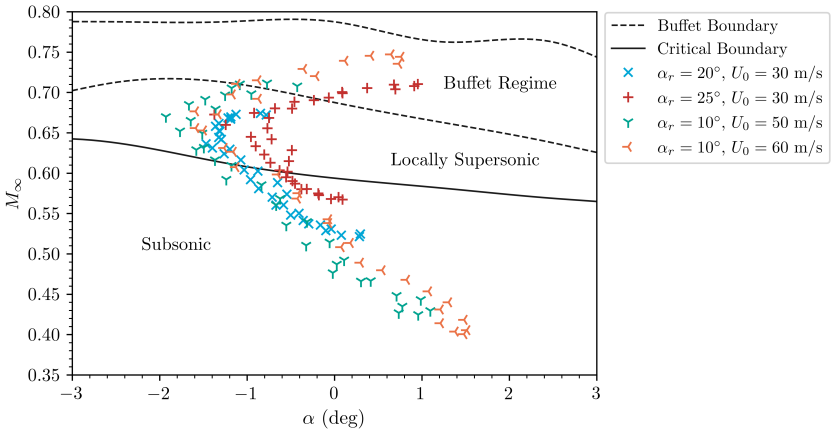

Figure 9.6: Local angle of attack α and Mach number M_∞ for rotor tip panel over a full rotation at runaway tip speed ratio λ_{run}. A point is plotted for every $d\phi = 10°$.

for various combinations of rotor tilt angle and incoming wind speed. It is evident from the figure that an increase in either the tilt angle or the wind speed rapidly results in entering the buffet regime. Nevertheless, it is important to note that achieving a significant braking effect through drag associated with a shock that does not induce separation (and hence, no buffet), is achievable.

In the context of the loads in the tip region under buffet conditions, a basic assessment can be conducted. Referring to Figure 9.6, it is observed that the tip section of the rotor at a wind speed of $U_0 = 60$ m/s and a tilt angle of $\alpha_r = 10°$ encounters the buffet regime at the advancing side. Under these conditions, the Mach number is approximately $M_\infty = 0.725$, and the angle of attack varies within $\alpha \in [-1°, 1°]$. For simplification, we assume $\alpha = 0°$. The calculated reduced frequency for these flow conditions, as obtained from the URANS simulations in Part II, is found at $k_r = 0.826$. The reduced frequency can be related to the physical frequency by using Equation (9.2).

$$\begin{aligned} k_r &= \frac{2\pi f(c/2)}{U_\infty}\,, \\ f &= \frac{k_r U_\infty}{\pi c}\,, \\ f &= 13.28 \text{ Hz}\,, \end{aligned} \tag{9.2}$$

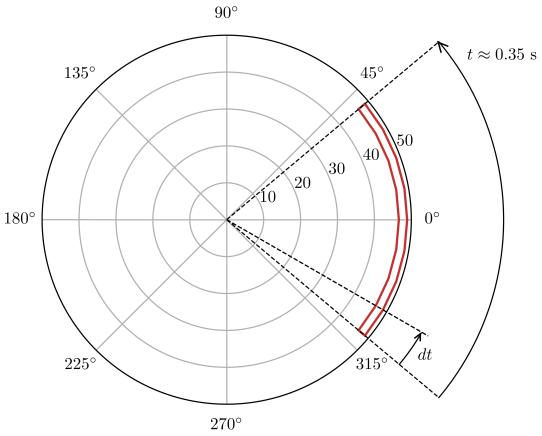

Figure 9.7: Tip region subjected to buffet. $U_0 = 60$ m/s, $\lambda = \lambda_{run}$ and $\alpha_r = 10°$

Here, the free stream velocity in the tip section is taken as $U_\infty = 246.5$ m/s, and the chord length $c = 4.885$ m. Figure 9.7 shows the tip panels during the rotation a rotation in the buffet regime. The lifting line method progresses in time with azimuthal step $d\phi = 10°$. The time step can then be calculated as $dt = d\phi/\Omega$. This results in the tip region being in the buffet regime for a duration of 0.35 s. Consequently, as the tip region traverses the advancing side, it undergoes approximately 4.5 buffet cycles. The calculated fluctuations for the lift coefficient are $\Delta C_l \approx 0.32$, where the time-avaraged coefficient equals 0.015. The radial force distribution calculated for the tip region is thus represented by:

$$\begin{aligned} \min(F_n') &= -9.61 \text{ kN/m}\,; \\ \max(F_n') &= 17.07 \text{ kN/m}\,; \end{aligned} \tag{9.3}$$

The calculations indicate that the fluctuating forces working on the blades can become exceptionally large. These findings suggest, considering the magnitude and frequency of the loads, that operation in the buffet regime can ultimately lead to structural failure.

9.4. Discussion

The primary focus of this chapter has been addressed at evaluating the feasibility of using shock-stall as an effective mechanism for overspeed protection. The first and only research that has been dedicated to this subject has been conducted by Wood [6] in the context of small HAWTs ($P < 3$ kW). His findings rejected the hypothesis, since drag divergence occurred to slowly. In contrast, this work has demonstrated that shock-stall can be used as a passive overspeed protection mechanism for a tilted turbine. However, there are a few important considerations, which will be discussed in this section.

For the first test case, considering North Sea conditions, a maximum rotational speed has not been established. The question arises what the practical benefits would be of using shock-stall as a breaking mechanism. Especially given that the rotor has the capacity to further reduce its tilt angle, which has shown to be an effective braking mechanism. In contrast, for the second case considering typhoon conditions found in the Western Pacific, a definitive maximum rotational speed has been found. In these

scenarios, where the tilt angle is already minimized for operational conditions, a passive overspeed protection mechanism would be highly beneficial.

It is important to note that the approach did not account for 3D effects. Prouty's work [93] on helicopter aerodynamics suggests that for thick airfoils, the effective tip Mach number could be reduced by approximately $\sim 10\%$ due to streamlines dispersing at the tips. This implies a delayed onset of shock-stall. Therefore, the findings of this study might undervalue the maximum rotational speed at runaway conditions, and the actual peak will likely be found at higher wind speeds.

In the context of transonic buffet, it has been shown that the rotor can be prone to major load fluctuations under operational or runaway conditions. Although precise calculations are beyond the scope of the lifting line method used here, initial assessments indicate that buffet-related load fluctuations could pose severe risks to blade structural integrity. However, prior research has shown that buffet mechanisms are also influenced significantly by 3D effects. A recent experimental study from D'Aguanno et al. [31] has shown that load fluctuations are significantly reduced for finite wings compared to full-span airfoils.

Additional to the negligence of 3D effects, two more assumptions that have been made should be highlighted. Firstly, for reasons regarding computational time of the URANS simulations, the decision was made to include a single Reynolds number Re_c, along with the assumption of a turbulent boundary layer. Its implications have been highlighted in the discussion of the CFD study (refer to Section 6.4). Secondly, the lifting line theory relies on the foundational concept of potential flow, which assumes the flow to be incompressible. In this work, lift and drag polars have been implemented for compressible flow. This does not directly violate the approach that has been taken, as the circulation Γ accurately reflects the behavior of an airfoil under compressible or shocked flow conditions. However, it should be noted that the wake is still considered to be incompressible. As highlighted by Yan and Archer [2] (refer to Chapter 3), compressibility effects in the wake can significantly influence rotor performance, potentially resulting in 20% reduction in power output when compressibility effects are considered.

10 Conclusions

This thesis aimed to explore the effects of compressible and transonic flow effects on the performance of a tilted wind turbine. In addressing this aim, the thesis has been split into two parts. The initial phase concentrated on modeling the characteristics of the NACA 63(4)-421 airfoil, which is the design airfoil for the company's wind turbines, using a URANS framework. This allowed to capture the complex phenomena of shock-induced separation. Ultimately, the findings from this study provided polars for the aerodynamic coefficients. In the second phase, these polars were implemented in the company's lifting line code, where the company's 3MW concept rotor could be analyzed. Conclusions are given first in Section 10.1. The chapter concludes with recommendations for future research and for the company in Section 10.2

10.1. Conclusions

Both the URANS and lifting line study have been guided by a primary research question. These are further divided into sub-questions, designed to incrementally build an understanding of the phenomena and their implications on wind turbine performance and safety. The following sections will delve into these questions and present the answers.

Q-1: What is the influence of high subsonic and transonic Mach numbers on the loads for the thick NACA 63(4)-421 airfoil, typical for wind turbine blade applications?

To address this main research question, two sub-questions have been formulated. The first focuses on the subcritical regime, while the second delves into scenarios surpassing this regime, particularly when shock waves emerge. The sub-questions will be addressed first, followed by an answer to the main question.

Q-1-1: To what extent can corrections to the incompressible aerodynamic coefficients accurately model the compressible coefficients?

The study first assessed the extent to which existing corrections could accurately predict the onset of local supersonic flow and their effectiveness to predict the aerodynamic coefficients for the subcritical regime. The findings did not reveal a uniformly superior method among the Prandtl-Glauert, Karman-Tsien, and Laitone corrections. The Prandtl-Glauert rule proved most accurate in predicting the critical Mach number at the lowest angle of attack examined ($\alpha = 5°$), while Karman-Tsien offered more precise estimates at higher angles of attack ($\alpha \geq -2.5°$). Ultimately, the Karman-Tsien rule emerged as the favored option, though the Prandtl-Glauert rule also presented itself as a viable alternative due to its reasonable accuracy and simplicity.

Q-1-2: Under which flow conditions can we expect shock-wave formation and transonic buffet, and how do these influence the loads?

The critical boundary has successfully been established, characterized by a rapid increase in the drag coefficient beyond this limit, marking the drag divergence Mach number M_{DD}. Conversely, a reduction in the lifting capabilities has been observed during shock-stall onset, with the lift coefficient approaching

zero when a strong shock wave terminates on both the suction and pressure sides for all studied angles of attack $\alpha \in [-5.0, 5.0]$.

Upon increasing the Mach number beyond the critical boundary, the URANS simulations also successfully identified the buffet boundary. It was observed that buffet onset occurs shortly after the critical boundary is exceeded, triggered when the shock wave reaches sufficient strength to induce separation. Buffet emerged at a Mach number increment ranging between $\Delta M_\infty = 0.08$ and 0.1 past the critical boundary. The fundamental classification of buffet considers two types, and both have been found. Firstly, for the higher angles of attack, buffet of the second kind has observed, where a shock emerged exclusively on the airfoil's pressure side. The mechanism aligned with previous studies on supercritical airfoils, where separation emerges from both rearward growth of the shock-induced bubble and trailing edge separation, eventually collapsing into a single recirculation zone. Furthermore, the results have provided the first identification of buffet of the first kind for a non-symmetrical airfoil. It was found that the load fluctuations were significantly higher, where the obtained amplitude of the lift coefficient was in the order of two times higher compared to a single oscillating shock on the pressure side.

Taking everything into consideration, the main question can be answered. Although broad generalizations regarding thick airfoils should be approached with caution, the study's results align with the expectation that the pronounced curvature of the airfoil results in a high susceptibility to shock-induced separation, resulting in a low drag divergence Mach number. In terms of load implications, this translates to a rapid increase in drag at relatively low Mach numbers, theoretically making the NACA 63(4)-421 airfoil suitable for using shock-stall as an inherent overspeed protection mechanism (addressed in Q-1-1). Simultaneously, a high susceptibility to shock-induced separation, has shown to make the profile prone to transonic buffet. The observed load fluctuations, particularly at low angles of attack, suggest that operating a wind turbine in the buffet regime could lead to significant structural implications.

Q-2: How do the effects of compressibility, shocked flow, and transonic buffet impact performance and operational safety of a tilted wind turbine under extreme wind conditions?

Again, two sub-question have been established. The first sub-question, Q-2-1, explores the hypothesis that the increased drag associated with shock-stall can successfully prevent overspeeding under storm conditions. The second considers whether, either during operation or a runaway scenario, the rotor will enter the buffet regime, and its implications.

Q-2-1: Under what conditions can the action of shock-stall function as a passive overspeed protection mechanism for an unloaded rotor?

In addressing this question, the study examined two distinct scenarios. The first scenario focused on conditions typical of the North Sea. The findings indicated that shock-stall contributed substantially to braking effectiveness compared to what assuming incompressible flow. However, it was also noted that with continuously increasing wind speeds, the rotor did not reach a maximum rotational velocity. Furthermore, the results revealed that for the considered wind speeds, there is still room to decrease the tilt angle when under operation wind speed rapidly increases, effectively preventing the rotor from overspeeding.

For the second scenario, which focused on typhoon conditions in the Western Pacific, reducing the tilt angle as a braking strategy is no longer feasible. This is because operation in such conditions necessitates setting tilt to its minimal angle considered in the study ($\alpha_r = 10°$). However, for these conditions, a definitive maximum rotational speed has been found, meaning the rotational velocity will not further increase beyond an incoming wind speed of 57.5 m/s.

In summary, shock-stall can serve as an intrinsic overspeed protection mechanism for a tilted rotor, but its efficacy is dependent on the wind speed it will encounter, and thereby its geographical location.

Q-2-2: For which conditions will the rotor be susceptible to transonic buffet, and what are the resulting implications on rotor loading?

The simulations that have been executed to answer Q-2-1 considered the mean values of the aerodynamic coefficients. As pointed out while addressing **Q-1**, the load fluctuations in the buffet regime reach significant values. A preliminary calculation has been done to assess the loads as the tip region travels through the buffet regime. From this calculation, it was found that the rotor can be prone

to major load fluctuations under either operational or runaway conditions, that can seriously put its structural integrity at risk.

the main question can be answered partially. The research successfully demonstrates that the rotor can sustain operation and be protected from overspeeding through the action of shock-stall during storm conditions. However, these results are based on time-averaged aerodynamic coefficients. Concerning rotor safety, the study indicates that transonic buffet could have severe implications. Yet, providing a precise calculation of these effects falls beyond the scope of this thesis, as it necessitates either experimental data or a comprehensive three-dimensional Computational Fluid Dynamics (CFD) approach.

10.2. Recommendations

This final section presents recommendations for future endeavors, divided into two distinct sections. Firstly, Section 10.2.1 offers suggestions for subsequent academic research, considering both the remaining research gaps and new questions that have emerged from this study. Following this, Section 10.2.2 provides strategic advice to the company, outlining a proposed path for the continued development of their rotor, based on the insights gained from this research.

10.2.1. Directions for Academic Research

In the context of airfoil aerodynamics, this research is the first to identify buffet for a thick airfoil and to identify the occurrence of first-kind buffet on an asymmetrical airfoil. The URANS methodology that has been applied, however, has some limitations. In the context of numerical simulations, future work should include:

- Two-dimensional CFD with higher fidelity methods, such as DES or LES approaches. Unlike URANS, these methods offer enhanced predictive capabilities for large areas of separated flow, as is the case for thick airfoils that encounter shock-induced separation. Prior studies, such as the work of Fukushima and Kawai [74] showed that while URANS effectively predicted the frequency of the oscillations, (WM)LES obtained better predictions of the load amplitudes.
- Three-dimensional CFD of the blade tip region. This could provide insights into the tip relief effect as described by Prouty [93] and whether buffet fluctuations on rotor tips are less severe in a 3D framework as suggested by the experimental study of d'Aguanno et al. [31]. These simulations could be conducted using URANS, or also implement higher fidelity methods such as WMLES.

Consequently, validating the accurateness of these findings necessitates experimental data, which is currently lacking for thick airfoils subjected to transonic flow conditions.

Additionally, airfoil design strategies could be explored with the objective of expanding the operational regime between the drag divergence Mach number and the onset of buffet for thick airfoils. Ideally, an airfoil would operate under shock-stall without encountering oscillatory loads at any Mach number. However, a potential limitation of this approach may include the need for modifications such as the addition of bumps or similar features to affect the SBLI. While effective in mitigating buffet, such alterations could potentially compromise airfoil and, consequently, rotor performance during standard operating conditions.

Finally, in the context of wind turbine aerodynamics, this study focused on the operational and runaway scenarios at high transonic Mach numbers but did not address structural aspects. It is thus recommended to evaluate these structural aspects through experimental methods or thorough CFD studies. This should include an investigation into whether turbine blades can be designed to withstand the loads encountered during shock stall and buffet. Moreover, given that the blades were assumed to be infinitely stiff in this study, conducting aeroelastic studies would be beneficial to understand the effects of blade flexibility on load dynamics.

10.2.2. Engineering Design Recommandations

The primary question from the company was whether shock-stall could serve as a mechanism for overspeed protection. The findings indicate that the effectiveness of this principle is dependent on the encountered wind speeds. In scenarios typical of the North Sea, it was observed that reducing the rotor plane tilt angle is a more efficient overspeed protection strategy than relying on shock-stall.

When considering failure scenario's, it is assumed that the generator fails, meaning that the rotor will accelerate towards its runaway tip speed ratio. Simultaneously, if we assume the control of the rotor is lost, it is not possible to reduce the tilt angle. Therefore, it is advised to implement a safety mechanism, where the rotor will always return to its minimum tilt angle. This could be effectively achieved through the use of spring-loaded mechanisms or counterweights that activate upon detection of any malfunction. Such a safety feature would consistently protect the rotor from overspeeding under all circumstances.

For turbines intended for regions prone to annual tropical typhoons, relying solely on the previously mentioned strategy has proven not to be sufficient. In such locations, overspeed protection could potentially be attained through the phenomenon of shock-stall. However, this approach presents challenges related to load fluctuations arising from buffet. Logically, the company would also benefit from higher fidelity numerical simulations, especially regarding 3D effects, which are mentioned in the previous section. It is recommended that the company undertakes comprehensive experimental research focused on the rotor tip region as they enter the shock-stall regime. Only after confirming that the buffet-induced load fluctuations are either less severe than anticipated or non-existent, can shock-stall be considered a reliable method to prevent overspeeding.

References

[1] P. Veers, K. Dykes, E. Lantz, S. Barth, C. L. Bottasso, O. Carlson, A. Clifton, J. Green, P. Green, H. Holttinen, D. Laird, V. Lehtomäki, J. K. Lundquist, J. Manwell, M. Marquis, C. Meneveau, P. Moriarty, X. Munduate, M. Muskulus, J. Naughton, L. Pao, J. Paquette, J. Peinke, A. Robertson, J. S. Rodrigo, A. M. Sempreviva, J. C. Smith, A. Tuohy, and R. Wiser, "Grand challenges in the science of wind energy", Science **366**, eaau2027 (2019).

[2] C. Yan and C. L. Archer, "Assessing compressibility effects on the performance of large horizontal-axis wind turbines", Applied Energy **212**, 33–45 (2018).

[3] J. Cao, Z. Qin, Y. Ju, Y. Chen, W. Z. Shen, X. Shen, and S. Ke, "Study of air compressibility effects on the aerodynamic performance of the IEA-15 MW offshore wind turbine", Energy Conversion and Management **282**, 116883 (2023).

[4] D. D. Tavernier and D. V. V. Terzi, "The emergence of supersonic flow on wind turbines", in Journal of physics: conference series, Vol. 2265 (TORQUE, June 2022), p. 042068.

[5] N. N. Sørensen, F. Bertagnolio, E. Jost, and T. Lutz, "Aerodynamic effects of compressibility for wind turbines at high tip speeds", in Journal of physics: conference series, Vol. 1037, 2 (TORQUE, June 2018), p. 022003.

[6] D. H. Wood, "Some effects of compressibility on small horizontal-axis wind turbines", Renewable Energy **10**, 11–17 (1997).

[7] G. Lachmann and H. Pearcy, *Boundary layer and flow control: its principles and application*, Boundary Layer and Flow Control v. 2 (Pergamon Press, 1961).

[8] B. Lee, "Oscillatory shock motion caused by transonic shock boundary-layer interaction", AIAA journal **28**, 942–944 (1990).

[9] M. Iovnovich and D. E. Raveh, "Reynolds-averaged navier-stokes study of the shock-buffet instability mechanism", AIAA Journal **50**, 880–890 (2012).

[10] M. Thiery and E. Coustols, "Urans computations of shock-induced oscillations over 2d rigid airfoils: influence of test section geometry", Flow, Turbulence and Combustion **74**, 331–354 (2005).

[11] G. Schepers, "Pragmatic Models: BEM with Engineering Add-Ons", in *Handbook of wind energy aerodynamics*, edited by B. Stoevesandt, G. Schepers, P. Fuglsang, and Y. Sun (Springer International Publishing, Netherlands Organisation for Applied Science, Petten, the Netherlands, 2022), pp. 393–436.

[12] J. D. Anderson, *Fundamentals of aerodynamics*, 5th ed. (McGraw-Hill, New York, NY, USA, 2011).

[13] H. Glauert and G. I. Taylor, "The effect of compressibility on the lift of an aerofoil", Proceedings of the Royal Society of London. Series A, Containing Papers of a Mathematical and Physical Character **118**, 113–119 (1928).

[14] H. S. Tsien, "Two-dimensional subsonic flow of compressible fluids", Journal of the Aeronautical Sciences **6**, 399–407 (1939).

[15] T. von Karman, "Compressibility effects in aerodynamics", Journal of the Aeronautical Sciences **8**, 337–356 (1941).

[16] E. V. Laitone, "New compressibility correction for two-dimensional subsonic flow", Journal of the Aeronautical Sciences **18**, 350–350 (1951).

[17] R. Vos and S. Farokhi, *Introduction to transonic aerodynamics*, Fluid Mechanics and Its Applications (Springer Netherlands, Dordrecht, South Holland, the Netherlands, 2015), pp. 89–91.

[18] J. Stack, W. F. Lindsey, and R. E. Littell, *The compressibility burble and the effect of compressibility on pressures and forces acting on an airfoil*, tech. rep. NACA-TR-646 (1938).

[19] C. Bonilla, K. Gompertz, M. Thake, J. P. Bons, S. H. Park, and C. J. Kim, "Rotorcraft airfoil performance near critical Mach number", in 50th aiaa aerospace sciences meeting including the new horizons forum and aerospace exposition (Jan. 2012).

[20] Y. Wang, Y. Liu, Z. Zhou, and S. Wang, "Finite-wing-analogy formula for compressibility correction to pressure coefficient of an underwater vehicle model at low mach number", Physics of Fluids **35**, 016111 (2023).

[21] H. Babinsky and J. Harvey, *Shock wave-boundary-layer interactions*, Cambridge Aerospace Series (Cambridge University Press, 2011).

[22] N. F. Giannelis, G. A. Vio, and O. Levinski, "A review of recent developments in the understanding of transonic shock buffet", Progress in Aerospace Sciences **92**, 39–84 (2017).

[23] I. Mabey, *Oscillatory flows from shock-induced separations on biconvex aerofoils of varying thickness in ventilated wind tunnels*, RAE/TM/Structures-969 (Royal Aircraft Establishment, 1980).

[24] J. Gibb, "The cause and cure of periodic flows at transonic speeds (Ph.D. thesis)" (Cranfield Insitute of Technology, 1988).

[25] H. Tijdeman, "Investigations of the transonic flow around oscillating airfoils" (Delft University of Technology, 1977).

[26] L. Jacquin, P. Molton, S. Deck, B. Maury, and D. Soulevant, "Experimental study of shock oscillation over a transonic supercritical profile", AIAA Journal **47**, 1985–1994 (2009).

[27] B. H. K. Lee, "Self-sustained shock oscillations on airfoils at transonic speeds", Progress in Aerospace Sciences **37**, 147–196 (2001).

[28] B. H. K. Lee and L. H. Ohman, *Unsteady pressure and force measurements associated with transonic buffeting of a two-dimensional supercritical airfoil*, tech. rep. ADA133139 (National Research Council of Canada, 1983).

[29] S. Hanagud, X. Lu, and R. Roglin, "Smart structure technology and control of buffet induced helicopter vibrations", in 27th Conference of the European RotorCraft Forum, moscow, russia, 70 (Kamov, 2001), pp. 70.1–70.11.

[30] J. Shi, T. Xu, S. R. Schafer, and C.-L. Chen, "Adaptive control of shock waves with a passively morphing layer for rotating blades", Journal of Aerospace Engineering **28**, 04014070 (2015).

[31] A. D'Aguanno, F. F. J. Schrijer, and B. W. van Oudheusden, "Finite-wing and sweep effects on transonic buffet behavior", AIAA Journal **60**, 6715–6725 (2022).

[32] X. Jiao, W. Meng, Q. Yang, L. Fu, and Q. Chen, "Adaptive continuous neural pitch angle control for variable-speed wind turbines", Asian Journal of Control **21**, 1966–1979 (2019).

[33] J. Jonkman, S. Butterfield, W. Musial, and G. Scott, *Definition of a 5-mw reference wind turbine for offshore system development*, tech. rep. NREL/TP-500-38060 (National Renewable Energy Lab, Golden, CO, USA, 2009).

[34] J. G. Schepers, K. Boorsma, N. Sørensen, G. Sieros, H. Rahimi, H. Heisselmann, E. Jost, T. Lutz, T. Maeder, A. Gonzalez, et al., "Final results from the eu project avatar: aerodynamic modelling of 10 mw wind turbines", in Journal of physics: conference series, Vol. 1037, 2 (TORQUE, June 2018), p. 022013.

[35] E. Gaertner, J. Rinker, L. Sethuraman, F. Zahle, B. Anderson, G. Barter, N. Abbas, F. Meng, P. Bortolotti, W. Skrzypinski, G. Scott, R. Feil, H. Bredmose, K. Dykes, M. Shields, C. Allen, and A. Viselli, *Definition of the IEA Wind 15-MW offshore reference wind turbine technical report*, tech. rep. NREL/TP-5000-75698 (NREL, Golden, CO, USA, 2020).

[36] L. Prandtl, *Applications of modern hydrodynamics to aeronautics*, tech. rep. NACA-TR-116 (NACA, Jan. 1923).

[37] M. A. Hossain, Z. Huque, and R. R. Kammalapati, "Propagation of shock on nrel phase vi wind turbine airfoil under compressible flow", Journal of Renewable Energy **2013**, 1–9 (2013).

[38] A. Jameson, "Aerodynamics", in *Encyclopedia of computational mechanics* (John Wiley & Sons, Ltd, 2004) Chap. 11, pp. 334–337.

[39] B. Peerlings, "A review of aerodynamic flow models, solution methods and solvers and their applicability to aircraft conceptual design: literature study report", MSc. Thesis (TU Delft, Delft, South Holland, the Netherlands, Jan. 2018).

[40] P. R. Spalart, "Strategies for turbulence modelling and simulations", International Journal of Heat and Fluid Flow **21**, 252–263 (2000).

[41] J. Blazek, "Chapter 7 - turbulence modelling", in *Computational fluid dynamics: principles and applications*, edited by J. Blazek, Second Edition (Elsevier Science, Oxford, 2005), pp. 227–270.

[42] J. D. Crouch, A. Garbaruk, D. Magidov, and A. Travin, "Origin of transonic buffet on aerofoils", Journal of fluid mechanics **628**, 357–369 (2009).

[43] T. Cebeci and A. Smith, "Chapter 2 - conservation equations for compressible turbulent flows", in *Analysis of turbulent boundary layers*, Vol. 15, edited by F. N. Frenkiel and G. Temple, Applied Mathematics and Mechanics (Elsevier, 1974), pp. 62–90.

[44] A. Favre, "Statistical equations of turbulent gases", Problems of hydrodynamics and continuum mechanics, 231–266 (1969).

[45] H. K. Versteeg and W. Malalasekera, *An introduction to computational fluid dynamics: the finite volume method*, 2nd ed. (Pearson Education Limited, Harlow, UK, 2007) Chap. 3, pp. 40–114.

[46] P. Catalano and M. Amato, "An evaluation of rans turbulence modelling for aerodynamic applications", Aerospace Science and Technology **7**, 493–509 (2003).

[47] M. J. Smith, M. Potsdam, T.-C. Wong, J. D. Baeder, and S. Phanse, "Evaluation of computational fluid dynamics to determine two-dimensional airfoil characteristics for rotorcraft applications", Journal of the American Helicopter Society **51**, 70–79 (2006).

[48] E. Goncalves and R. Houdeville, "Turbulence model and numerical scheme assessment for buffet computations", International Journal for Numerical Methods in Fluids **46**, 1127–1152 (2004).

[49] M. Tahani, M. Masdari, H. Eivazi, and M. Tatar, "Assessment of turbulence models for transonic oscillating airfoil", International Journal of Numerical Methods for Heat & Fluid Flow **27**, 2603–2628 (2017).

[50] OpenCFD, *OpenFOAM - The Open Source CFD Toolbox - User's Guide*, 1.4, OpenCFD Ltd. (United Kingdom, Nov. 2007).

[51] P. R. Spalart and S. R. Allmaras, "A one-equation turbulence model for aerodynamic flows", in 30th aerospace sciences meeting and exhibit, Vol. 439 (AIAA, 1992).

[52] F. S. Lien, G. Kalitzin, and P. A. Durbin, "Rans modeling for compressible and transitional flows", in Proceedings of the summer program, Vol. 1 (Center for Turbulence Research, 1998), pp. 267–286.

[53] F. R. Menter, "Two-equation eddy-viscosity turbulence models for engineering applications", AIAA Journal **32**, 1598–1605 (1994).

[54] B. E. Launder and D. B. Spalding, "The numerical computation of turbulent flows", Computer Methods in Applied Mechanics and Engineering **3**, 269–289 (1974).

[55] D. C. Wilcox, "Reassessment of the scale-determining equation for advanced turbulence models", AIAA Journal **26**, 1299–1310 (1988).

[56] F. R. Menter, M. Kuntz, and R. Langtry, "Ten years of industrial experience with the SST turbulence model", Turbulence, heat and mass transfer **4**, 625–632 (2003).

[57] E. Buckingham, "On physically similar systems; illustrations of the use of dimensional equations", Physical review **4**, 345–376 (1914).

[58] W. Sutherland, "The viscosity of gases and molecular force", The London, Edinburgh, and Dublin Philosophical magazine and journal of science **36**, 507–531 (1893).

[59] C. Jiang, J. Pan, Y. Zhu, J. Li, and E. K. Quaye, "Development and verification of a high-speed compressible reactive flow solver in openfoam", Journal of Computational Science **63**, 101780 (2022).

[60] D. Modesti and S. Pirozzoli, "A low-dissipative solver for turbulent compressible flows on unstructured meshes, with openfoam implementation", Computers & Fluids **152**, 14–23 (2017).

[61] P. H. Cook, M. C. P. Firmin, and M. A. McDonald, *Aerofoil RAE 2822: pressure distributions, and boundary layer and wake measurements*, tech. rep. AR-138 (Royal Aircraft Establishment, East Lansing, MI, USA, 1977).

[62] T. Coakley, "Numerical simulation of viscous transonic airfoil flows", in 25th aiaa aerospace sciences meeting (1987), p. 416.

[63] R. I. Issa, "Solution of the implicitly discretised fluid flow equations by operator-splitting", Journal of Computational Physics **62**, 40–65 (1986).

[64] L. S. Caretto, A. D. Gosman, S. V. Patankar, and D. B. Spalding, "Two calculation procedures for steady, three-dimensional flows with recirculation", in Proceedings of the third international conference on numerical methods in fluid mechanics, edited by H. Cabannes and R. Temam (1973), pp. 60–68.

[65] H. K. Versteeg and W. Malalasekera, *An introduction to computational fluid dynamics: the finite volume method*, 2nd ed. (Pearson Education Limited, Harlow, UK, 2007) Chap. 6, pp. 186–196.

[66] M.-S. Liou and C. J. Steffen, "A new flux splitting scheme", Journal of Computational Physics **107**, 23–39 (1993).

[67] T. Karman, "Mechanische ähnlichkeit und turbulenz", in Nachrichten von der gesellschaft der wissenschaften, Vol. 322 (1930), pp. 58–76.

[68] M. Drela, "XFOIL: An Analysis and Design System for Low Reynolds Number Airfoils", in Low Reynolds Number Aerodynamics, edited by T. J. Mueller (1989), pp. 1–12.

[69] I. Gonzalez-Aparicio, A. Pian, J. P. Verhoef, G. Bergman, and P. Van der Werff, *Offshore wind energy deployment in the north sea by 2030: long-term measurement campaign. k13a, 2016-2020*, tech. rep. TNO R10371 (TNO Energy Transition, Petten, the Netherlands, 2021).

[70] I. H. Abbott and A. E. von Doenhoff, *Theory of wing sections*, 1st ed. (Dover Publications Inc., New York, NY, USA, 1959), pp. 544–545.

[71] D. M. Somers, *Design and experimental results for the S809 airfoil*, tech. rep. NRELlSR-440-6918 (National Renewable Energy Lab, Golden, CO, USA, 1997).

[72] J. W. Slater, *Rae 2822 transonic airfoil: study #1*, Dec. 2002.

[73] W. Zhou, Z. Zhang, K. Qu, and H. S. Tang, "Numerical investigation of transonic airfoil buffet suppression", in 53rd AIAA aerospace sciences meeting, Kissimmee, Florida (2015), p. 0068.

[74] Y. Fukushima and S. Kawai, "Wall-modeled large-eddy simulation of transonic airfoil buffet at high reynolds number", AIAA Journal **56**, 2372–2388 (2018).

[75] A. Memmolo, "Numerical study of transonic buffet on supercritical airfoil with different boundary layer states", PhD Thesis (Sapienza-University of Rome, Rome, Italy, 2018).

[76] P. Moise, M. Zauner, N. D. Sandham, S. Timme, and W. He, "Transonic buffet characteristics under conditions of free and forced transition", AIAA Journal **61**, 1061–1076 (2023).

[77] C. M. Langel, R. Chow, O. F. Hurley, C. (P. Van Dam, D. C. Maniaci, R. S. Ehrmann, and E. B. White, "Analysis of the impact of leading edge surface degradation on wind turbine performance", in 33rd wind energy symposium, Kissimmee, Florida (2015), p. 0489.

[78] J. Katz and A. Plotkin, "Fundamentals of inviscid, incompressible flow", in *Low-speed aerodynamics*, 2nd ed., Cambridge Aerospace Series (Cambridge University Press, 2001) Chap. 3, pp. 21–43.

[79] A. van Garrel, *Development of a wind turbine aerodynamics simulation module*, tech. rep. ECN-C–03-079 (Energy research Centre of the Netherlands, Petten, The Netherlands, Jan. 2003).

[80] H. Lamb, *Hydrodynamics*, Dover Books on Physics (Dover publications, 1932).

[81] C. Oseen, "Uber die wirbelbewegung in einer reibenden flussigkeit", Ark. Mat. Astro. Fys. **7**, 14–26 (1912).

[82] T. Sant, V. del Campo, D. Micallef, and C. S. Ferreira, "Evaluation of the lifting line vortex model approximation for estimating the local blade flow fields in horizontal-axis wind turbines", Journal of Renewable and Sustainable Energy **8**, 023302 (2016).

[83] F. Balduzzi, D. Marten, A. Bianchini, J. Drofelnik, L. Ferrari, M. S. Campobasso, G. Pechlivanoglou, C. N. Nayeri, G. Ferrara, and C. O. Paschereit, "Three-Dimensional Aerodynamic Analysis of a Darrieus Wind Turbine Blade Using Computational Fluid Dynamics and Lifting Line Theory", Journal of Engineering for Gas Turbines and Power **140**, 022602 (2017).

[84] D. Micallef, "3d flows near a hawt rotor: a dissection of blade and wake contributions", PhD Thesis (TU Delft, Delft, the Netherlands, Dec. 2012).

[85] B. Montgomerie, *Methods for root effects, tip effects and extending the angle of attack range to {+-} 180 deg., with application to aerodynamics for blades on wind turbines and propellers*, tech. rep. FOI-R-1305 (Swedish Defence Research Agency, Stockholm, Sweden, 2004).

[86] D. A. Spera, *Models of lift and drag coefficients of stalled and unstalled airfoils in wind turbines and wind tunnels*, tech. rep. NASA/CR-2008-215434 (NASA, USA, 2008).

[87] L. A. Viterna and D. C. Janetzke, *Theoretical and experimental power from large horizontal-axis wind turbines*, tech. rep. NASA-TM-82944 (NASA Lewis Research Center, Cleveland, OH, USA, 1982).

[88] Feb. 2024.

[89] M. M. Hand, D. A. Simms, L. J. Fingersh, D. W. Jager, J. R. Cotrell, S. Schreck, and S. M. Larwood, *Unsteady aerodynamics experiment phase vi: wind tunnel test configurations and available data campaigns*, tech. rep. NREL/TP-500-29955 (National Renewable Energy Laboratory, Golden, CO, USA, Dec. 2001).

[90] I. Hashem, W. Ke, and B. Zhu, "On the wake characteristics of the nrel phase vi wind turbine under turbulent inflow conditions", in 14th european conference on turbomachinery fluid dynamics & thermodynamics (European Turbomachinery Society, Apr. 2021), ETC2021–542.

[91] J. Schepers, K. Boorsma, T. Cho, S. Gomez-Iradi, A. Schaffarczyk, A. Jeromin, W. Z. Shen, T. Lutz, K. Meister, B. Stoevesandt, S. Schreck, D. Micallef, R. Pereira, T. Sant, H. Madsen, and N. Sørensen, *Final report of iea task 29, mexnext (phase 1): analysis of mexico wind tunnel measurements*, tech. rep. ECN-E–12-004 (Energy Research Center of the Netherlands, Petten, the Netherlands, May 2014).

[92] R. P. Brent, *Algorithms for Minimization without Derivatives*, 1st (Prentice-Hall, Englewood Cliffs, New Jersey, 1973).

[93] R. W. Prouty, *Helicopter performance, stability, and control* (R.E. Krieger Publishing Company, 1995), pp. 177–187.